

SPECTROSCOPY OF NEUTRON-RICH OXYGEN AND FLUORINE NUCLEI VIA SINGLE-NEUTRON KNOCKOUT REACTIONS

by

Ben Pietras

A THESIS

Submitted to the

University of Liverpool

in partial fulfilment of the
requirements for the degree of

DOCTOR OF PHILOSOPHY

Department of Physics

2009

Contents

Acknowledgements	xii
Abstract	xiv
1 Introduction	1
1.1 The Nucleus	1
1.2 The Magic Numbers and Shell Structure	3
1.3 The Nuclear Shell Model	3
1.3.1 The Woods Saxon Potential	4
1.3.2 The Spin–Orbit Interaction	5
1.4 Evolution of Shell Structure far from Stability	8
1.4.1 Nuclear Density Profiles	8
1.4.2 Halo Nuclei	9
1.4.3 Evolution of Shell Gaps	10
1.5 New Magic Numbers at $N = 14, 16$	12
1.5.1 Experimental Evidence	12
1.5.2 The Tensor Force	15

1.6	Single-Neutron Removal Reactions	18
1.6.1	Longitudinal Momentum Distributions	20
1.6.2	Adiabatic Approximation	23
1.6.3	Serber Reaction Model	24
1.6.4	Eikonal Theory	26
2	Experimental Method	33
2.1	Radioactive Ion Beam Production	33
2.1.1	Primary Beam Production	34
2.1.2	Projectile Fragmentation	35
2.1.3	Fragment Separation	35
2.2	Experimental Detection Setup	37
2.2.1	Overview of Experimental Setup	37
2.2.2	The SPEG Spectrometer	39
2.3	Direct Beam and Fragment Identification	44
2.3.1	Identification Gates	46
2.3.2	The Hybrid γ -ray Array	49
2.3.3	EXOGAM	50
2.3.4	The NaI Array	53
2.4	γ -ray Array Calibration	54
2.4.1	EXOGAM	54
2.4.2	NaI Array	57
2.5	SPEG Calibrations	58

2.6	Drift Chambers	64
2.7	Ionisation Chamber	67
2.8	Data Acquisition Trigger	71
3	Analysis	76
3.1	Target Thickness	76
3.2	Doppler Shift and Broadening Correction	77
3.2.1	Lorentz factor calculation	77
3.2.2	Theta Calculation	79
3.3	Inclusive Cross Sections	82
3.4	Exclusive Cross Sections	87
3.5	Inclusive Momentum Distributions	91
3.6	Exclusive Momentum Distributions	92
3.7	Eikonal Calculations	95
3.7.1	Exclusive Cross Sections	95
3.7.2	Experimental Spectroscopic factors	99
3.7.3	Exclusive Momentum Distributions	99
3.7.3.1	Transformation of Theoretical LMDs	101
3.7.3.2	Convolution of Theoretical LMDs	101
3.7.4	Interactions and Model Spaces	104
4	Results and Discussion	106
4.1	Inclusive One-Neutron Removal Cross Sections	107
4.2	$^{23}\text{O} \rightarrow ^{22}\text{O}$	108

4.2.1	Discussion	108
4.2.2	Inclusive One-Neutron Removal Cross Sections	109
4.2.3	Longitudinal Momentum Distributions	113
4.3	$^{24}\text{F} \rightarrow ^{23}\text{F}$	115
4.3.1	Discussion	115
4.3.2	$\gamma\gamma$ Coincidences	117
4.3.3	Exclusive One-Neutron Removal Cross Sections and Spectroscopic Factors	125
4.3.4	Longitudinal Momentum Distributions	127
4.4	$^{25}\text{F} \rightarrow ^{24}\text{F}$	133
4.4.1	Discussion	133
4.4.2	Exclusive One-Neutron Removal Cross Sections	137
4.4.3	Longitudinal Momentum Distributions	137
4.4.4	Experimental Spectroscopic Factors	142
4.5	$^{26}\text{F} \rightarrow ^{25}\text{F}$	144
4.5.1	Discussion	144
4.5.2	Longitudinal Momentum Distributions	148
	Summary	150
	References	152

List of Figures

1.1	The Chart of Nuclides	2
1.2	The Nuclear Shell Model	7
1.3	Hartree–Fock calculated neutron and proton density profiles.	8
1.4	Evolution of Shell Gaps.	11
1.5	The effect of Isospin on the Neutron Separation Energy.	13
1.6	Evolution of 2_1^+ energy in light even–even nuclei.	14
1.7	Neutron effective single particle energies.	15
1.8	Schematics illustrating the tensor interaction.	16
1.9	Neutron effective single–particle energies for ^{30}Si and ^{24}O	17
1.10	Single–nucleon removal reaction schematic.	19
1.11	Core Fragment Inclusive Longitudinal Momentum Distributions.	21
1.12	Core fragment ^{25}Ne LMD	22
1.13	Three–body system.	23
1.14	Serber model.	24
1.15	Effect of valence neutron’s angular momentum orientation on cross section.	25

1.16	^{28}Mg core fragment Theoretical Longitudinal Momentum Distributions.	26
1.17	One-dimensional Eikonal case.	28
1.18	Nucleon travelling through finite range potential of the target.	28
1.19	Core and valence neutron S-matrices for ^{26}F projectile.	30
2.1	General layout of GANIL, indicating the location of SISSI.	36
2.2	Experimental setup, from secondary beam production to SPEG.	38
2.3	SPEG High-Resolution Mass Spectrometer.	39
2.4	Optics of SPEG.	44
2.5	ΔE vs. E for all ions.	46
2.6	ΔE vs. E for the Fluorine and Oxygen isotopes.	47
2.7	X_f vs. TOF for the Fluorine and Oxygen isotopes.	47
2.8	ΔE vs. X_f for the Fluorine and Oxygen isotopes.	48
2.9	Hybrid γ -ray Array.	49
2.10	One EXOGAM Clover, comprising four segmented coaxial detectors.	50
2.11	Simulated Energy Resolution for EXOGAM.	52
2.12	Schematic of Sodium Iodide detectors.	53
2.13	EXOGAM energy Calibration.	55
2.14	Efficiency vs. Energy for the entire EXOGAM array.	56
2.15	NaI fitting technique for ^{60}Co	57
2.16	Energy vs Efficiency for the total NaI array.	58
2.17	SPEG focal plane schematic.	59
2.18	Calibration Mask.	61

2.19	$B\rho^{ref}$ scan with mask.	62
2.20	B_ρ scan across SPEG focal plane.	63
2.21	Dispersion calibration.	64
2.22	SPEG Drift Chambers.	66
2.23	Drift chamber TDC calibration.	67
2.24	Ionisation chamber TOF correction.	68
2.25	Ionisation gas pressure correction.	70
2.26	Gas pressure correction effect.	71
2.27	Circuit Diagram of Germanium link to GMT.	73
2.28	Representation of the timing signals used.	74
2.29	Circuit diagram of the Ganil Master Trigger.	75
3.1	The effect of energy loss through half the ^{12}C target.	79
3.2	EXOAM clover face.	80
3.3	Example of Doppler-correction and Add-back effects.	82
3.4	Incident beam rate, Fluorine.	83
3.5	Incident Beam Rate Scaled Down to Reaction Fragment Rate.	84
3.6	^{24}F Scaledown factors from LDCX1.	85
3.7	^{24}F Scaledown factors from Trifoil.	86
3.8	Forward EXOGAM Array Ratio.	88
3.9	Backward EXOGAM Array Ratio.	88
3.10	Isotropic Forward EXOGAM Array Efficiency.	89
3.11	Isotropic Backward EXOGAM Array Efficiency.	89

3.12	Background Subtraction schematic.	93
3.13	Example of LMD background subtraction.	94
3.14	Dependence of σ_{sp} on RMS radius.	97
3.15	Contributions of stripping (nucleon absorbed) and diffraction (nucleon dissociated) mechanisms to the single-particle cross section.	98
3.16	Eikonal distribution for the ^{24}F fragment.	100
3.17	Transformation from centre-of-mass frame to laboratory frame. . . .	102
3.18	Direct-beam-through-target longitudinal momentum distributions. .	103
3.19	Convolution of Fragment Theoretical LMDs with the Projectile DBTT LMD.	104
4.1	Level scheme of ^{22}O	110
4.2	^{22}O γ spectra.	111
4.3	^{22}O Inclusive LMD from this experiment.	114
4.4	^{22}O Inc. LMD taken from [35].	114
4.5	Comparison of ^{22}O and ^{23}F state energies.	115
4.6	^{23}F γ spectra.	116
4.7	EXOGRAM $\gamma\gamma$ coincidences for ^{23}F	117
4.8	Level Scheme of ^{23}F	119
4.9	^{23}F Shell-model predicted levels.	120
4.10	^{23}F Inclusive LMD.	128
4.11	^{23}F ground state LMD.	129
4.12	^{23}F 625(4) keV coincident LMD.	129

4.13	^{23}F 916(4) keV coincident LMD.	130
4.14	^{23}F 1702(4) keV coincident LMD.	130
4.15	^{23}F 1997(5) keV coincident LMD.	131
4.16	^{23}F 2903(4) keV coincident LMD.	131
4.17	^{23}F 3367(6) keV coincident LMD.	132
4.18	^{23}F 3793(7) keV coincident LMD.	132
4.19	Level scheme of ^{24}F compared to shell model calculations.	133
4.20	^{24}F γ spectra for the EXOGAM and NaI arrays.	134
4.21	^{24}F Shell-model predicted Levels.	135
4.22	^{24}F Inclusive LMD.	138
4.23	^{24}F ground state LMD.	139
4.24	^{24}F 523(3) keV coincident LMD.	139
4.25	^{24}F 2764(5) keV coincident LMD.	140
4.26	^{24}F EXOGAM Geant4 – data comparison.	141
4.27	Comparison of ^{25}F level scheme with shell-model predictions.	145
4.28	^{25}F γ spectra for the EXOGAM and NaI arrays.	146
4.29	Inclusive LMD of ^{25}F	149

List of Tables

2.1	Calibration Sources.	54
2.2	Data Acquisition Trigger.	72
4.1	Inclusive One-Neutron Removal Cross Sections.	107
4.2	^{23}O Inclusive One-Neutron Removal Cross Sections	109
4.3	Predicted occupancies for $^{23}\text{O} \rightarrow ^{22}\text{O}$ using the USD interaction.	112
4.4	$\gamma\gamma$ Coincidences for ^{23}F	118
4.5	^{23}F γ intensities.	121
4.6	Predicted Occupancies for $^{24}\text{F} \rightarrow ^{23}\text{F}$ using the USD interaction.	124
4.7	Exclusive Cross Sections and Spectroscopic Factors for $^{24}\text{F} \rightarrow ^{23}\text{F}$	126
4.8	Predicted Occupancies for $^{25}\text{F} \rightarrow ^{24}\text{F}$ using the USD interaction.	136
4.9	$^{25}\text{F} \rightarrow ^{24}\text{F}$ Exclusive Experimental Cross Sections.	137
4.10	$^{25}\text{F} \rightarrow ^{24}\text{F}$ Experimental Spectroscopic Factors	143
4.11	Predicted occupancies for $^{26}\text{F} \rightarrow ^{25}\text{F}$ using the USD interaction.	147

Acknowledgements



Thanks are due firstly to Beatriz Fernández-Domínguez, shown second left on the photo above. From the beginning till the end it was fantastic to work with you Bea, muchas gracias mi pequeño ardilla!

I don't know if Jeffry Thomas (far right) is the smartest guy I've ever met, but I can't think of any smarter. Jeff – thanks for your enduring patience and all the hard work you put in, both at GANIL and with the analysis. Star.

To the estimable gent, Stefanos Paschalis (centre), now living the dream in San Francisco – thankyou for all your help, especially at the beginning.

To the people in the Liverpool Nuclear group, Alex Grint, David Oxley, Fay Filmer, Laura Harkness, David Scraggs, Ren Cooper, Carl Unsworth, Ste Moon, Eddie Parr and Martin Jones – thankyou all. Special mention goes to Jones for fixing some of the

grammatical atrocities ridden throughout this doorstep (cheers la!) and for his love of prawn sandwiches and cats. Rock and roll.

Thanks also go to Marielle Chartier for giving me the opportunity to work on this data and for her help in discussing the analysis and correcting this thesis.

Nigel Orr, for his tireless work on the experiment and his enthusiastic guidance on the analysis throughout. Good on ya, ya ripper!

A mention is also due to the Surrey folk; Nicky Patterson, Simon Brown, Gemma Wilson and the irrepressible Professor Wilton Catford – all of whom made my time at GANIL so much better with than without. Thanks in particular to Nick for his work on the NaI calibration and advice on the eikonal malarky.

Ein besonderer Heil geht an Dr. Marcus “Diogenes” Scheck. Vielen Dank.

It would be very ungrateful of me not to thank the EPSRC, who have funded this work. Thankyou for making this possible, and for the places I’ve been able to visit. Thanks also to the beam operators and other collaborators at GANIL – your talents and efforts are much appreciated. As are all of those who support and contribute towards the free software that enabled the analysis. Many thanks.

Also I’d like to thank my Mum, sister Lorna and nephew Stan – his habit of running around looking cute and headbutting people was a cornerstone of this work.

Seriously – thankyou for everything.

Lastly, *no thanks at all* go to the mischievous Amanda Munns, without whom this thesis would have been done ages back.

So long, and thanks for all the fish!

ABSTRACT

At the limits of nuclear stability, increasing proton-neutron asymmetry leads to a shifting of orbitals from nuclear shell-model predictions. In turn this leads to a weakening of shell gaps such as at $N = 20$, and the emergence of new gaps at $N = 14$ and 16. To observe this evolution of the structure as the neutron dripline is approached, single-nucleon removal reactions have been employed for oxygen and fluorine isotopes. These reactions are an excellent way of probing the nuclear wavefunction to reveal information on the single-particle content in the wavefunction. Cross sections have been measured, both inclusive and exclusive, and partial production cross sections calculated. This has allowed spectroscopic factors to be extracted and compared to theoretical predictions from shell-model calculations. Longitudinal momentum distributions, both inclusive and exclusive, have also been measured. The orbital angular momentum of the removed nucleon has a pronounced effect on the momentum distribution of the surviving core, which can be compared to theoretical predictions based on eikonal theory. This gives a valuable insight into the configuration mixing for the ground and excited states of the nuclei of interest.

Chapter 1

Introduction

1.1 The Nucleus

At the centre of each atom lies a nucleus, a many body quantum system comprising of two types of particles; electrically positive protons (denoted π) and electrically neutral neutrons (denoted ν). In relation to atomic properties, and therefore material and chemical properties on a larger scale, the number of protons is the determining factor. The particles that comprise the nucleus exist in a potential created by the nucleon–nucleon forces that govern the interactions between them. There are three forces which preside; The strong, Coulomb and weak forces. The strong force is essentially responsible for the binding of the nucleons and, as its name suggests, is extremely effective over a short range (~ 2 fm). The Coulomb force is a long–range repulsive force between the positively charged protons, becoming significant in larger nuclei where the effect of the strong force weakens between the nuclear extremities. The

weak force provides a decay channel in which the type of nucleon can switch between proton and neutron if energetically favourable.

The Coulomb force determining the atomic electron configuration is well understood, however the forces behind the nuclear system are still not yet determined.

The widely adapted nomenclature to characterise the nucleus is AZ , where A is the mass number, relating to the total of protons and neutrons in the nucleus and Z is the element symbol, characterised by the number of protons the nucleus contains.

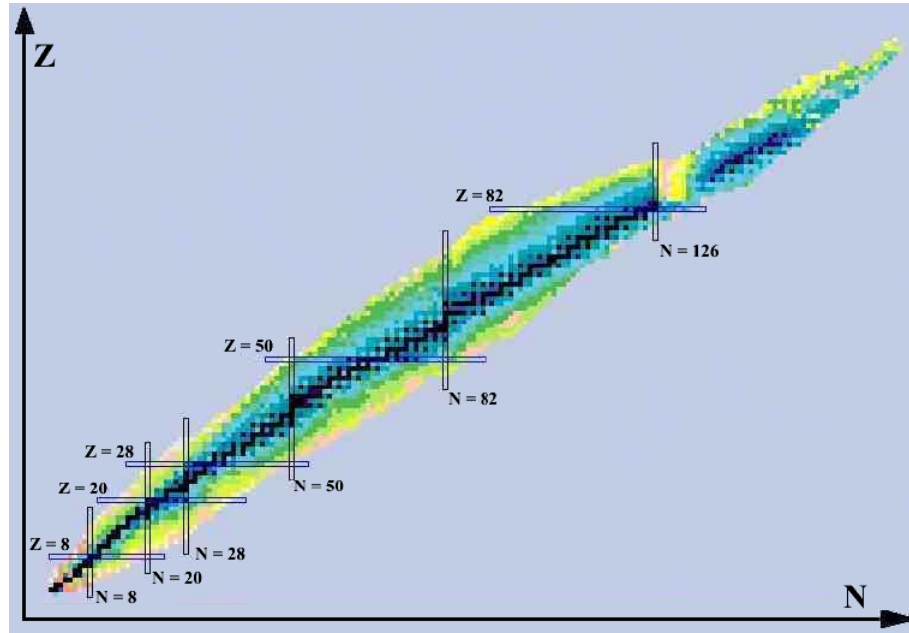


Figure 1.1: The Chart of Nuclides, including the “classical” magic numbers.

Fig. 1.1 representing the Chart of Nuclides shows the ‘valley of stability’ in black, where the nuclides are stable, i.e. not susceptible to β -decay. The number of neutrons increases along the x -axis, the number of protons along the y -axis. The boxed regions represent regions of classical magicity.

1.2 The Magic Numbers and Shell Structure

Certain combinations of neutrons and protons are more tightly bound within the nucleus, a phenomenon clearly evidenced in nuclear mass data [39]. For stable nuclei and nuclei close to the valley of stability a certain number of nucleons, namely $N = 2, 8, 20, 28, 50, 82$ and $Z = 2, 8, 20, 28, 50$ and 82 are termed ‘magic numbers’ and the nuclei exhibiting these nucleon numbers are called ‘magic nuclei’. If both the number of neutrons and the number of protons correspond to a magic number they are referred to as doubly-magic. The magic number refers to the complete occupancy of a shell, which can be considered similar to that of the electron shells found in atomic physics. The difference in energy between one shell and another is referred to as a *shell gap*. Characteristics of magic nuclei include for example a notably lower mass than the trend of their neighbour isotopes might suggest, hence a higher nucleon binding energy and an increased excitation energy to the nucleus’s first excited state for even-even nuclei. The magic numbers for β -stable and near-stable nuclei are shown in boxes beside their respective orbitals in Fig. 1.2.

1.3 The Nuclear Shell Model

Although the nucleus comprises of strongly interacting particles, due to the Pauli principle these interactions are suppressed, the system behaving as a Fermi liquid at low excitation energies. This allows stable single-particle orbits to arise.

1.3.1 The Woods Saxon Potential

The Woods Saxon potential is thought to be the most realistic approximation of the nuclear mean field potential,

$$V(r) = \frac{V_0}{1 + \exp(\frac{r-R}{a})}, \quad (1.1)$$

where V_0 represents the potential well depth, a the nuclear diffuseness and R is the nuclear radius, parameterised as $R = r_0 A^{1/3}$, where A is the mass number and r_0 represents the radius of a nucleon, $r_0 = 1.25$ fm [80].

Low lying nuclear excitations may be attributed to single-particle excitations or a collective excitation where multiple single-particle excitations are correlated.

Within the nucleus there are multiple nucleon-nucleon interactions, which combine to give a mean potential, subtracted from the two-body interaction. This mean-field potential is chosen with a view to minimise the off-diagonal matrix elements of the Hamiltonian. This can then be used to determine the single-particle orbits. The Hamiltonian consists of this mean-field potential and a residual two-body interaction between these states. By diagonalising the Hamiltonian matrix, solutions for the nuclear wavefunction may be found. Off-diagonal terms in the pure single-particle basis lead to wavefunctions which have contributions from multiple single-particle configurations. This is known as configuration mixing. In order to undertake shell-model calculations the dimension of the Hamiltonian must be reduced. This is commonly achieved by making the assumption of an inert core, where nucleons occupying the orbitals comprising this core are taken to be fully occupied, having no interactions with subsequent orbitals. In this way the core can be treated as a vacuum

around which particles and holes can be added. Typically the core is chosen to be the closest doubly-magic system to the nucleus in question. The orbitals which exist after the inert core can be taken as independent of those of lower and higher energy. This assumption is called truncation, with calculations restricted to a subset of the possible single-particle states termed a *model space*.

After making the assumption of a truncated model space, fits to known nuclear properties for a number of nuclei in this region may be made. This allows phenomenological effective interactions to be derived. Where observed single-particle energies are available they are used to adjust the mean potential [12], for cases where the energy has not been observed experimentally, the value is taken from Hartree-Fock calculations [15].

1.3.2 The Spin-Orbit Interaction

The origin of the magic numbers is explained by the addition of a *spin orbit* term to the nuclear potential. This was first proposed independently by Mayer and Jensen in 1949 [40, 29]. The modified potential is given by Eq. 1.2.

$$V_{total} = V_{central}(r) + V_{ls}(r)L \cdot S \quad (1.2)$$

Here L and S are the orbital and spin angular momentum operators for a single nucleon and $V_{ls}(r)$ is a function of the radial coordinate. The coupling of L and S means that m_l and m_s are no longer ‘good’ quantum numbers. This necessitates the use of eigenstates of the total angular momentum vector J , defined by $J = L + S$.

Squaring this relation gives

$$J^2 = L^2 + S^2 + 2L \cdot S, \quad (1.3)$$

which may be rearranged as

$$L \cdot S = \frac{1}{2} (J^2 - L^2 - S^2). \quad (1.4)$$

The expectation value of $L \cdot S$ may be referred to as $\langle ls \rangle$ and expressed via

$$\langle ls \rangle = \frac{\hbar^2}{2} [j(j+1) - l(l+1) - s(s+1)] = \begin{cases} l/2, & \text{for } j = l + \frac{1}{2} \\ -(l+1)/2, & \text{for } j = l - \frac{1}{2} \end{cases} \quad (1.5)$$

with a single nucleon spin, $s = \frac{1}{2}$. The splitting between two spin-orbit partners is thus,

$$\Delta E_{ls} = \frac{2l+1}{2} \hbar^2 \langle V_{ls} \rangle. \quad (1.6)$$

As $V_{ls}(r)$ is negative, the state with $j = l + \frac{1}{2}$ ($j_>$) has a lower energy than the state with $j = l - \frac{1}{2}$ ($j_<$). These splittings are substantial, increasingly so with higher orbital angular momentum. This results in the $j_>$ degenerate level of the initially higher level having a lower energy than the $j_<$ degenerate level of the initially lower level. This allows crossings between levels to occur. This first crossing due to this degeneracy occurs when the splitting of the first $l = 2$, $j_<$ level ($1d_{3/2}$) rises above the second $l = 0$ level ($2s_{1/2}$), as shown in Fig. 1.2.

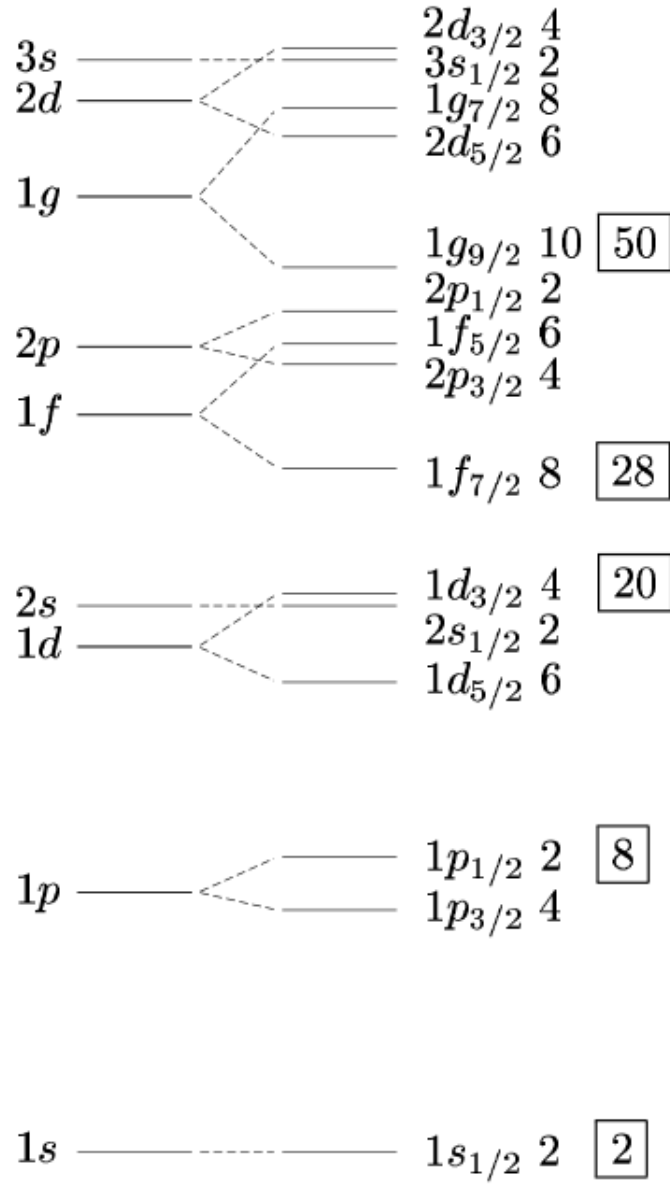


Figure 1.2: Shell sequences calculated with the Woods–Saxon potential (left) and after inclusion of the residual Spin–Orbit interaction (right). The boxes indicate the “classical” magic numbers.

1.4 Evolution of Shell Structure far from Stability

1.4.1 Nuclear Density Profiles

Shown in Fig. 1.3 are the proton and neutron matter distributions for a proton-rich nucleus ($^{31}_{18}\text{Ar}_{13}$) and neutron-rich nucleus ($^{25}_{10}\text{Ne}_{15}$) from Hartree-Fock calculations. It can be seen that the respective distributions are dependent on the nucleus' asymmetry.

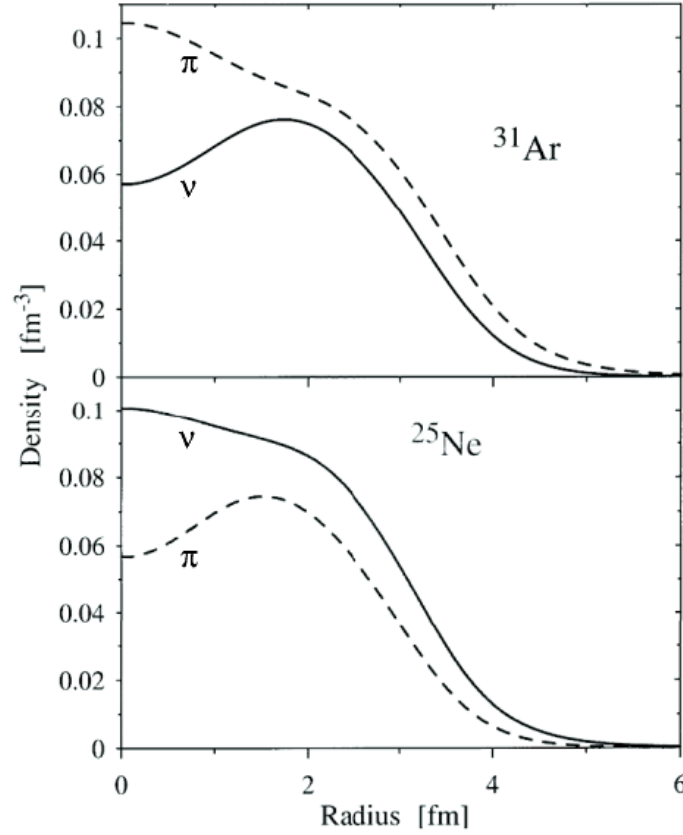


Figure 1.3: Hartree-Fock calculated neutron and proton density profiles, adapted from [22].

1.4.2 Halo Nuclei

Towards the neutron dripline the small binding contribution from nucleon–nucleon pairing becomes significant. Nuclei with an even number of neutrons may be bound, while isotopes with an odd number are not, even if they have a lower mass. Examples of this include ^{10}Li , ^{21}C (unbound) and ^{11}Li , ^{22}C (bound).

In certain neutron–rich nuclei the weakly bound neutrons may exhibit a far greater spatial distribution than predicted by the liquid drop model. The nucleus may be thought of as a core nucleus whose valence nucleons wavefunctions extend far out into the classically forbidden region, creating a “halo”. This halo state can be described as a threshold phenomenon resulting from the presence of a bound state close to the continuum. As the strong force acts over very short distances and the separation energy is very low, the valence nucleons are allowed to tunnel out to a much greater spatial extent than normally permitted and be present at distances far from the nuclear core.

The structure of the borromean nucleus ^{11}Li was the first observation of a halo and is an excellent example of this phenomenon. ^{11}Li had an interaction radius as large as ^{208}Pb , yet is 20 times lighter. This nucleus can be thought of as ^9Li with two neutrons as a halo, first observed at RIKEN in 1985 [65]. Halo nuclei may have one (^{11}Be [4]), two (^{11}Li , ^{22}C [65, 31]), or even 4 (^8He [66]) nucleon halos. Proton halos have also been observed (^8B [57]), but cannot extend to the size of neutron halos due to the Coulomb barrier. Many more halos have been theoretically predicted [32].

1.4.3 Evolution of Shell Gaps

For stable or near-stable nuclei the nuclear potential and resulting shell structure is well known. Far from the valley of β -stability this potential changes, resulting in the development of new magic numbers and the breakdown of shell gaps established for stable nuclei [44]. The high asymmetry of proton and neutron number in these systems means the spin-isospin component of the nucleon-nucleon interaction becomes significant. In the region of $N \geq 20$ and $Z \leq 12$, referred to as the “island of inversion” [76], intruder particle-hole excitations across the $N = 20$ shell gap dominate the ground state wavefunction. This results in the nuclei of this region having strongly deformed structures [70, 47, 76].

This new phenomenon necessitated a revision of established nuclear structure models to account for the onset of deformation along the classically magic $N = 20$ isotones. This deformation was reproduced in a deformed Hartree-Fock calculation [16], later confirmed by shell-model calculations where the inclusion of the $1f_{7/2}$ shell in the model space permitted cross shell excitation [78]. A calculation which, in addition to the $1f_{7/2}$, allowed occupation of the $2p_{3/2}$ subshell found the “correlation energy” gained in residual particle-hole and pairing interactions to be greater than the energy difference between the $1d_{3/2}$ and $1f_{7/2}$ subshells for the nuclei in this region. This demonstrates that the spacing of single-particle states is not the sole consideration when explaining the breakdown of shell gaps.

For nuclei close to the neutron dripline there are long standing predictions that the nuclear surface will be far more diffuse [21, 22]. This is thought to be due to the

weak binding of the valence nucleons and the proximity of the Fermi surface to the particle continuum. In such high isospin nuclei the resulting shallow single-particle potentials combined with pairing correlations could yield a more uniformly spaced shell structure (see Fig. 1.4). The spin-orbit interaction is also dependent on the variation of potential with nuclear radius, lessening the gap between two spin-orbit pairs for nuclei with a more diffuse nuclear surface. This may lead to the loss of traditional shell gaps present in β -stable nuclei [48].

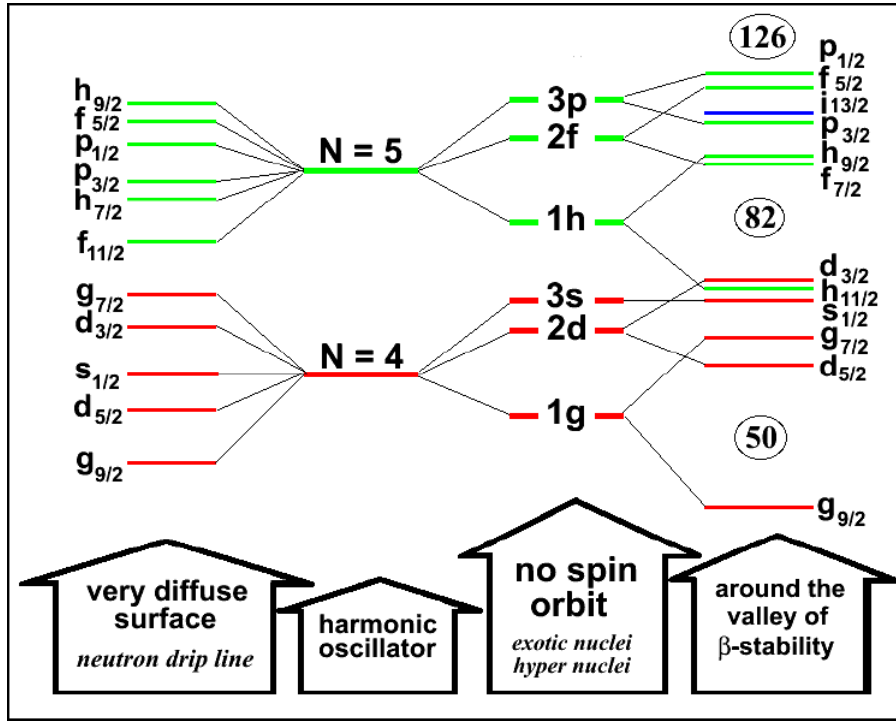


Figure 1.4: Evolution of shell gaps, adapted from [22].

1.5 New Magic Numbers at $N = 14, 16$

1.5.1 Experimental Evidence

As the neutron dripline is approached, the structure of nuclei between $Z \simeq 8$ and $Z \simeq 12$ changes drastically from that at stability. For ^{16}O double-magicity results in a very strongly bound nucleus with a shell gap of ~ 10 MeV [77]. Considering that ^{28}O would be predicted to be doubly-magic it could be expected to be stable or comparably long-lived, however the $N = 20$ shell closure is insufficient, resulting in ^{28}O being unbound [67]. Conversely, ^{24}O has recently been identified as a doubly magic nucleus [64, 34], revealing the shifting of the magic numbers at the limits of stability. This has resulted in the interaction of the sd shell being revised [44]. A drop in the neutron separation energy, S_n , signifies the presence of a shell gap, with it being relatively easier to remove the neutron added after the gap. Fig. 1.5 shows the evolution of S_n for nuclei with different values of isospin. In the top figure a sharp drop in S_n at $N = 16$ can be seen for $T_Z = 5/2$, becoming more pronounced for $T_Z = 7/2$. Accompanying this is the smoothing of the drop at $N = 20$. This is direct evidence of the decline of traditional magic numbers and the emergence of new ones as the neutron dripline is approached.

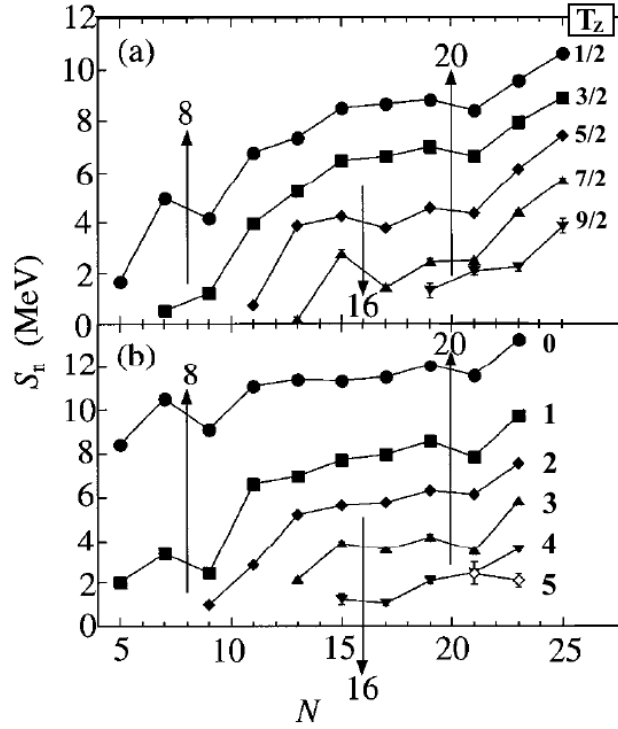


Figure 1.5: The effect of Isospin on the Neutron Separation Energy. The top figure shows nuclei with odd N , even Z , each line representing a different isospin value. The bottom figure shows this for nuclei with odd N , odd Z . Modified from [46].

Another strong indication of the existence of a magic number is the change in the 2_1^+ energy for even-even nuclei along an isotopic chain. Shown in Fig. 1.6 are the 2_1^+ state energies for a number of light even-even nuclei. The sharp rise between ^{20}O and ^{22}O , also ^{22}O and ^{24}O indicates the emergence of new magic numbers at $N = 14$ and $N = 16$ for the Oxygen isotopes [8].

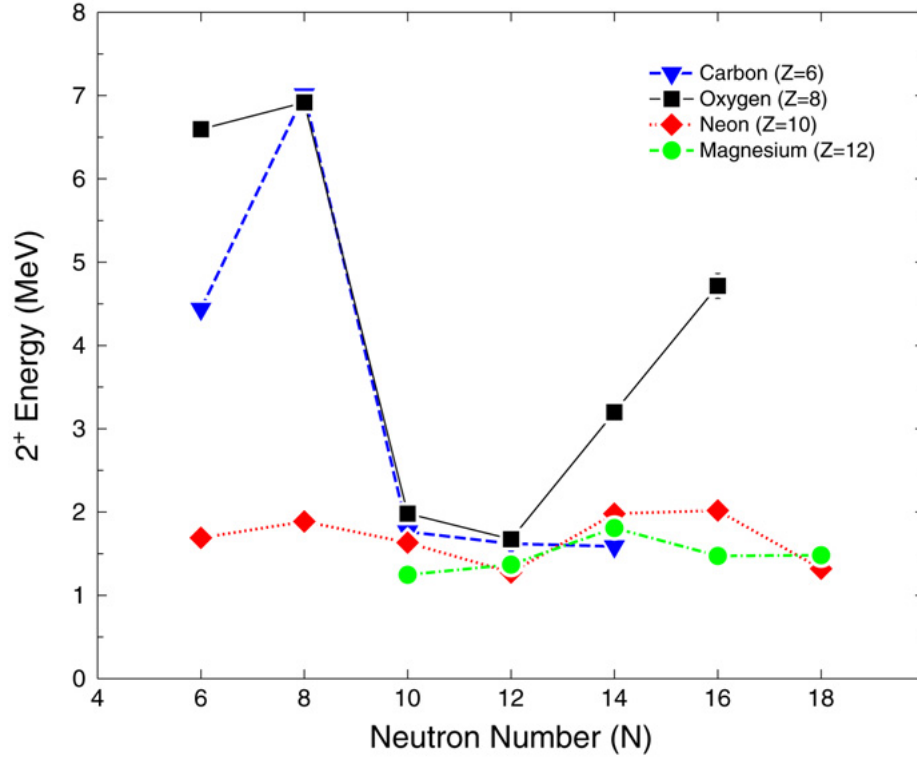


Figure 1.6: Evolution of 2_1^+ energy in light even-even nuclei. Taken from [30].

The evolution of the effective single particle energies for Oxygen and Carbon can be seen in Fig. 1.7. The values were calculated using the monopole matrix elements of the USDB interaction [14]. The emergence of new magic numbers is clearly evident as the neutron number increases. The $\nu d_{3/2}$ level can be observed to be bound by ~ 1 MeV at $N = 16$, which corresponds to ^{24}O .

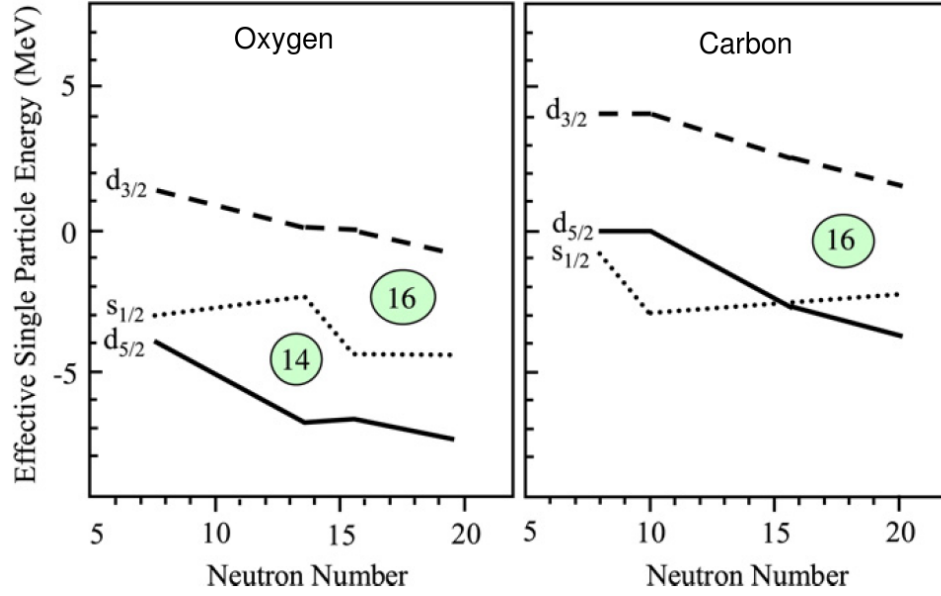


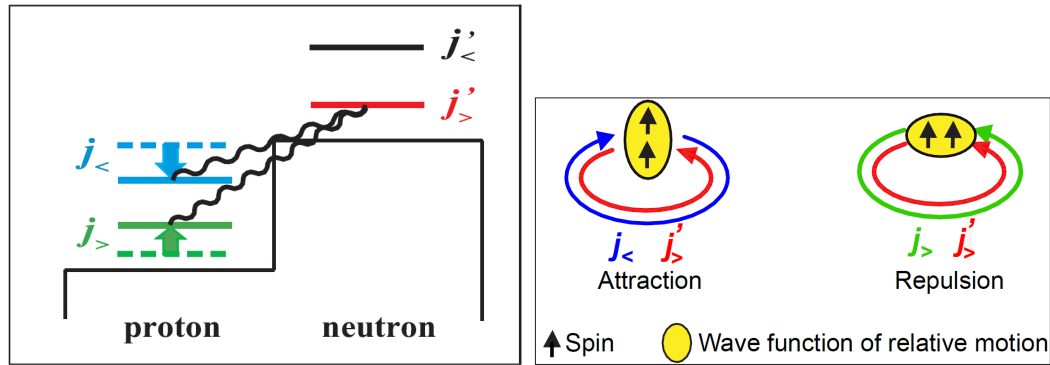
Figure 1.7: Neutron effective single particle energies as a function of neutron number in the isotopic chains. Taken from [62].

The importance of the monopole part of the proton–neutron residual interaction becomes apparent when considering the last bound cases of the Oxygen and Fluorine isotopes. Oxygen terminates at ^{24}O [27, 25], whereas the addition of a single proton enables six extra neutrons to bind to create ^{31}F [54]. This large extension of the neutron dripline from Oxygen to Fluorine can be explained by the addition of a single proton in the $\pi d_{5/2}$ orbit, which causes its spin-flip partner $\nu d_{3/2}$ orbit to become more bound by about the value of the monopole involved, in this case $V_{d_{5/2}d_{3/2}}^{pn} \sim 2 \text{ MeV}$.

1.5.2 The Tensor Force

The disappearance of the standard magic numbers and the emergence of new numbers such as 6, 16 and 34 for light, neutron–rich nuclei led T. Otsuka and co–workers to

propose that an explanation could be a nucleon–nucleon interaction. He postulated that in exotic nuclei the spin–isospin component of the interaction has a powerful effect [44]. The occupancy of the proton orbital $j_>$ ($j_> = l + \frac{1}{2}$) significantly alters the energy of the $j_<$ ($j_< = l - \frac{1}{2}$) neutron orbital. When there are more protons occupying the $j_>$ orbital there is a greater summed attraction between these protons and the $j_<$ neutrons, which reduces the energy of the $j_<$ neutron level. This property is referred to as the tensor interaction [45]. This property is illustrated in Fig. 1.8.



(a) The shifting of proton spin–orbit partners (b) The attractive and repulsive components due to the tensor interaction. of the tensor interaction.

Figure 1.8: Schematics illustrating the tensor interaction [45].

Fig. 1.8(a) illustrates the attractive and repulsive interactions of the tensor force. In Fig. 1.8(b) the left of the figure shows the case where the relative motion wavefunction (yellow) is aligned in the same direction as the spin (black arrows), creating an attractive force between the spin–orbit partners of different type nucleons. The right of Fig. 1.8(b) shows the case where the relative motion wavefunction is aligned on

an axis orthogonal to the spin direction, resulting in a repulsive force between two different type nucleons of the same spin-orbit level.

A good example of shell migration due to the tensor interaction is shown in Fig. 1.9 [44]. The tensor interaction occurs between the protons in the first $d_{5/2}$ orbital and the neutrons in the first $d_{3/2}$ orbital. For ^{30}Si the first $d_{5/2}$ proton orbital is fully occupied, whereas in ^{24}O this $d_{5/2}$ level is vacant, resulting in a lack of attraction for the neutron $d_{3/2}$ orbital, which subsequently becomes less strongly bound (shown by dotted line). The resultant change in the effective single particle energy (ESPE) reduces the shell gap between the $1d_{3/2}$ and $1f_{7/2}$ neutron subshells. This results in the disappearance of the traditional $N = 20$ magic number in ^{24}O and the emergence of a new magic number at $N = 16$.

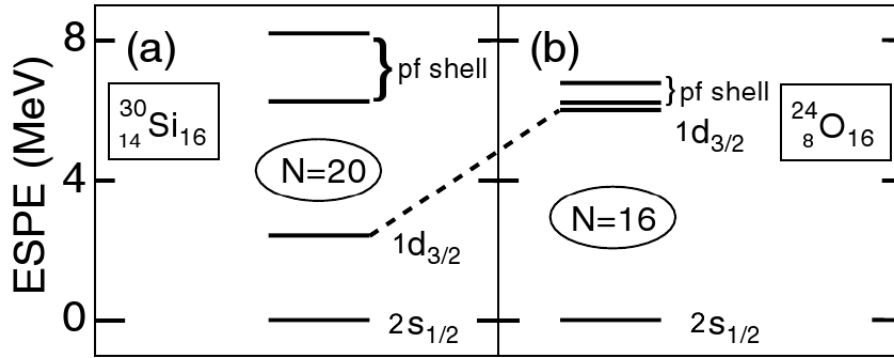


Figure 1.9: Neutron effective single-particle energies for a) ^{30}Si and b) ^{24}O . Adapted from [44].

1.6 Single-Neutron Removal Reactions

In order to explore the evolution of shell structure at the extremes of nuclear stability the reaction channel of single-neutron removal at intermediate energies is an excellent tool. Due to the unstable nature of the nuclei to be studied it is necessary to employ inverse kinematics, where the radioactive beam of exotic nuclei is incident on a light, stationary nuclear target. The removal reaction itself is sensitive to the occupation of single particle orbitals [28, 11, 53].

This mechanism enables detailed probing of the nuclear ground state and excited states, and was particularly successful [68] in investigating the “island of inversion”, the area of the nuclear chart where $N \geq 20$ and $10 \leq Z \leq 12$, characterised by the presence of intruder states, as previously discussed.

A schematic representation of a single-nucleon removal (sometimes referred to as “knockout”) reaction is shown in Fig. 1.10. For these reactions a nucleus with mass A impinges on a light nuclear target, causing the separation of a nucleon from the $A-1$ fragment core of the projectile’s incident nucleus. This fragment core is then observed moving at approximately the projectile velocity in the exit channel. The incident nucleus typically has an energy of the order of 50 A.MeV in order to reduce the probability of multiple interactions. The system can then be treated with an adiabatic approximation, as explained in Section 1.6.2.

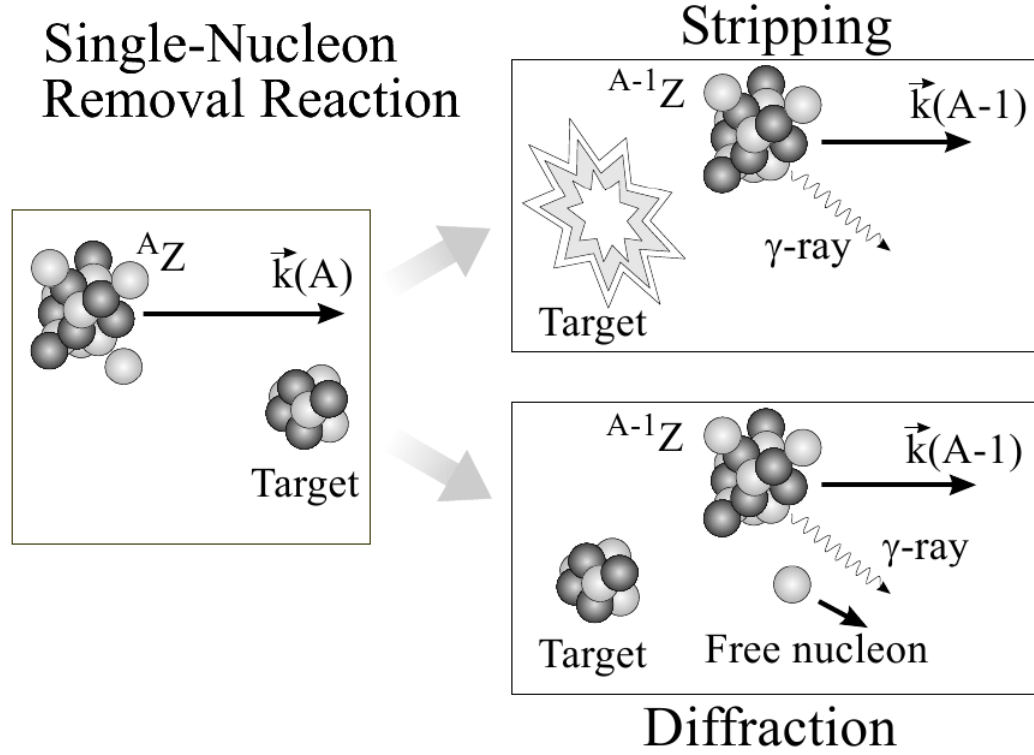


Figure 1.10: Single-nucleon removal reaction schematic.

The nucleon may be separated via two main processes; stripping and diffraction. Stripping occurs when one nucleon is absorbed by the target, leaving the $A-1$ fragment nucleus intact. The Serber model [58] describes this as the “transparent limit”, where the target is transparent to the core. Diffraction refers to the case where both the nucleon and residual core undergo an elastic interaction with the target, leaving the core-nucleon system in an unbound state. In both these cases the $A-1$ core fragment is present in the exit channel, and it is the residue fragment’s longitudinal momentum distribution (LMD) which carries the signature of the angular momentum of the nucleon removed. This in turn gives information of the orbital occupancy for the fragment state, the spectroscopic factor related to the overlap of the projectile’s

ground state wavefunction and the wavefunction of the state in which the fragment was produced. By gating on the transition γ rays, information can be derived for the excited states. The partial cross sections can be used to give spectroscopic information on these excited states, giving spectroscopic factors which are comparable to theory.

1.6.1 Longitudinal Momentum Distributions

Another excellent example of the strength of observing the core nuclei’s longitudinal momentum distributions as a spectroscopic tool to observe nuclear structure was the work by E. Sauvan, et al [55] at GANIL. For this experiment ^{40}Ar was fragmented at ~ 70 A.MeV to produce a “cocktail” of nuclides. The inclusive LMDs of a number of different nuclei following one-neutron removal reactions is shown in Fig. 1.11. If the addition of a single neutron results in a dramatic reduction in the width of the LMD of the core fragment it is indicative of a shift from d-wave to s-wave occupancy.

This effect can be seen in the oxygen and fluorine nuclei. For isotopes up to $N = 14$ the wide LMDs indicate occupation of the $1d_{5/2}$. After 14 neutrons have been added, the $1d_{5/2}$ orbital is full, any additional neutrons occupy the $2s_{1/2}$ orbital. This is reflected in the sharply reduced LMD width of ^{24}F and ^{23}O when $N = 15$. This can reveal surprising results, such as the case of ^{14}B . After filling the $\nu 1p_{1/2}$ shell in ^{13}B , it is expected that the following neutron to be added to the system would occupy the $1d_{5/2}$ shell (see Fig. 1.11). Examining the change in LMD width from $^{13}\text{B} \rightarrow ^{14}\text{B}$ there is a distinct narrowing, indicating that the valence neutron alternatively occupies the $2s_{1/2}$ orbital. This is also the case for $^{14}\text{C} \rightarrow ^{15}\text{C}$, indicating that $2s_{1/2}$ is an intruder orbital for these elements above the $N = 8$ isotone. In addition to the LMD the one neutron

removal cross section (σ_{-1n}) can give information on the nuclear structure. The LMD of ^{14}B indicated that the valence neutron predominantly occupied the $2s_{1/2}$ orbital, while the relatively large σ_{-1n} indicted an extended neutron density distribution. Both of these are signatures of a halo nucleus, supporting previous findings [7].

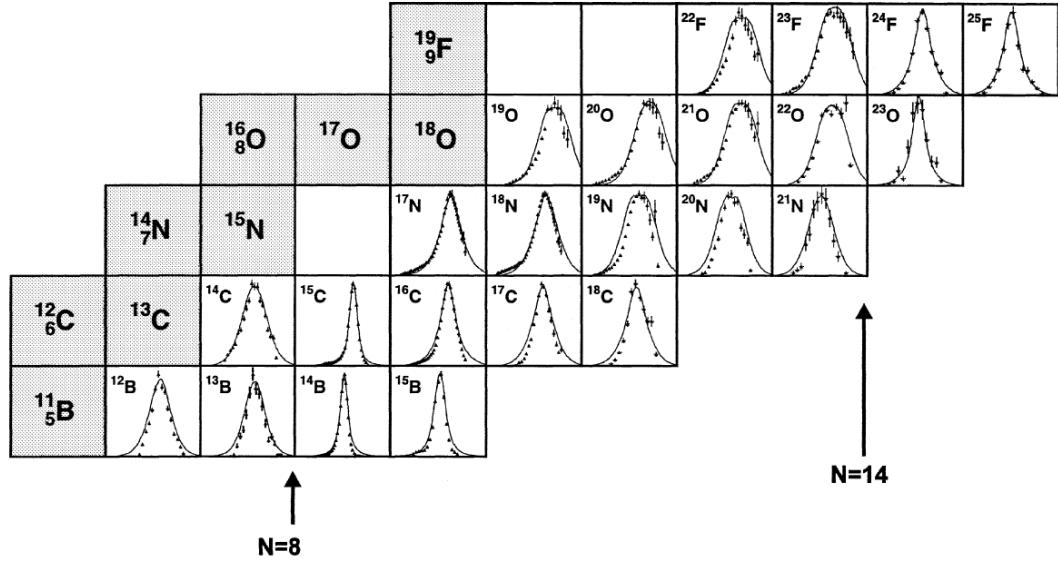


Figure 1.11: Core fragment inclusive longitudinal momentum distributions for one neutron removal on a ^{12}C target. Solid lines represent the theoretical distribution calculated using the Glauber (eikonal) model [55].

A good example of how inclusive and exclusive longitudinal momentum distributions can give information on the single particle structure is given by work done at MSU on single-neutron removal reactions, shown in Fig. 1.12 are exclusive LMDs for $^{26}\text{Ne} \rightarrow ^{25}\text{Ne}$, the ground state of ^{25}Ne extracted via the removal of the excited states' contribution to the inclusive LMD [68].

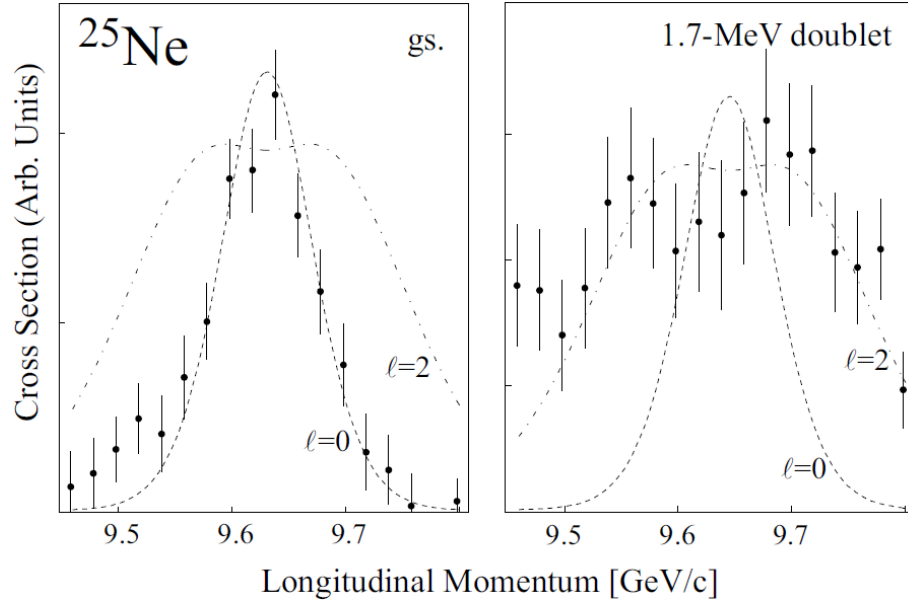


Figure 1.12: Core fragment ^{25}Ne LMD following single-neutron removal. Overlaid are theoretical eikonal predictions for s-wave and d-wave occupancy. Taken from [68].

It can clearly be seen to the left of Fig. 1.12 that the ground state LMD has a strong s-wave contribution, this tells us that the ground state of ^{25}Ne has a high occupancy of the $2s_{1/2}$ orbital, while the states that comprise the 1.7 MeV doublet show a strong d-wave occupancy from the exclusive momentum distribution. This technique is extremely sensitive, with valuable spectroscopic information available using beam rates as low as a few particles per second. In addition to the LMDs, the inclusive and exclusive cross sections can be calculated, from which experimental spectroscopic factors may be extracted, shedding further light on the nuclear structure.

1.6.2 Adiabatic Approximation

In order to observe the above effects it must be possible to reduce other interactions in the system. This is achieved by using a beam energy of the order of 50 A.MeV. An essential step is to take two sets of dynamical variables and assign one set as high-energy (*fast*) and the other as low-energy (*slow*). In Fig. 1.13 the fast variable is \mathbf{R} , the projectile's centre of mass translational motion, while the slow variable is \mathbf{r} , the projectile's internal motion [72]. This means that at high beam energies the core and valence system barely change in the time it takes the nucleus to traverse the target, essentially reducing the system from a three-body to a two-body case.

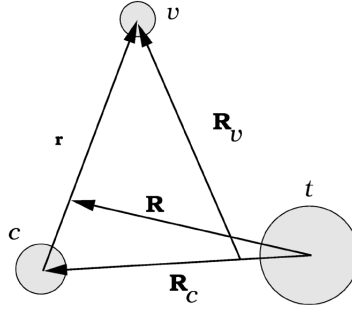


Figure 1.13: Definition of the coordinate system adopted for the core, valence nucleon and target three-body systems, taken from [73].

A further advantage to the small time frame in which the projectile traverses the target is that it is possible to discount the possibility of further interactions between core and target following single-nucleon removal. Thus we can assume the state in which the core is detected is directly associated with the single-nucleon removal reaction.

1.6.3 Serber Reaction Model

An early model by Serber assumed that the target nuclei acted like a black disc [58]. Shown in Fig. 1.14 is the case for an incident deuteron. Depending on the impact parameter and orientation of the deuteron, one of its nucleons will be absorbed by the target (in the case of Fig. 1.14, the proton), while the core continues unaffected along the initial trajectory. This approximation has proven useful in a number of cases

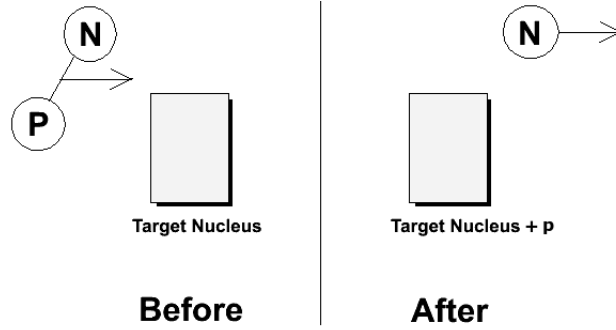


Figure 1.14: Proton stripping for an incident deuteron, Serber model [58].

regarding heavier nuclei, for example modelling ^{11}Be as a neutron and a ^{10}Be core, forming a one neutron halo nucleus. Assuming the target is transparent to the core, but the neutron is absorbed, the theoretical LMD fits the experimental data well [42]. However, for the case of proton knockout of ^8B on a ^{12}C target [61] the LMD is far narrower than the Serber model predicts. This discrepancy can be understood by considering that the ^8B valence nucleon predominantly occupies the $1p_{3/2}$ shell with $l = 1$, giving evidence of a proton halo [17]. The valence nucleon of ^{11}Be abnormally occupies the $2s_{1/2}$ orbital as a halo with the spectroscopic factor, $C^2S = 0.74$ [4],

giving a dominant $l = 0$ effect. Neutron halo nuclei are able to have a surprisingly large spatial extension when predominantly s-wave, due to the lack of both an angular momentum and Coulomb barrier.

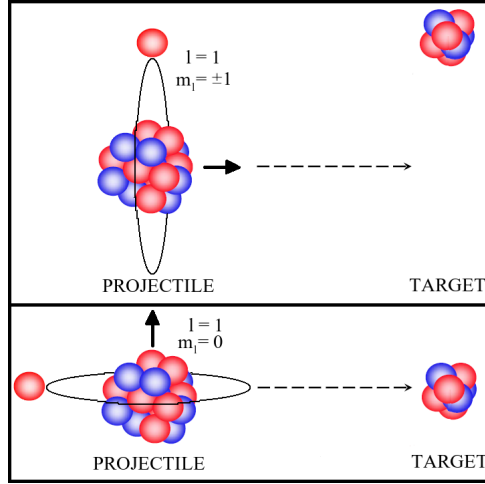


Figure 1.15: The orientation of the valence nucleon relative to the projectile momentum has an effect on the removal cross section, if the valence nucleon's angular momentum projected along the beam axis with $m_l = \pm 1$ the reaction is more likely, with $m_l = 0$ absorption is favoured.

The schematic Fig. 1.15 demonstrates that for nuclei where the valence nucleon occupancy is not predominantly s-wave, absorption of the core becomes a more dominant factor. The direction of the valence nucleons angular momentum relative to the beam axis also has a pronounced effect on the longitudinal momentum distribution. Fig. 1.16 demonstrates this effect. A reduced reaction probability for $m_l = 0$, is reflected in the reduced contribution to the overall LMD.

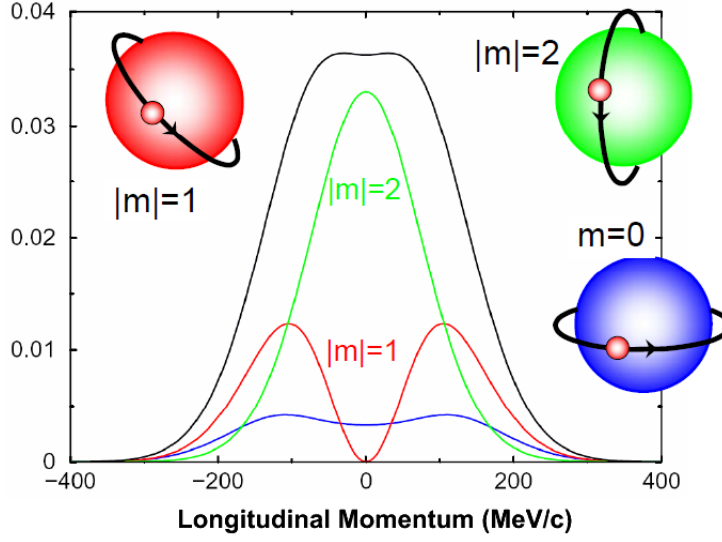


Figure 1.16: ^{28}Mg core fragment theoretical longitudinal momentum distributions [73].

1.6.4 Eikonal Theory

In order to deduce the cross sections for the removal of a neutron from each nuclide, the probability of nucleon removal at each impact parameter value needs to be calculated, along with the scattering of the nuclear core. Eikonal theory may be employed to this aim [71]. The Adiabatic assumption is taken, along with the assumption that the residual nucleus continues unperturbed along the projectile's incident trajectory as a point-like particle. The potential $U(r)$ is defined as

$$U(r) = V_C(r) + V(r) + V_{so}(r)\vec{l} \cdot \vec{s}, \quad (1.7)$$

with V_C the Coulomb potential, $V(r)$ the nuclear potential due to the strong force and $V_{so}(r)\vec{l} \cdot \vec{s}$ being the contribution from the spin-orbit interaction. For a semi-classical solution of the projectile's motion the Schrödinger equation needs to be solved in the

centre of mass frame,

$$\left(-\frac{\hbar^2}{2\mu} \nabla_r^2 + U(r) - E_{cm}\right) \chi_k^+(\vec{r}) = 0, \quad (1.8)$$

where the reduced mass is given by

$$\mu = \frac{m_c m_v}{m_c + m_v}, \quad (1.9)$$

with m_c (m_v) being the core (valence nucleon) mass and $\chi_k^+(\vec{r})$ the distorted wavefunction. When $|U|/E \ll 1$, i.e. in cases where the beam energy is sufficiently high that the variation in potential is negligible over the incident nucleus' wavelength, we can use the expression

$$k = \sqrt{\frac{2\mu E}{\hbar^2}}, \quad (1.10)$$

to substitute into Eq. 1.8, giving

$$\left(\nabla_r^2 - \frac{2\mu}{\hbar^2} U(r) + k^2\right) \chi_k^+(\vec{r}) = 0. \quad (1.11)$$

The distorted wavefunction may be written as

$$\chi_k^+(\vec{r}) = \exp(i\vec{k} \cdot \vec{r}) \omega(\vec{r}), \quad (1.12)$$

with the $\omega(\vec{r})$ component present to account for elastic scattering as the initial state of the system is modified by eikonal phases. Substitution yields

$$\left[2i\vec{k} \cdot \nabla \omega(\vec{r}) - \frac{2\mu}{\hbar^2} U(r) \omega(\vec{r}) + \nabla_r^2 \omega(\vec{r})\right] \exp(i\vec{k} \cdot \vec{r}) = 0. \quad (1.13)$$

As $2\vec{k} \cdot \nabla \omega(\vec{r}) \gg \nabla_r^2 \omega(\vec{r})$, the $\nabla_r^2 \omega(\vec{r})$ curvature term in Eq. 1.13 can be discounted, assuming a straight line path. In order to simplify the problem further the path of \vec{k}

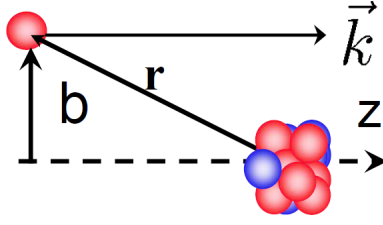


Figure 1.17: One-dimensional Eikonal case [73].

can be taken to be the z -axis. This now leaves a one-dimensional problem, shown by Fig. 1.17. This simplifies the case to

$$\frac{d\omega}{dz} \simeq -\frac{i\mu}{\hbar^2 k} U(\vec{r}) \omega(\vec{r}) \quad (1.14)$$

This may be used to give a solution of ω as

$$\omega(\vec{r}) = \exp \left[-\frac{i\mu}{\hbar^2 k} \int_{-\infty}^Z U(r') dz' \right]. \quad (1.15)$$

The relationship outlined in Eq. 1.15 shows that the phase ω changes as the nucleon passes through the region of nuclear potential. The $V_C(r)$ term in Eq. 1.7 is neglected as the eikonal model assumes no deflection, that the nucleon follows a straight path through a finite-range potential at an impact parameter b , shown in Fig. 1.18.

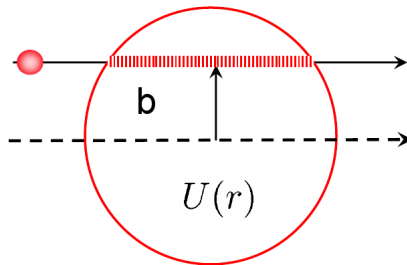


Figure 1.18: Nucleon travelling through finite range potential of the target [73].

After the interaction (as $z \rightarrow \infty$), Eq. 1.12 may be written as

$$\chi_k^+(\vec{r}) \rightarrow \exp(i\vec{k} \cdot \vec{r}) \exp \left[-\frac{i\mu}{\hbar^2 k} \int_{-\infty}^{\infty} U(r') dz' \right] = S(b) \exp(i\vec{k} \cdot \vec{r}), \quad (1.16)$$

where $S(b)$ is the amplitude of the outgoing waves in the forward direction as a result of scattering at impact parameter b , the eikonal approximation to the S-matrix.

The velocity of the projectile may be given by

$$v = \frac{\hbar k}{\mu}, \quad (1.17)$$

substitution yields

$$S(b) = \exp \left[-\frac{i}{\hbar v} \int_{-\infty}^{\infty} U(r') dz' \right]. \quad (1.18)$$

S-matrices (also referred to as *profile functions*) can be employed to calculate single-nucleon removal partial cross sections by giving an impact parameter dependent probability that the incident nucleon can travel through or be absorbed. The parameters used in the calculation of S-matrices are an effective nucleon-nucleon interaction, the assumed matter distributions and the root mean squared (RMS) radii of the core and target nuclei. The total interaction between the projectile and target is taken as the sum of the interactions between the constituents of the projectile and the target. In order to calculate the reaction cross sections, the transmission (absorption) of both the core and the valence neutron need to be calculated. In Fig. 1.19 the S-matrices are shown both for a core ^{25}F and one valence neutron which comprise an incident ^{26}F projectile [74]. The real (imaginary) part of the profile function is related to the scattering (absorption) of the neutron. The small region of negative values is caused by the inclusion of the imaginary part.

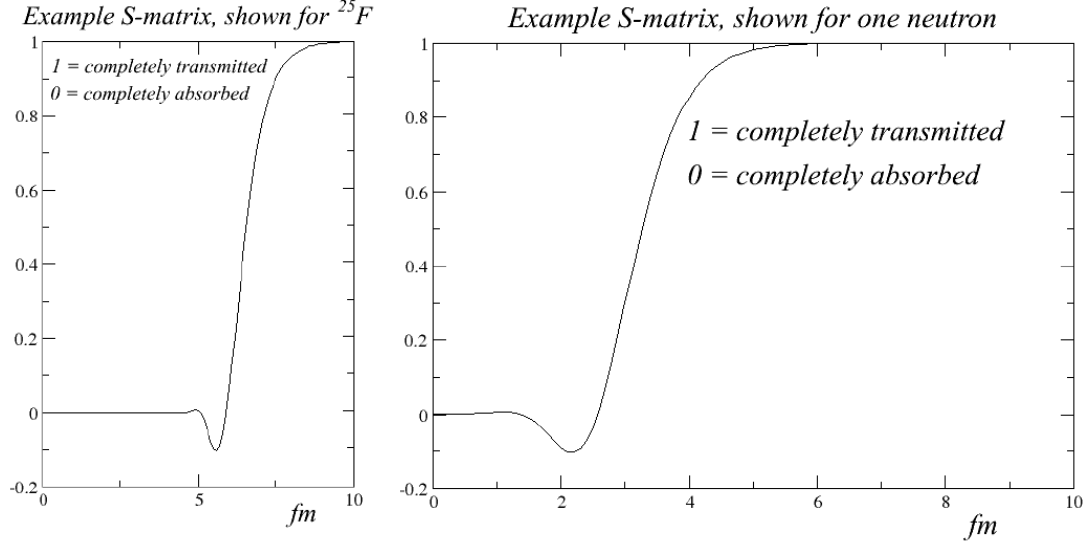


Figure 1.19: Core and valence neutron S-matrices for ^{26}F projectile [74].

In single-nucleon removal reactions the two main processes involved are stripping (where the nucleon is absorbed by the target) and diffractive breakup (where the nucleon is dissociated from the core through their two-body interactions with the target). After the S-matrices for a specific case have been calculated, the stripping cross section may be found via

$$\sigma_{str} = \frac{1}{2j+1} \int d\vec{b} \sum_m \langle \psi_{jm} | (1 - |S_n|^2) |S_c|^2 | \psi_{jm} \rangle. \quad (1.19)$$

Eq. 1.19 firstly integrates over all impact parameters, combining this with the probability that the core survives ($|S_c|^2$) and the valence nucleon is absorbed ($1 - |S_n|^2$). The core fragment relative-motion wavefunctions (ψ_{jm}) are calculated as eigenstates of an effective two-body Hamiltonian whose local potential has been adjusted to reproduce the separation energy of the nucleon from the initial state to the state of interest [28]. This separation energy is the sum of the ground-state (GS) nucleon separation energy

and the excitation energy of the core fragment final state. Similarly, the cross section for diffractive breakup may be found via

$$\sigma_{dif} = \frac{1}{2j+1} \int d\vec{b} \left[\sum_{m,m'} [\langle \psi_{jm} | (1 - S_n S_c)^2 | \psi_{jm} \rangle \delta_{mm'} - |\langle \psi_{jm'} | (1 - |S_n S_c|) | \psi_{jm} \rangle|^2] \right]. \quad (1.20)$$

The partial cross section for single-particle removal is just the sum of these two processes, namely $\sigma_{sp} = \sigma_{str} + \sigma_{dif}$. There is another minor contribution, σ_C , which corresponds to Coulomb dissociation. As the target was light this contribution was assumed negligible [28], which enables the one-dimensional integral to be taken over a straight line path through the nuclear potential at the impact parameter, shown in Eq. 1.15. The partial cross section derived from the S-matrices assumes that a nucleon is there to be removed. The actual cross section depends on the occupancy of each considered subshell, which can be given in the form of spectroscopic factors (C^2S values). Theoretical C^2S values can be given by shell-model calculations, using codes such as OXBASH [15] based on NuShell [49]. Experimental C^2S values may be extracted by dividing the exclusive cross sections measured from data with the theoretical single-particle cross section for that state. As these are different for the s-wave and d-wave orbitals the relative occupancy needs to be known. Ergo, experimental spectroscopic factors can be extracted for cases where the relative occupancy is well known or for the case where it can be assumed that a single subshell is occupied, either from the information provided by the longitudinal momentum distribution corresponding to that state or restrictions of angular momentum coupling. In order to compare experimental C^2S values with theory, a centre-of-mass correction

needs firstly to be employed to the theoretical spectroscopic factors (see Section 3.7). The experimental spectroscopic factors give information on the occupancy of the single particle states for each state, thus testing shell-model predictions and shedding light upon the nuclear structure.

Chapter 2

Experimental Method

The main purpose of this experiment is to determine the reaction cross-sections for several neutron-rich nuclides from the single-neutron removal channel, and further the partial cross-sections relating to individual states (excited and ground) by use of γ -ray tagging. By comparing the longitudinal momentum distributions for both the inclusive and exclusive cases to theoretical predictions, information on the single-particle states can be obtained, along with spectroscopic factors extracted from the cross-sections. The set-up and calibration of the experiment will be discussed, including the reconstruction of the SPEG focal plane, the hybrid γ array, the data acquisition and particle identification.

2.1 Radioactive Ion Beam Production

Radioactive Ion Beams (RIBs) are produced in flight at the GANIL ‘*Grand Accélérateur National d’Ions Lourds*’ facility, based at Caen, France (see Fig. 2.1). In-flight

radioactive beam production is a three stage process; primary beam production, projectile fragmentation and fragment separation.

2.1.1 Primary Beam Production

There are a number of primary beams available for use at GANIL. The experiment reported in this thesis used ^{36}S , a neutron-rich stable beam ideal for the production of light neutron-rich exotic nuclei. The beam was originally extracted from SF_6 gas, injected into an ion source chamber. Using the Electron Cyclotron Resonance technique, microwaves are used to impart energy into the system, creating a hot plasma by accelerating the atomic electrons until they dissociate, leaving the ions in high charge states. The plasma is confined by a combination of radial and axial magnetic fields. A frequency of microwave specific to the frequency at which the electrons gyrate throughout the magnetic field is applied. This resonance acceleration causes the stripping of more electrons from the atom, leaving the Sulphur ions in very high charge states. A high voltage is then used to extract these Sulphur ions from the magnetically confined plasma.

The C01 cyclotron is used for the initial acceleration of this beam, which is then transferred to a set of two separated-sector cyclotrons, achieving a beam of ^{36}S at 72 A.MeV.

2.1.2 Projectile Fragmentation

The 72 A.MeV ^{36}S beam is focused by the first superconducting solenoid of the SSI (Superconducting Intense Source for Secondary Ions) [3] pair to impinge on a 442 mg cm^{-2} ^{12}C production primary target. The primary target is positioned between two super-conducting solenoid coils, which provide a maximum field of 11 T, with a maximum magnetic rigidity of 2.88 Tm. The first solenoid ‘SOL1’ is used to focus the incoming ^{36}S beam in a spot of 0.4 ± 0.2 mm diameter on the target. The second solenoid ‘SOL2’ reduces beam spread, enabling the collection of secondary beam ions to increase (to a factor 10 or more). Cooling for the target is provided by a closed circuit of liquid helium at 4.6 K. Additional measures taken to avoid the heat extremes which would otherwise sublime the target include rotation of the target at 3000 rpm – spreading the radiated heat over a much larger area than the beam spot. A very large acceptance angle of up to ± 80 mrad is achieved with a small emittance of 16π mm mrad due to the small beam spot. The SSI target may be rotated relative to the beam direction ($\theta \leq 45^\circ$), which allows a variable thickness of the target to allow optimum fragment production.

2.1.3 Fragment Separation

The projectile fragmentation reaction produces a wide range of nuclei, only a fraction of which occupy the region of interest in this thesis. Following fragmentation at the primary target, a cocktail of different species is produced as the secondary ion beam. To separate out the species of interest (neutron-rich Oxygen – Magnesium)

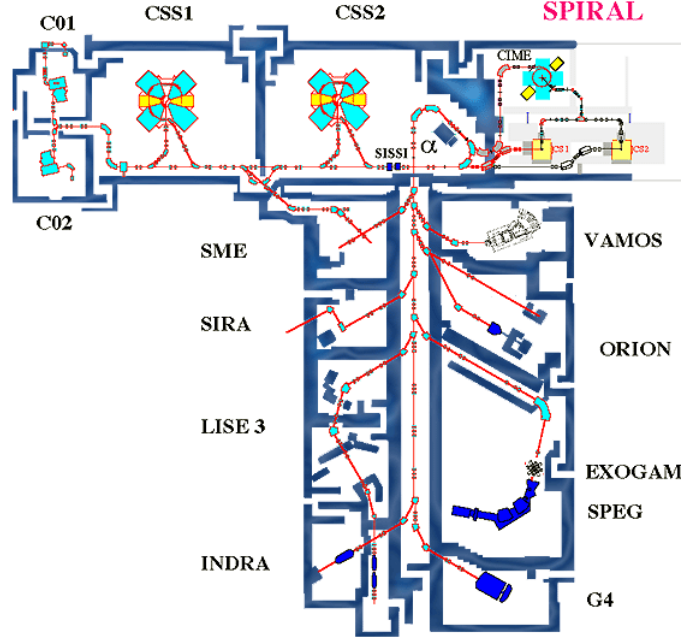


Figure 2.1: General layout of GANIL, indicating the location of SSSI.

the ALPHA spectrometer [50] is employed, where the first dipole acts to optimise production, the second dipole tuned to the magnetic rigidity corresponding to the area of interest.

The relationship is

$$B\rho = \frac{\gamma m_0 v}{q}, \quad (2.1)$$

where $B\rho$ is the magnetic rigidity of a particle with rest mass m_0 , charge q , velocity v and γ – the Lorentz factor (see Eq. 3.2). There are a number of species that share the same region of $B\rho$, and in order to filter out the undesired fraction, a $251\mu\text{m}$ Beryllium degrader was situated between the two dipoles of the ALPHA spectrometer. The degrader absorbs a certain fraction of the secondary beam particle's energy, in

accordance with,

$$\frac{dE}{dx} \propto \frac{AZ^2}{E}. \quad (2.2)$$

While the $B\rho$ of the desired/undesired species may be the same, their energy loss through the degrader differs. The second dipole is tuned to the modified $B\rho$ of the desired species after their energy loss in the degrader to further filter the secondary beam. A further function of the degrader is to reduce the momentum spread of the secondary beam, by careful choice of tapering the material thickness, which results in the same AZ particles with a higher momentum passing through a thicker section of the degrader, and therefore depositing a larger fraction of energy (and vice versa) in order to lower each species spread in momentum (Δp), the momentum dispersion $\Delta p/p$ limited to $\pm 0.5\%$.

2.2 Experimental Detection Setup

2.2.1 Overview of Experimental Setup

Shown in Fig. 2.2 is a schematic representation of the experimental setup from secondary beam production through to detection. The selected cocktail beam exits the ALPHA spectrometer and is focused by the analyser dipole to be achromatic at the reaction target. The beam is then focused via two quadrupoles, before passing through the trifoil detector, followed by “little” drift chambers (LDCs) to be incident on a ^{12}C , $\sim 171 \text{ mg/cm}^2$ thick secondary ‘reaction’ target.

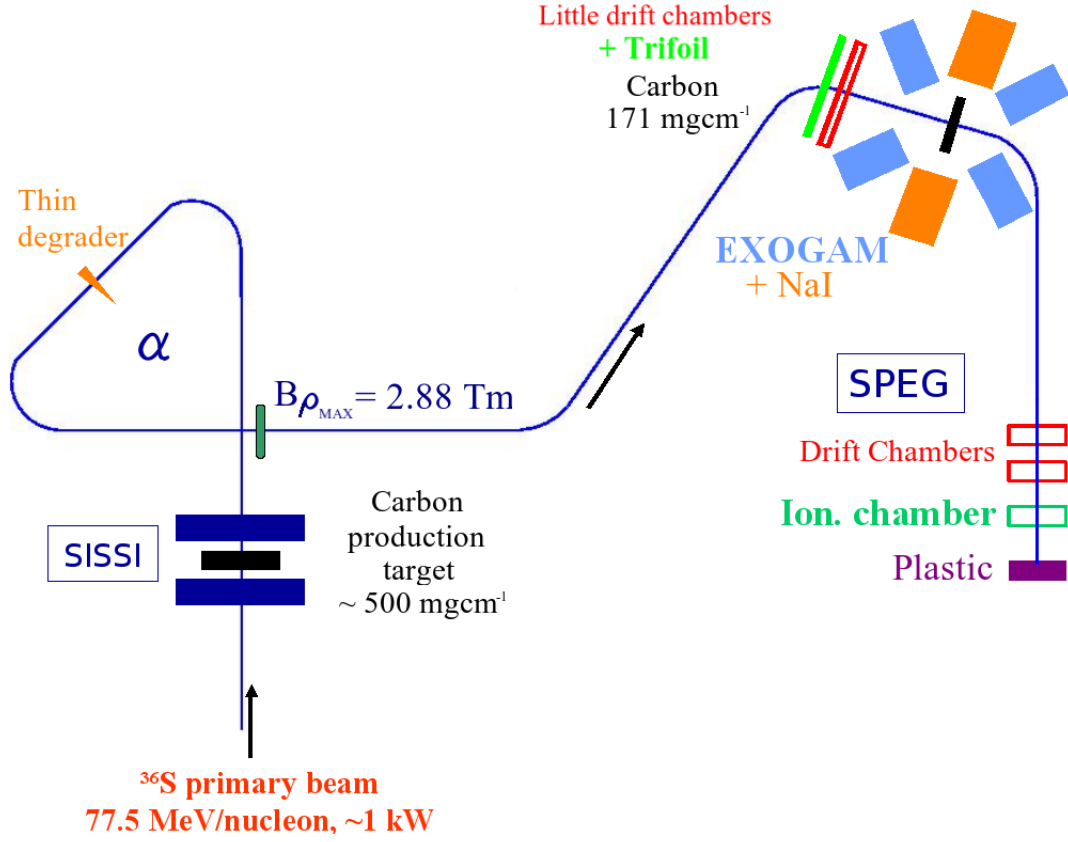


Figure 2.2: Experimental setup, from secondary beam production to SPEG.

At the reaction target a small fraction of the beam particles undergoes single-neutron removal ‘knockout’ reactions. The $B\rho$ of the SPEG spectrometer is set to $\sim 2.45 \text{ Tm}$, tuned to the region of A/Z and momentum of the reaction products of interest. The reaction products, or core fragments, were identified by the standard detection set-up of SPEG; a set of two drift chambers to measure position, X , Y , an ionisation chamber to measure energy loss, ΔE , and a plastic scintillator detector to measure the residual energy, E , where the beam terminates. Surrounding the secondary target is a hybrid array of γ detectors, employed to detect coincident γ rays with an event-by-event identification of the ions detected in SPEG using $\Delta E : E$ and

time of flight information.

2.2.2 The SPEG Spectrometer

In order to identify the different nuclides of interest and measure their longitudinal momentum distribution, the SPEG spectrometer is utilised. Shown in Fig. 2.3 are the core components which constitute SPEG, DA – the analyser dipole, Q1 – the entrance quadrupole, S1 – a sextupole and a set of two dipoles, D1 and D2, and Q2 – an exit quadrupole [10]

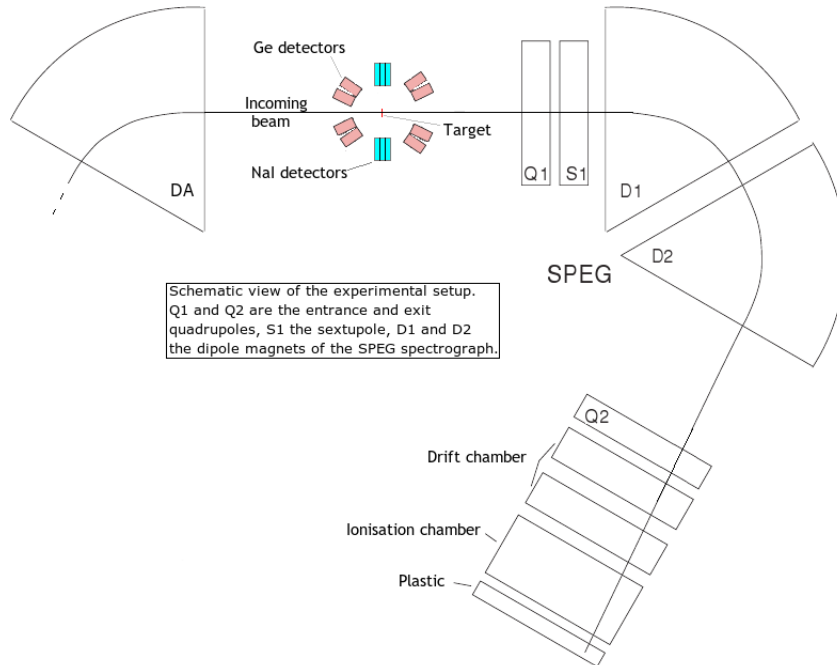


Figure 2.3: SPEG High-Resolution Mass Spectrometer, adapted from [9].

For the experiment described in this thesis, SPEG operated achromatically at the intermediate focal plane (where the reaction target was positioned) in order to

optimise fragment production by employing the analyser dipole to focus the secondary beam at the target. The entrance quadrupole controls the vertical optics inside the dipole and is horizontally defocusing. The vertical focusing occurs at the exit of D2. The exit quadrupole determines the angular dispersion at the focal plane. Aberrations (x/θ^2) in the magnetic field due to dipole exit face curvature, kinematic conditions, etc, must be corrected for. This is accomplished via the use of S1 (the entrance sextupole) which can be adjusted to correct for the (x/ϕ^2) aberration with second order corrections, after which the first dipole (D1) exit face curvature can be used to correct the (x/θ^2) aberration. The second dipole (D2) exit face curvature then determines the tilt angle of the focal plane. The acceptance of the device is $\pm 4^\circ$ in both the vertical and horizontal direction, the mean bending radius being 2.4 m. At the final ‘dispersive’ focal plane, SPEG was set to operate chromatically. This was in order to distribute the reaction products spatially along the focal plane, depending on their longitudinal momentum. In order to reconstruct the particle trajectory and thus their position in the dispersive SPEG focal plane, two sets of drift chambers were utilised. Following calibration, initial values at the focal plane are needed in order to reconstruct each ions trajectory following the reaction target. These values are X_i (Y_i), which give the value on the horizontal (vertical) axis, θ_i (ϕ_i) which give the angle in the horizontal (vertical) axis with respect to the incident beam direction and l_i (δ_i) which gives the deviation with respect to a central trajectory (momentum) value. The final horizontal position at the focal plane is denoted as X_f , which can be described as a function of the initial value inputs (denoted subscript i) and the geometry of the

spectrometer,

$$X_f = f(X_i, \theta_i, Y_i, \phi_i, l_i, \delta_i). \quad (2.3)$$

Following a Taylor expansion, neglecting terms higher than first order, the horizontal trajectory an ion follows in a magnetic element may be defined as

$$X_f = \left(\frac{\partial f}{\partial X} \right) X_i + \left(\frac{\partial f}{\partial \theta} \right) \theta_i + \left(\frac{\partial f}{\partial Y} \right) Y_i + \left(\frac{\partial f}{\partial \phi} \right) \phi_i + \left(\frac{\partial f}{\partial l} \right) l_i + \left(\frac{\partial f}{\partial \delta} \right) \delta_i. \quad (2.4)$$

This can be done for any of the input parameters used. In order to describe the optical parameters in a format which lends itself to calculations, a transfer matrix is used. By approximating each term to first order, a matrix may be constructed to transform the initial parameters to their final values. An example of a transfer matrix is shown in Eq. 2.5.

$$\begin{pmatrix} X_f \\ \theta_f \\ Y_f \\ \phi_f \\ l_f \\ \delta_f \end{pmatrix} = \begin{pmatrix} R_{11} & R_{12} & R_{13} & R_{14} & R_{15} & R_{16} \\ R_{21} & R_{22} & R_{23} & R_{24} & R_{25} & R_{26} \\ R_{31} & R_{32} & R_{33} & R_{34} & R_{35} & R_{36} \\ R_{41} & R_{42} & R_{43} & R_{44} & R_{45} & R_{46} \\ R_{51} & R_{52} & R_{53} & R_{54} & R_{55} & R_{56} \\ R_{61} & R_{62} & R_{63} & R_{64} & R_{65} & R_{66} \end{pmatrix} \begin{pmatrix} X_i \\ \theta_i \\ Y_i \\ \phi_i \\ l_i \\ \delta_i \end{pmatrix} \quad (2.5)$$

Each of the matrix elements above represents a characteristic of the spectrometer to a first order approximation. Below some of the more important terms are summarised, with the notation *z_{foc}* referring to the final focal plane.

$$R_{12} = \left(\frac{\partial f}{\partial \theta} \right)_{z_{foc}} \quad (2.6)$$

with a value of zero, defines the focal plane. Independent of trajectory, identical ions with identical longitudinal momentum should diverge at the same X position in the focal plane.

$$R_{11} = \left(\frac{\partial f}{\partial X} \right)_{z_{foc}} \quad (2.7)$$

is the magnification of the image at the focal plane in the horizontal direction. R_{33} is the value for the vertical direction.

$$R_{22} = \left(\frac{\partial f}{\partial \theta} \right)_{z_{foc}} \quad (2.8)$$

relates to the magnification of the horizontal angle. R_{44} similarly relates to the vertical angle.

$$R_{16} = \left(\frac{\partial f}{\partial \delta} \right)_{z_{foc}} \quad (2.9)$$

refers to the horizontal dispersion in momentum along the focal plane. The analogous vertical term is R_{36} . The values units are cm/%.

$$R_{26} = \left(\frac{\partial f}{\partial \phi} \right)_{z_{foc}} \quad (2.10)$$

refers to the angular dispersion in the horizontal direction, with units mrad/%. For the vertical direction the element is R_{46} . An important factor to consider is the resolution of the SPEG spectrometer and how it is affected by the emittance of the beam. Only the horizontal terms in the transfer matrix can be considered, discounting the dispersion and magnification in the vertical direction (i.e. the Y and ϕ related elements). This simplifies the spectrometer to only consider the X position. This simplification yields the expression

$$X_f = \frac{\partial X}{\partial \delta} \delta_i + \frac{\partial f}{\partial X} X_i. \quad (2.11)$$

As the focal plane is intended to spatially separate identical particles with different momentum along the X -axis, the resolution of momentum is dependent on the resolution of the horizontal position (X_i) in SPEG. There are two modes of operation in which SPEG can be utilised. Achromatic mode serves to focus identical particles with different energy on the same point on the focal plane. Chromatic mode causes identical particles with different trajectories, but the same energy, to be focused. At the intermediate focal plane Achromatic mode is employed to focus the beam onto the reaction target. At the dispersive focal plane Chromatic mode is used in order to observe the particles momentum in relation to their position at the focal plane. A schematic of the SPEG optics is shown in Fig. 2.4.

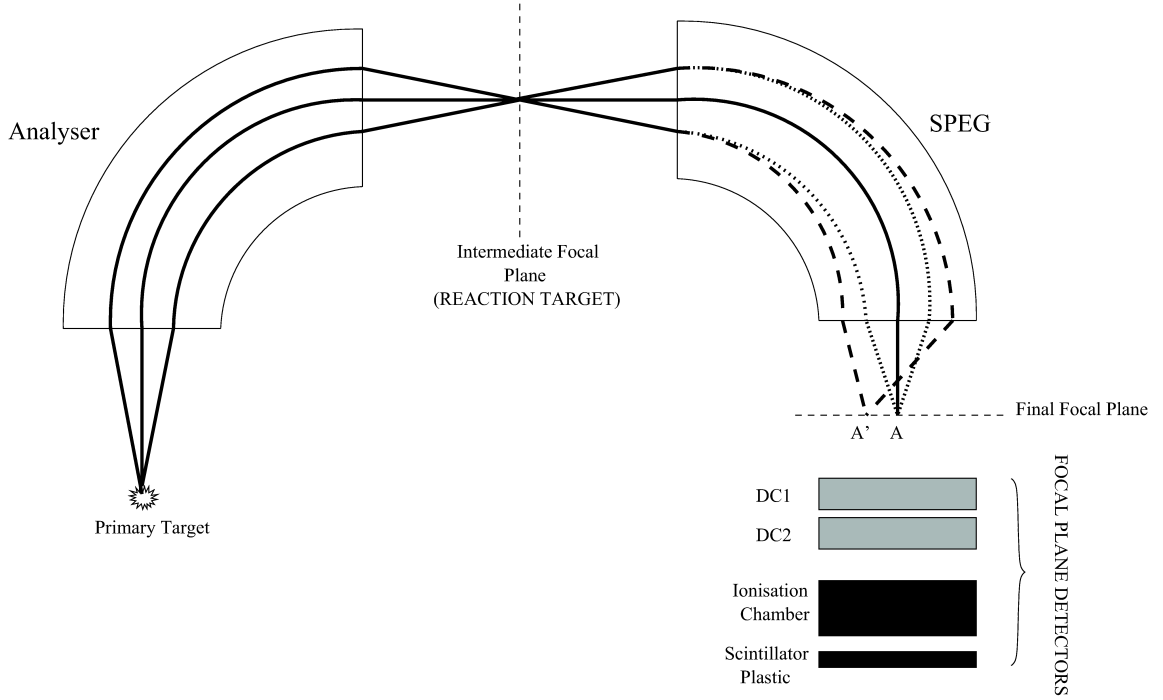


Figure 2.4: Optics of SPEG, set in Achromatic mode for the intermediate focal plane and Chromatic mode for the dispersive (final) focal plane.

2.3 Direct Beam and Fragment Identification

Using a time-of-flight (TOF) method necessitates a long flight path (~ 100 m) to achieve good resolution between ions of a similar mass and charge. The TOF was measured relative to the radio-frequency of the cyclotron and the SPEG terminating plastic scintillator. An average flight time for the ions is typically in the region of $1 \mu\text{s}$, which enables the most exotic, short-lived isotopes to be reached. Having no significant lifetime limitations, the SPEG spectrometer can be employed with very low secondary beam intensities (0.01 particles/second), making available very exotic nuclei close to the neutron dripline, in the region $A \sim 10 - 40$. The angular acceptance

of SPEG is $\pm 2.3^\circ$, the momentum acceptance $\sim 7\%$ [10]. Positioned in front of the reaction target was a thin, plastic ‘trifoil’ detector. The purpose of the trifoil was three-fold. It was intended as an additional means of particle identification ‘PID’ giving a time of flight between itself and the terminating plastic. Also it was used as a data acquisition trigger as well as giving information on the beam rate. The ionisation chamber was used to enable particle identification, spanning the length of the SPEG focal plane. The chamber was filled with Isobutane gas at a pressure of 400 mb. This pressure fluctuated due to problems with gas regulation and a correction was employed to account for this in the data analysis (see Section 2.7). The energy loss (ΔE) detected by the ionisation chamber as particles pass through it is expressed by the Bethe–Bloch formula:

$$-\frac{dE}{dx} = \frac{4\pi Z^2 e^4}{m_e v^2} N z \left[\ln \left(\frac{2m_e v^2}{I} \right) - \ln(1 - \beta^2) - \beta^2 \right], \quad (2.12)$$

where $Z(z)$ is the number of protons in the incident ion (absorber material), $N(I)$ is the number density (ionisation potential) of the absorber material, m_e is the electron rest mass and β is the velocity of the incident ion expressed as $\beta = v/c$, a fraction of the speed of light in a vacuum.

Following their progression through the ionisation chamber the ions encounter a plastic scintillator of sufficient thickness to prevent penetration, absorbing the remaining energy carried by the incident ions. The energy is converted in the scintillator into light which is directly proportional to the amount of energy absorbed. This light is then detected by a photo-multiplier tube at either end of the plastic scintillator, the total energy (E) related to the two signals (E_L , E_R) via

$$E = \sqrt{E_L \cdot E_R}. \quad (2.13)$$

Due to problems with the E_L signal, E was taken as E_R for the experiment described in this thesis. With the energy loss (ΔE) and the residual energy (E) for each ion it is possible to use a 2D $\Delta E:E$ plot that clearly separates the ions isotopically for particle identification (see Fig. 2.5).

2.3.1 Identification Gates

A number of 2D gates was made to identify the reaction fragments using a number of detectors. Shown in Figs. 2.5, 2.6, 2.7 and 2.8 is the identification for ^{24}F following single-neutron removal from ^{25}F .

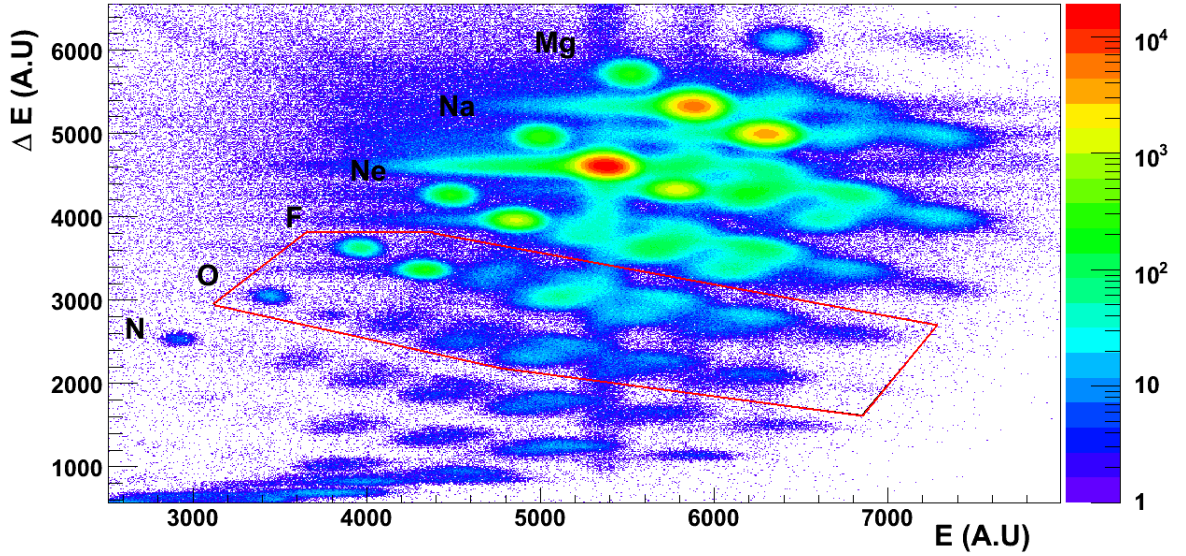


Figure 2.5: ΔE vs. E for all ions. A gate for the Fluorine and Oxygen isotopes is shown.

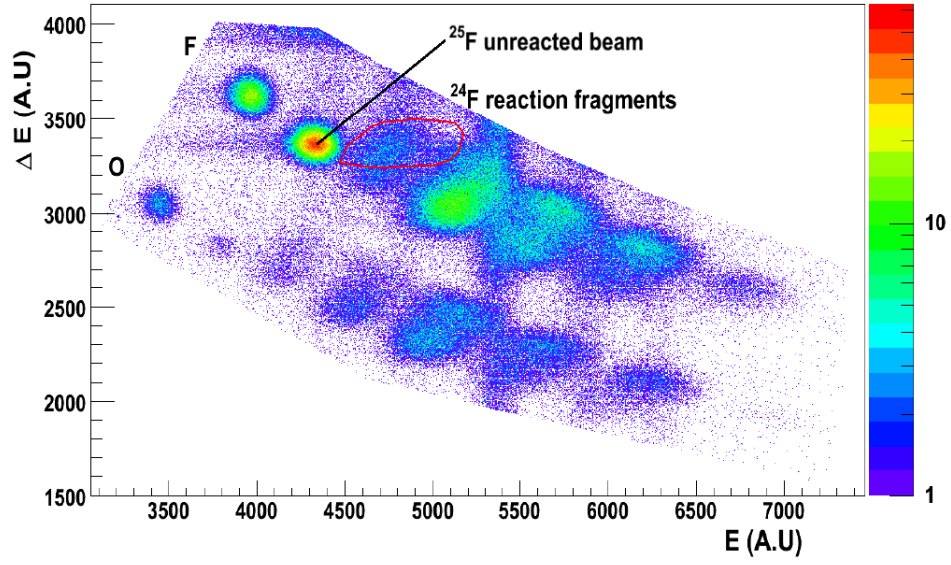


Figure 2.6: ΔE vs. E for the Fluorine and Oxygen isotopes. A gate for the ^{24}F reaction fragment is shown.

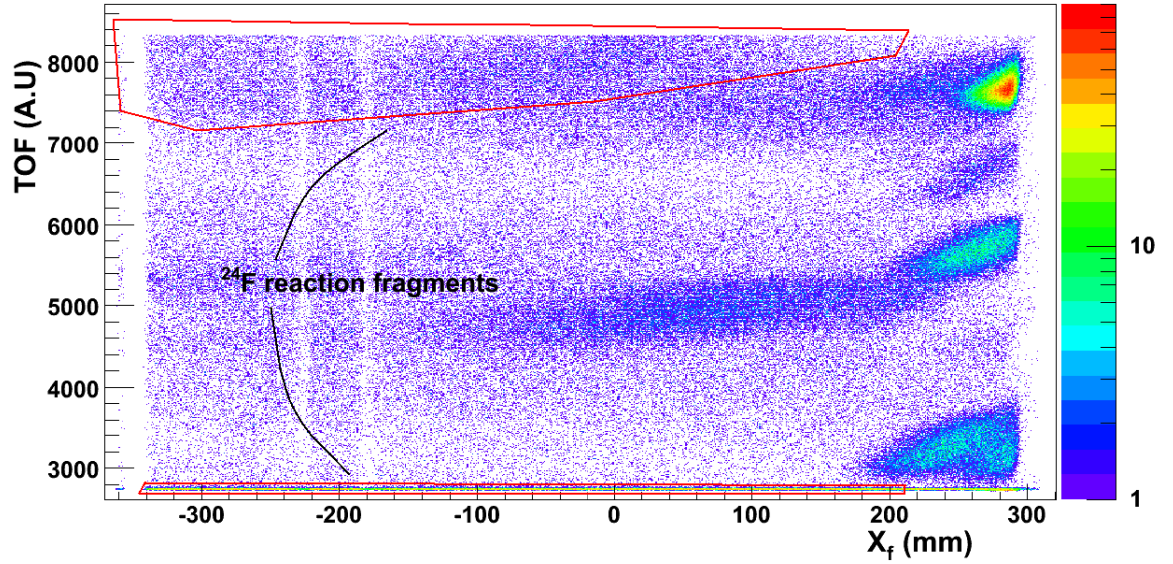


Figure 2.7: X_f vs. TOF for the Fluorine and Oxygen isotopes. Two gates for the ^{24}F reaction fragment is shown.

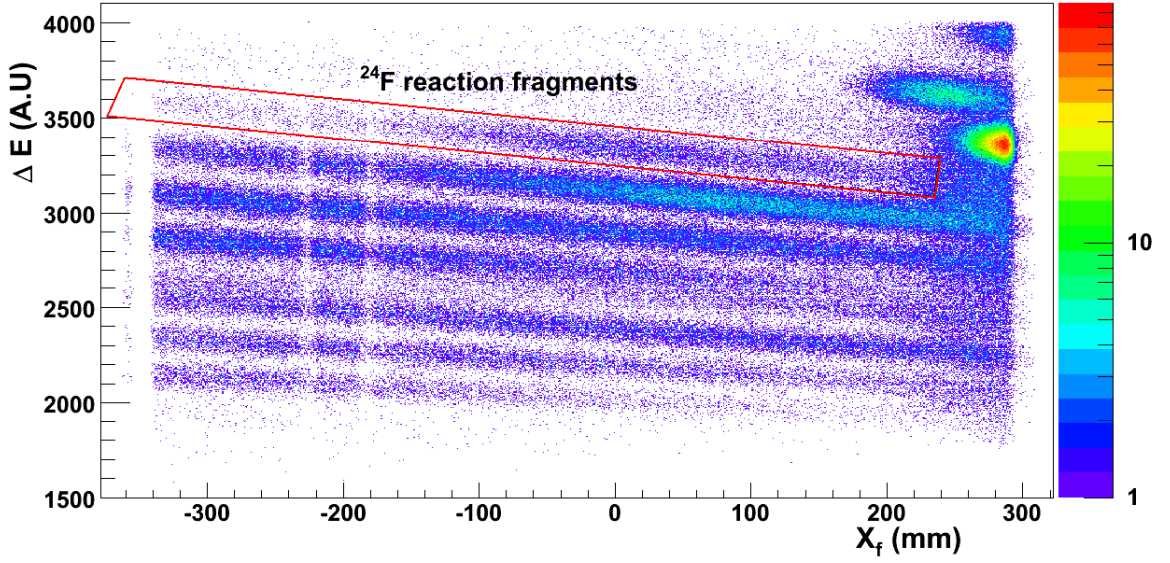


Figure 2.8: ΔE vs. X_f for the Fluorine and Oxygen isotopes. A gate for the ^{24}F reaction fragment is shown.

In Fig. 2.7 there are two gates shown for one fragment. The time of flight was set for a certain range, the intention being that any values exceeding that range would overlap to the beginning. An unresolved error resulted in the ions overlapping the TOF range being placed in a very narrow region at the start of the range, which reduced the accuracy for the identification of the ions in these cases.

Fig. 2.8 shows the recoil fragments stretching across X_f , the SPEG focal plane. On the right-hand-side of the figure the intense regions correspond to unreacted ions that were partially caught by the acceptance of SPEG. The 1D projection in X_f of the gated region in Fig. 2.8, in coincidence with the other identification gates, would be the LMD for the ^{24}F recoil fragment.

2.3.2 The Hybrid γ -ray Array

The γ -ray array was positioned around the reaction target in order to detect the energies of γ rays released upon the prompt decay of nuclei following single-neutron removal reactions. The hybrid array consists of eight EXOGAM Germanium detectors [5, 52, 60], four at forward angles and four at backward angles, centred at 45° and 135° to the beam respectively. Twelve hexagonal Sodium Iodide detectors were positioned in clusters of three at 90° to the beam. Shown in Fig. 2.9 are the EXOGAM clovers and the hexagonal NaI detectors. At the centre of the array is located a carbon fibre shell target chamber, which housed the target holder and reaction target, the beam passing left to right (see Fig. 2.9).

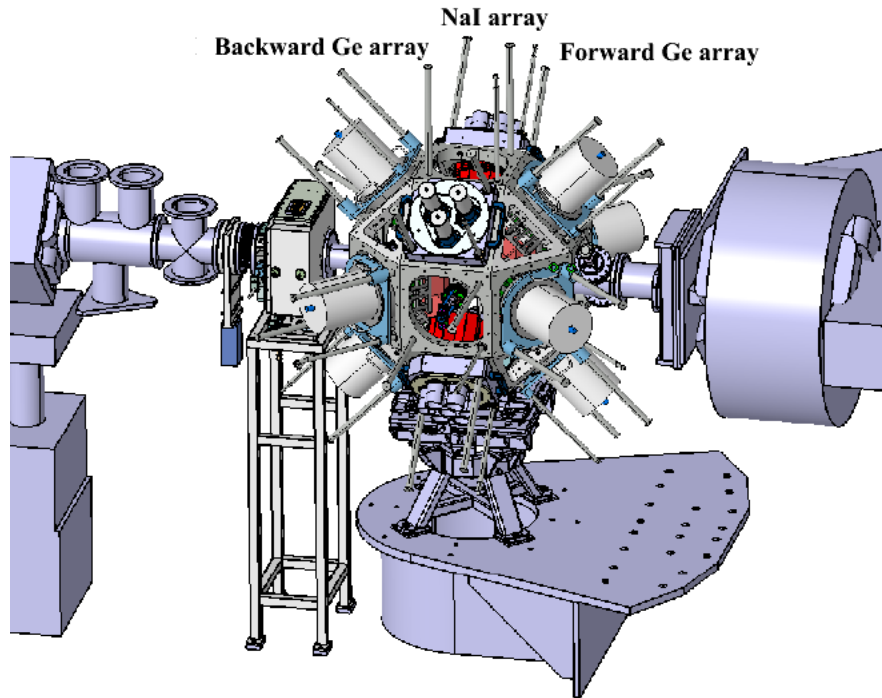


Figure 2.9: Hybrid γ -ray Array, beam direction from left to right.

2.3.3 EXOGAM

Surrounding the secondary target were eight EXOGAM high-purity germanium detectors. Four of the EXOGAM clovers (forward array) were positioned at an angle of 45° from the reaction target, with respect to the beam direction at a target – detector distance of 215 mm. The other four EXOGAM detectors (backward array) were positioned at an angle of 135° with a distance of 134 mm from the target, apart from one backward clover, which was stuck at 174 mm. The EXOGAM detectors were placed at target – detector distances previously determined to give $\sim 2 - 3\%$ detector efficiency at $E_\gamma = 1.3$ MeV for the separate forward and backward arrays, based on Geant4 [1] Monte Carlo simulations. Germanium detectors yield excellent energy resolution, but their detection efficiency suffers at higher γ -ray energies.

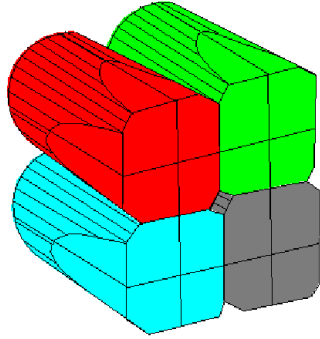
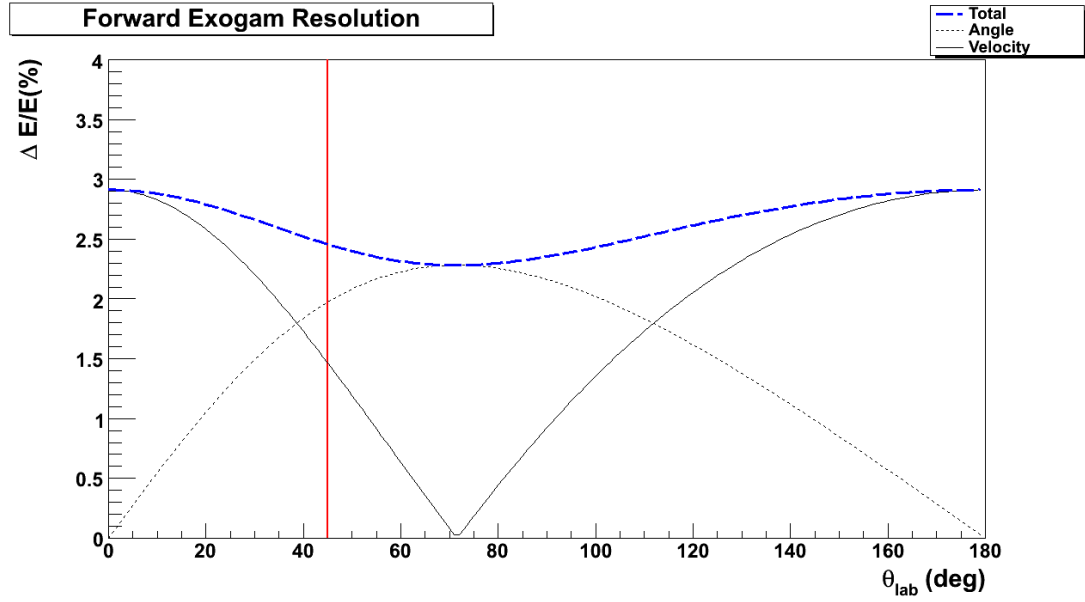


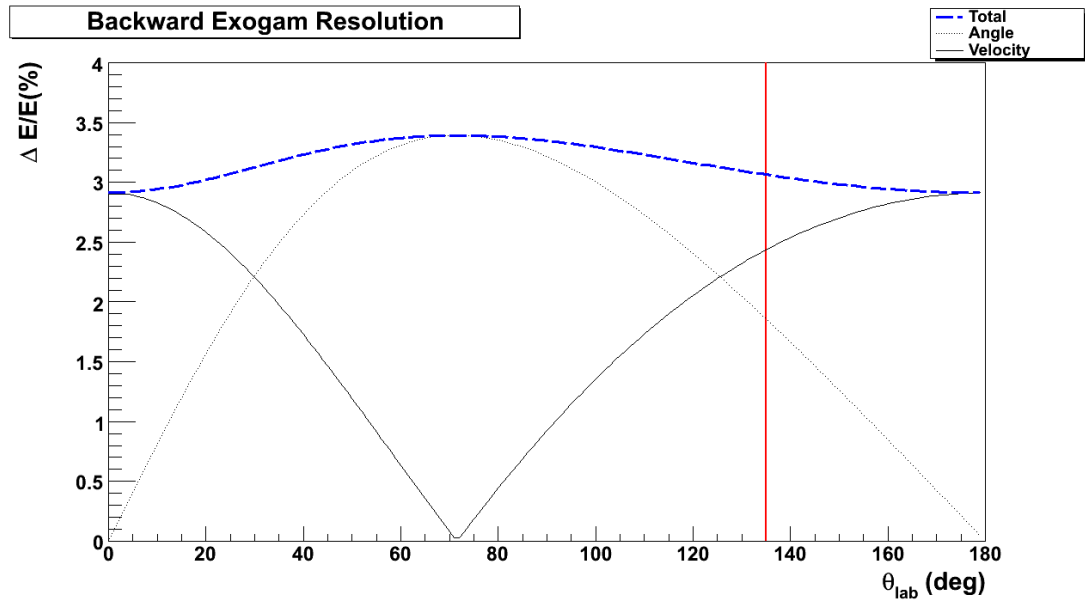
Figure 2.10: One EXOGAM Clover, comprising four segmented coaxial detectors.

An important factor in reducing the Doppler broadening is reducing the uncertainty of the angle from the beam at which the first interaction occurred. Physical division of the detector is necessary to reduce this opening angle, shown by the four tapered

coaxial Germanium crystals which comprise one Clover. Further reduction of the Doppler Broadening is achieved via electronic segmentation, which divides each crystal into four quadrants, shown in Fig 2.10. Fig. 2.11 shows the simulated energy resolution for the forward and backward EXOGAM arrays. The energy lost by the incident ion while traversing the target is included in the simulation. The vertical line on each figure represents the mid-point angle of the clovers in their respective arrays. The velocity of the ion was set as $\beta = 0.317(26)$.



(a) Forward EXOGAM array.



(b) Backward EXOGAM array.

Figure 2.11: Simulated Energy Resolution for EXOGAM. The line labelled “Velocity” refers to the contribution from the moving source. The line labelled “Angle” refers to the contribution from the EXOGAM segment opening angle, “Total” being the combined energy resolution.

2.3.4 The NaI Array

The Sodium Iodide (NaI) array consists of 12 hexagonal detectors, positioned in clusters of three around the secondary target at 90° from the beam direction. Each cluster is set at 90° from each other in the X - Y plane. Fig. 2.12 shows one such NaI cluster.

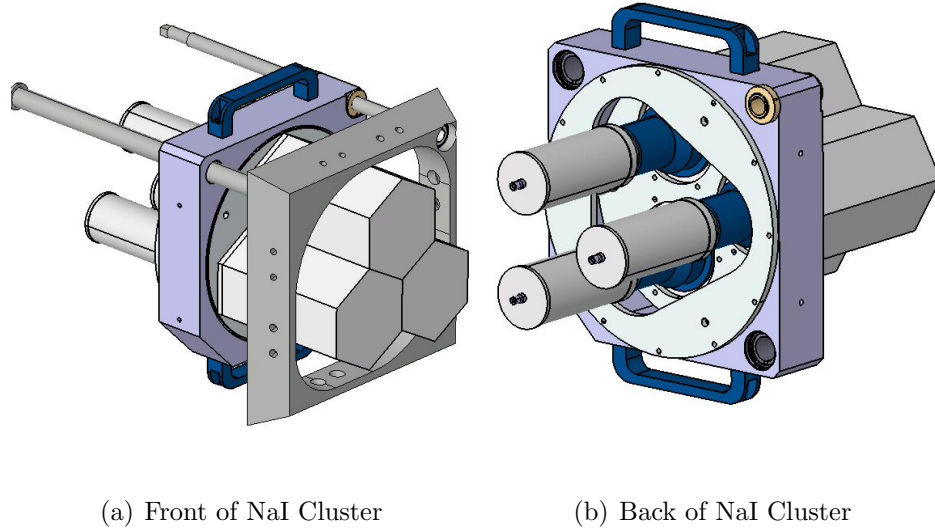


Figure 2.12: Schematic of Sodium Iodide detectors.

NaI was employed mainly because of its high detection efficiency, retaining this better at higher γ -ray energy than Germanium. The detectors were hexagonal, with a 62.5 mm radius and 202 mm length. They were encased in Aluminium and Thallium doped, as this reduces the possibility of the reabsorption by the material of an emitted photon.

2.4 γ -ray Array Calibration

2.4.1 EXOGAM

The EXOGAM detectors were calibrated for both energy and efficiency in order to correctly measure the emitted decay energy from the prompt decay of reaction fragments produced in excited states in order to determine the exclusive cross sections and exclusive momentum distributions. Table 2.1 lists the energies used, accompanied by the source nuclide. The asterisked energies were also used for the Sodium Iodide array calibration. Each of the 32 central contacts and 128 segments were calibrated

Table 2.1: Calibration Sources.

Source	E_γ (keV)	Intensity (%)	Source	E_γ (keV)	Intensity (%)
^{152}Eu	244.70	7.58	^{56}Co	1238.28*	67.60
^{152}Eu	344.28	26.50	^{60}Co	1332.50*	99.97
^{137}Cs	661.66*	85.10	^{56}Co	1360.22	4.33
^{152}Eu	778.90	12.94	^{152}Eu	1408.01	21.01
^{56}Co	846.77*	100.00	^{40}K	1460.83	11.00
^{152}Eu	964.08	14.61	^{56}Co	1771.35*	15.69
^{56}Co	1037.84	13.99	^{56}Co	2034.76	7.88
^{152}Eu	1112.07	13.64	^{56}Co	2598.46*	17.28
^{60}Co	1173.24*	99.97	^{56}Co	3253.42*	7.93

employing a 3rd-order polynomial fit. The relationship was found to be close to linear, as expected. As an example, the calibration for Clover 0 is shown in Fig. 2.13. The fit for each central contact is shown left, the segments shown right.

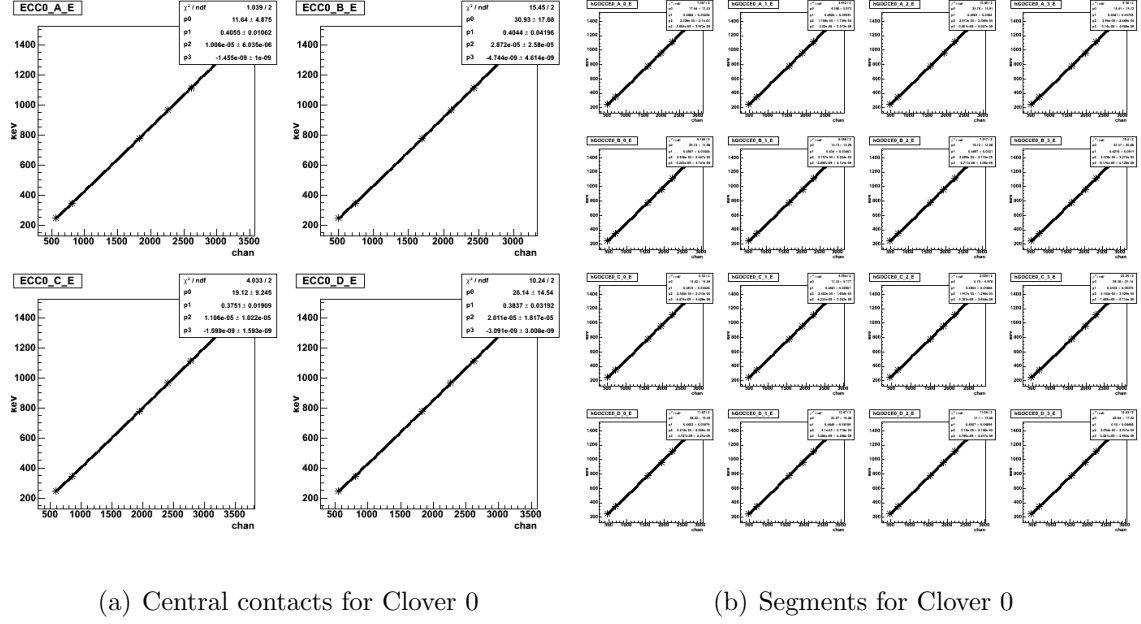


Figure 2.13: EXOGAM energy Calibration.

The efficiency calibration was also done (Fig. 2.14). One issue to overcome was that the activity of the ^{56}Co source was unknown. The efficiency calibration was firstly done using the ^{152}Eu , ^{137}Cs and ^{60}Co sources, with a range in energy from 0.24–1.41 MeV. There were four ^{56}Co decay energies of significant intensity that fell into this lower energy range. These were used with the 245–1408 keV efficiency calibration to calculate the ^{56}Co source activity, using a weighted mean with errors dependent on the fit and the respective peak integrals. The ^{56}Co source was then used to complete the efficiency calibration up to the 3.25 MeV point. This was done separately for each

clover. The separate clover efficiency calibrations were then summed to give efficiency calibrations for the forward, backward and total array respectively.

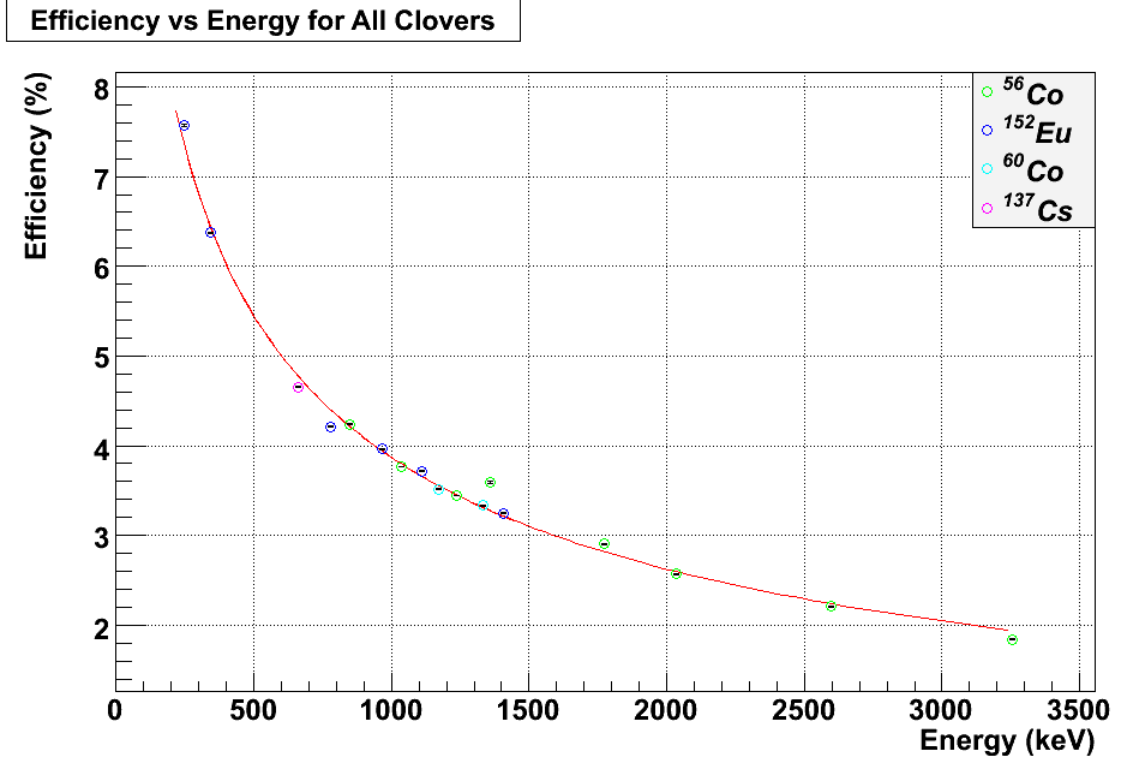


Figure 2.14: Efficiency vs. Energy for the entire EXOGAM array.

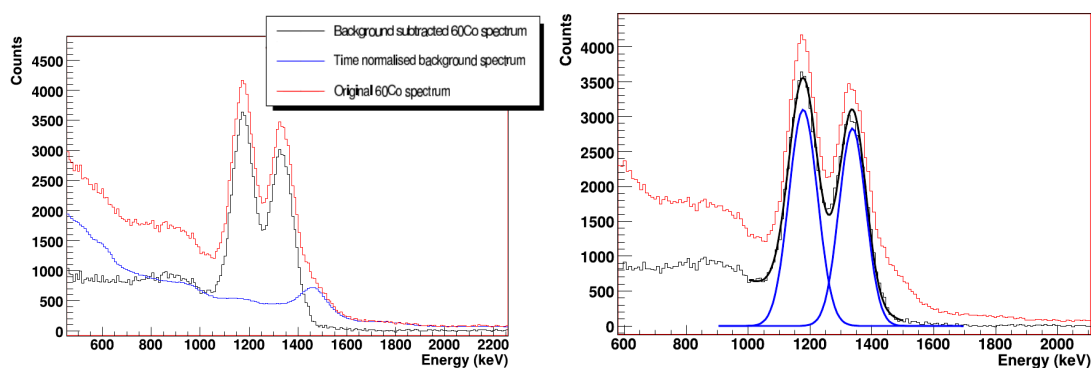
The efficiency was fitted as

$$\varepsilon_0 = \exp \left[(p0 \cdot (\log(E))^2 + p1 \cdot \log(E) + p2) \right], \quad (2.14)$$

for both the EXOGAM and NaI arrays [38].

2.4.2 NaI Array

Of the twelve Sodium Iodide detectors, two proved to have insurmountable problems. This left ten functional NaI detectors in the array. For the ^{56}Co and ^{137}Cs spectra a first order background in conjunction with a Gaussian fit was used. For the ^{60}Co the similarity in peak energies in addition to the 1461 keV ^{40}K background transition gave some difficulties in resolution. In order to extract realistic peak integrals a two Gaussian fit was used after subtracting a time scaled background run (see Fig. 2.15).



(a) ^{60}Co with scaled background.

(b) Two Gaussian fit.

Figure 2.15: NaI fitting technique for ^{60}Co .

A selection of γ -ray energies (shown asterisked in Table 2.1) was used in the efficiency calibration. With each useable Sodium Iodide detector calibrated for efficiency it was possible to sum their efficiency values at each energy to give the efficiency calibration for the total NaI array, shown in Fig. 2.16.

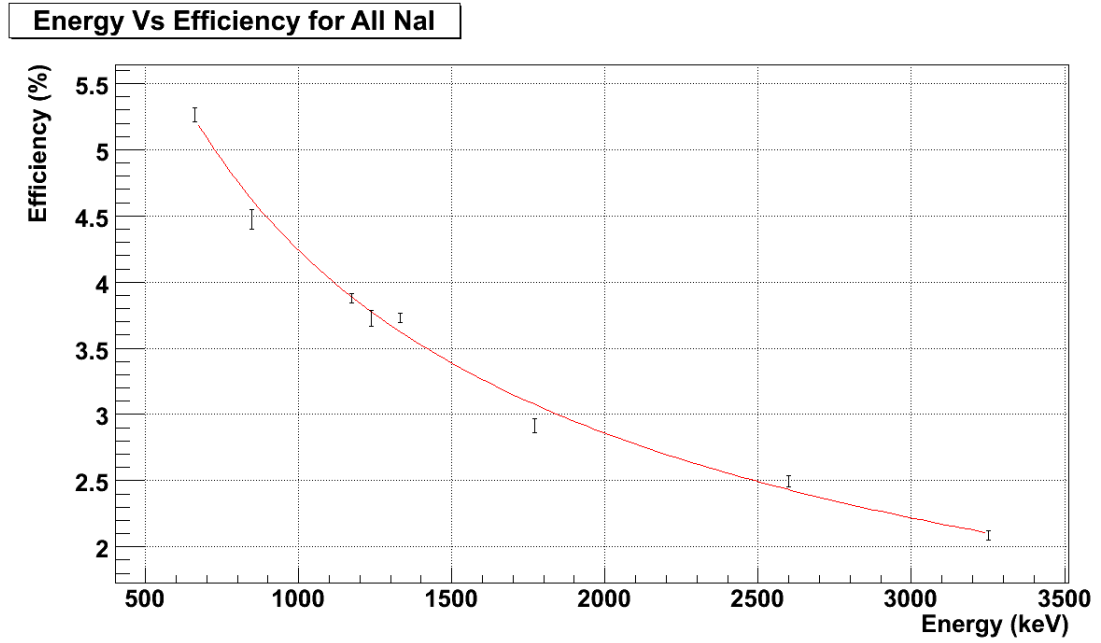


Figure 2.16: Energy vs Efficiency for the total NaI array.

2.5 SPEG Calibrations

Focal Plane

In order to ensure that the paths of each particle passing through the spectrometer are correctly reconstructed with the transfer matrix a full reconstruction of the focal plane must be performed. A schematic illustrating the basic focal plane coordinates is given in Fig 2.17.

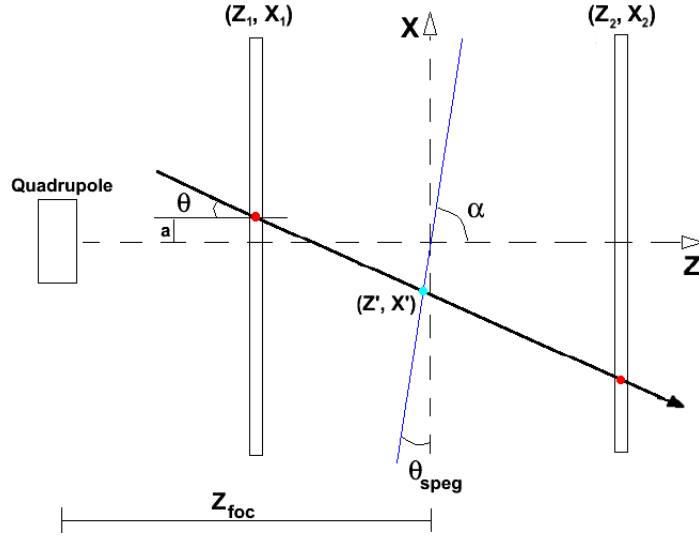


Figure 2.17: SPEG focal plane schematic.

In Fig 2.17 the dark arrow represents the reconstructed particle trajectory. The SPEG focal plane angle relative to the X -axis is denoted by θ_{SPEG} , a value of approximately 8° . The angle the trajectory makes perpendicular to the first drift chamber is given by θ , the offset distance from the trajectory to the centre of the first drift chamber is given by a . The trajectory follows a straight path after exiting the spectrometer. Its position on the X -axis is given by

$$x = z \tan(\theta) - a. \quad (2.15)$$

The x coordinate at the focal plane is given by

$$x' = (z' - z_{foc}) \tan(\alpha), \quad (2.16)$$

where z' is the z coordinate at the focal plane, z_{foc} is the distance between the last quadrupole and the centre of the focal plane and α the angle between the focal plane and the z -axis.

At $x = x'$ and $z = z'$ the particle's trajectory and the focal plane intersect. Combining Eqs. 2.15 and 2.16 gives

$$z \tan(\theta) = (z' - z_{foc}) \tan(\alpha) - a, \quad (2.17)$$

which can be rearranged to give

$$z' = \frac{-z_{foc} \tan(\alpha) - a}{\tan(\theta) - \tan(\alpha)}. \quad (2.18)$$

Substituting this into Eq. 2.16 gives

$$x' = \left(\frac{-z_{foc} \tan(\alpha) - a}{\tan(\theta) - \tan(\alpha)} - z_{foc} \right) \tan(\alpha). \quad (2.19)$$

Assuming that the value used for z_{foc} is correct, the x and z coordinates of the particle at the focal plane can now be determined. The value of z_{foc} was taken to be 152 cm, which was checked by plotting θ against X_f for data taken with a ^{36}S beam incident on a ^{208}Pb target directly followed by a mask. The purpose of the lead target was to spread the beam over an opening angle sufficient to traverse all holes in the mask. The incident beam ions are light with respect to the target ^{208}Pb nuclei, resulting in a low transfer of energy from the incident ion to the target. This means that across the small angular range between the reaction target and the holes in the mask there is only a small energy spread for the different beam trajectories. This energy uniformity results in the different beam trajectories intersecting at the focal plane. Masks are essentially metal sheets with geometrically precise holes positioned throughout. In the geometric pattern of the holes, one was left out to aid orientation of the reconstructed image.

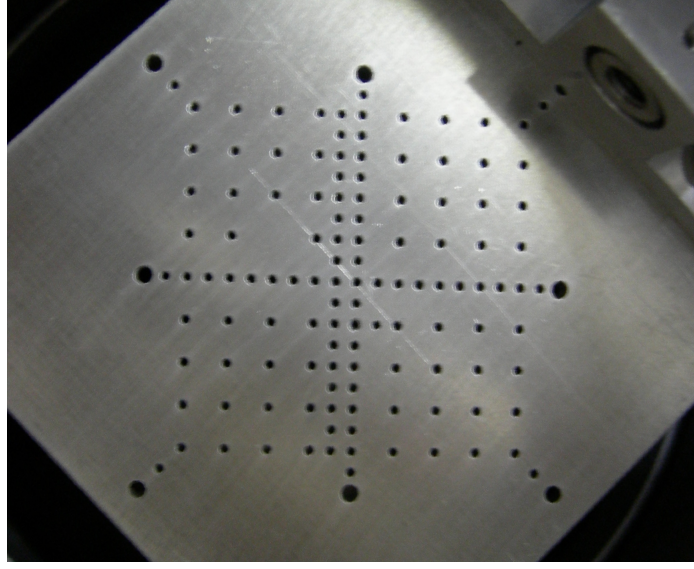


Figure 2.18: Calibration Mask.

With the mask in place, five data sets with a constant beam $B\rho$ were taken at varying values of $B\rho^{ref}$ for the dipoles D1 and D2 (see Fig. 2.3) directly following the reaction target; 2.51, 2.55, 2.60, 2.65, and 2.70 Tm (see Fig. 2.20). This shifted the mask image across the focal plane (see Fig. 2.19). If the reconstruction is correct the image will maintain its integrity at different values of $B\rho^{ref}$.

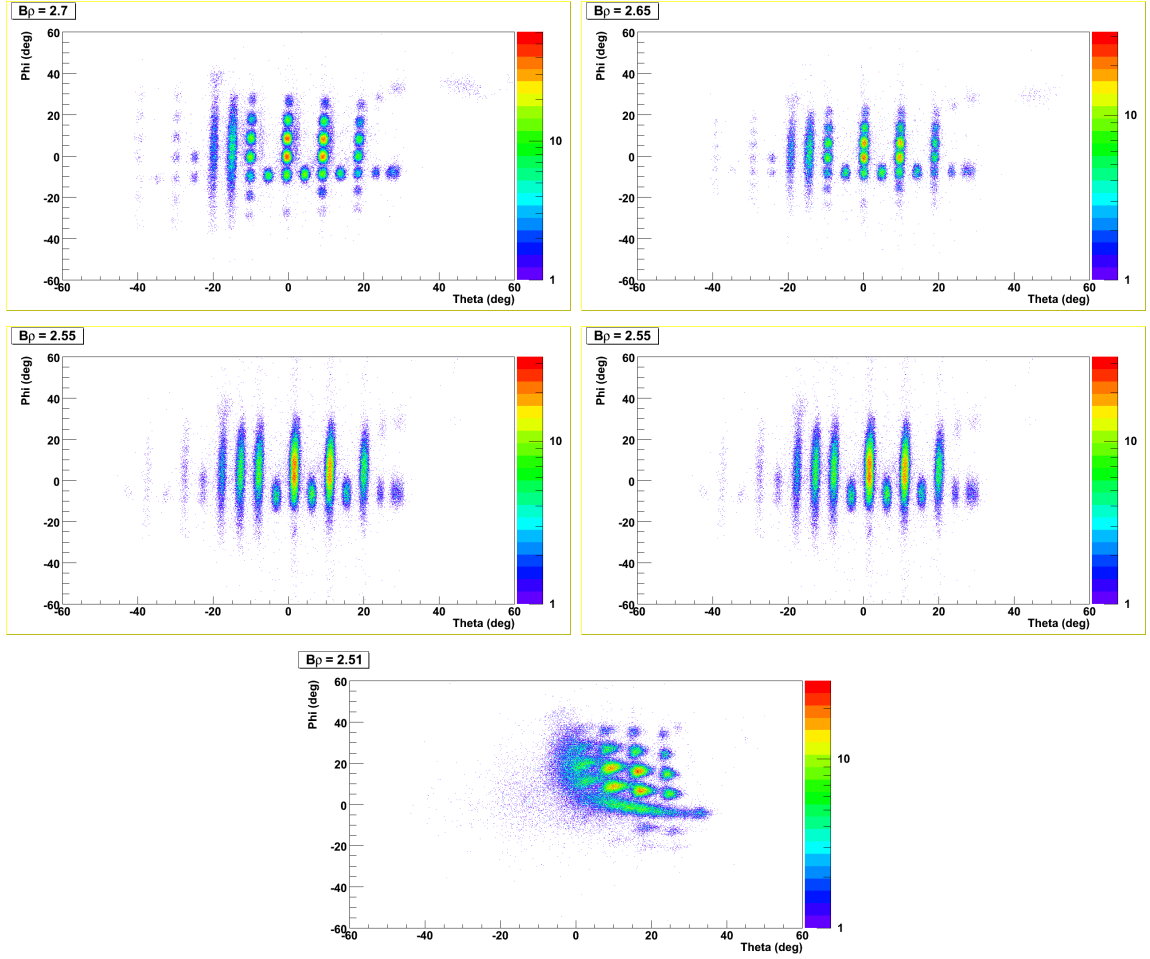


Figure 2.19: $B\rho^{ref}$ scan with mask.

As can be seen in Fig. 2.19, θ remains at a constant value across the focal plane, in accordance with Eq. 2.6. There is poorer resolution in Y , ϕ than in X , θ , which negates the use of transverse momentum distributions as analogous partners to their longitudinal counterparts. Also the SPEG resolution worsens towards the left-hand-side of the final focal plane. The data sets shown in 2.19 were used to measure the momentum acceptance and calibrate the dispersion of the beam. The dispersion relates the difference in momentum of different ions with their position on the SPEG

focal plane. It is the relation between the position in the SPEG focal plane (X_f) and momentum which allows the longitudinal momentum distribution (LMD) for each nuclide to be reconstructed. The momentum acceptance of SPEG is determined via Eq. 2.20.

$$\frac{\Delta p}{p} = \frac{X_{length}}{D} = \frac{60 \text{ cm}}{8.146 \text{ cm}/\%} = 7.37 \%. \quad (2.20)$$

Here X_{length} refers to the distance across the SPEG focal plane on the x -axis and D to the dispersion. The dispersion relates the distance between two points in X_f that correspond to a shift of one percent in momentum. The dispersion was taken as the gradient of Fig. 2.21. It relates to the transfer matrix (see Eqs. 2.5, 2.9) as the R_{16} term.

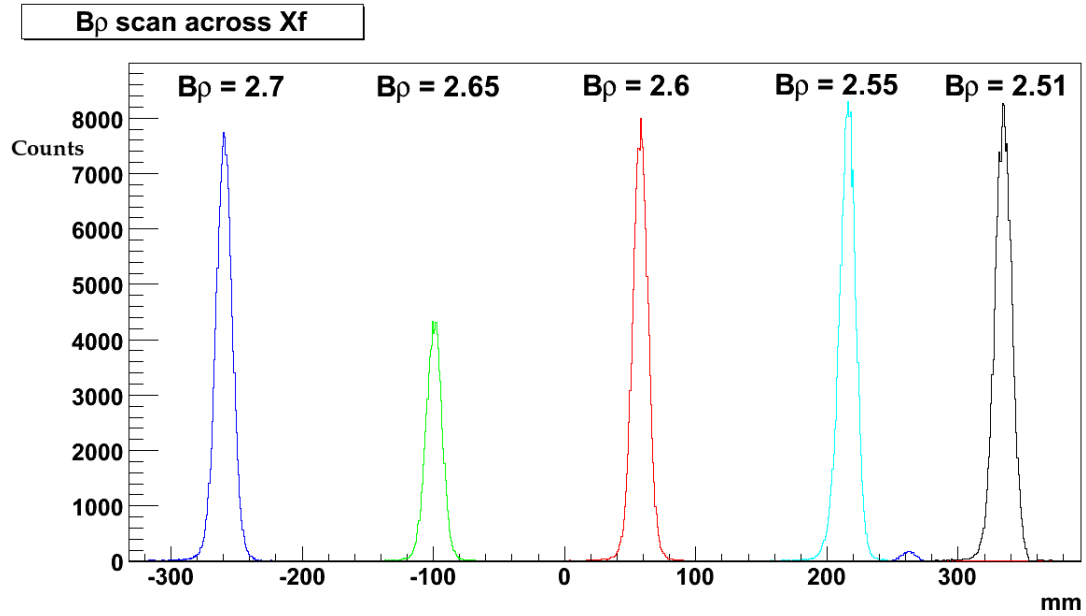


Figure 2.20: B_ρ scan across SPEG focal plane.

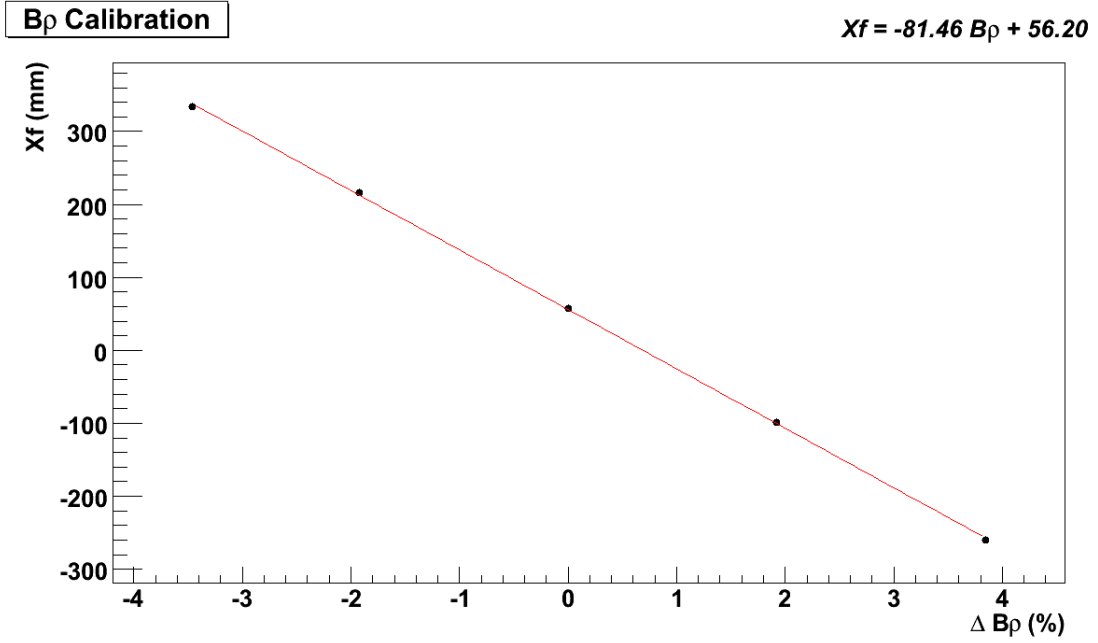


Figure 2.21: Dispersion calibration.

2.6 Drift Chambers

To measure the momentum distributions, precision position measurements are needed to reconstruct the particle's trajectory. This is achieved by use of two sets of gas-filled detectors, termed drift chambers. The drift chambers consisted of a set of two gas detectors, each with two rows of charge collection pads. As the charged particle passes through the drift chamber the gas is ionised, releasing electrons which follow the field lines of an applied electric field. The electric field strength is sufficient for swift transfer of the electrons via the most direct route available. The electrons are accelerated towards a positively charged $20\ \mu\text{m}$ proportional wire, which amplifies the electron number by a factor of $\sim 10^4$ [37]. The electron cloud is then collected by the

anode pads and gives information on the x -axis position of the passing ion. Each set of drift chambers has the length of 60 cm, height 12 cm, a length sufficient to span the SPEG focal plane. The sets consist of two rows of 128 anode pads, offset by half a pad in order to improve the position resolution by measuring the ratio of induced (or deposited) charge in the neighbouring pads. The method employed to fit the charge distribution is known as the Hyperbolic Inverse Secant Method, also known as SECHS [36]. The method fits the charge distribution over three pads, reconstructing the position of the ions to a better resolution than the width of an individual pad. The greater the distance between the ionisation point and the drift chamber pads where the charge is collected, the greater the time period between ionisation and collection. As the distance is positioned along the y -axis, time information can be related to the passing ions position in Y with knowledge of the geometry and electron drift velocity, V_D , taken as 50 mm/ μ s. In Fig. 2.22 is shown a schematic of the drift chambers. Each row of pads gives a separate measurement of the X and Y position of the passing ion at a position on the z -axis determined by the geometry of the detector. A linear least-squares fit is then used to reconstruct the trajectory of the ion, which is used to give a position value at the focal plane.

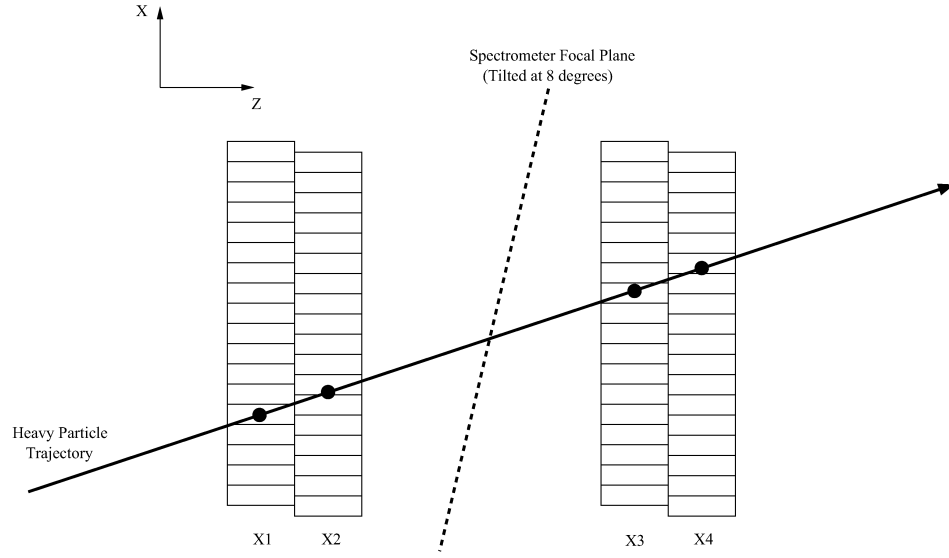


Figure 2.22: SPEG Drift Chambers.

In order to determine the position in Y of the passing ions the time taken between the initial ionisation and charge collection on the drift chamber pads must be measured. The plastic detector was taken as the start signal, the drift chambers used as the stop. This is possible as the time of flight of the ions between the drift chambers and the plastic scintillator is of the order of nanoseconds, which is negligible in comparison to the electrons drift velocity, taken as $5 \text{ cm } \mu\text{s}^{-1}$. To accurately convert this measured time to the position in Y , a time pulser with a period of 100 ns was employed. The subsequent calibration for the first drift chamber TDC (Time-to-Digital-Converter) is shown in Fig. 2.23.

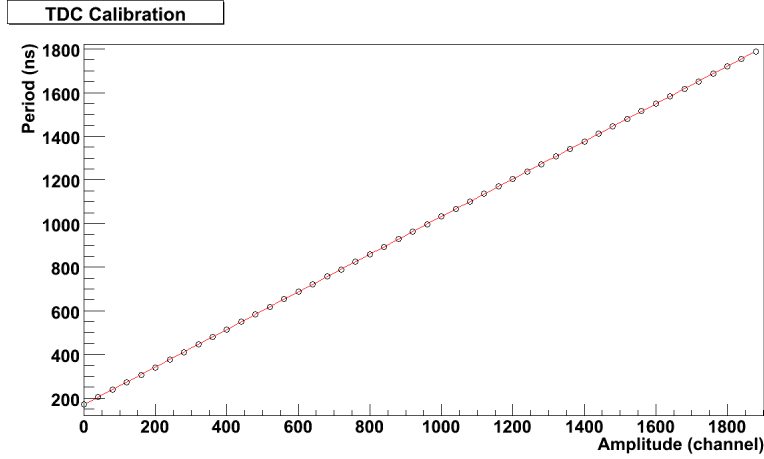


Figure 2.23: Drift chamber TDC calibration.

The drift chamber TDCs were used to calculate the passing ions position in Y , according to

$$Y = v_D \cdot cf \cdot td \cdot 0.01, \quad (2.21)$$

where Y is the position on the y -axis (mm), v_D is the drift velocity of the electrons ($\text{cm } \mu\text{s}^{-1}$), cf the TDC calibration factor (ns/channel) and td the channel number from the TDC. The drift chamber TDCs were found to have a calibration factor, cf , of approximately 3 ns per channel.

2.7 Ionisation Chamber

The ionisation chamber provides an energy loss measurement of the passing ions (according to the Bethe–Bloch formula, see Eq. 2.12) and is essential for particle identification. In order to keep a uniform energy loss measurement, the pressure of the Isobutane gas must be kept constant. Unfortunately, due to gas regulation issues

the pressure kept dropping and had to be increased several times throughout the experiment.

To correct for the fluctuating pressure an initial time-of-flight (TOF) correction was applied in order to align the energy loss of each isotope, as shown in Fig. 2.24.

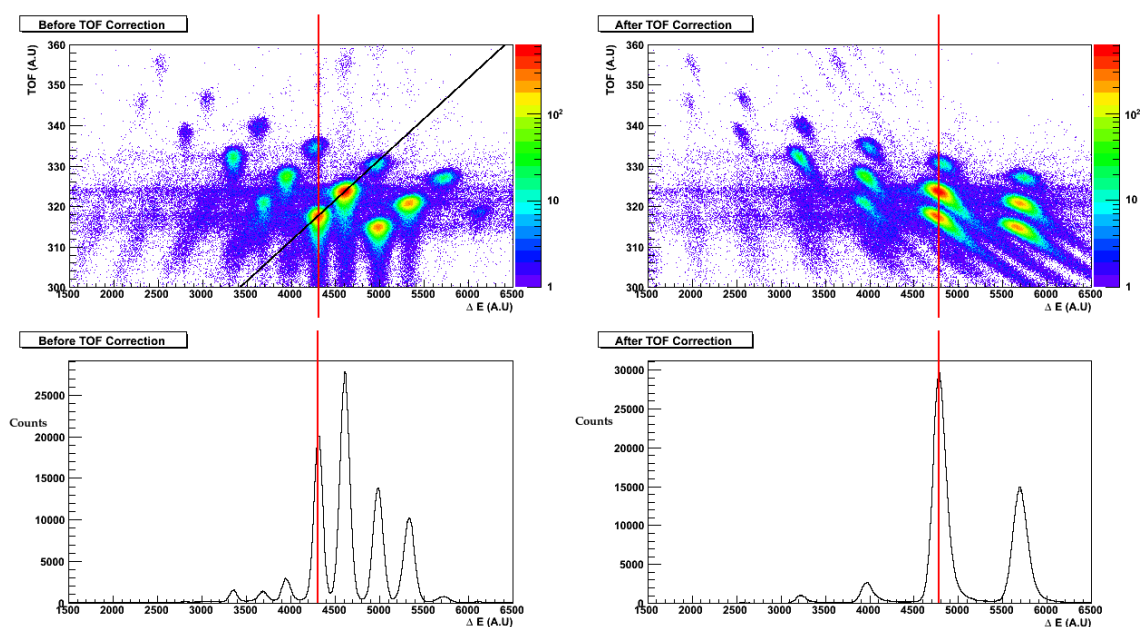


Figure 2.24: Ionisation chamber TOF correction.

The correction was done using the coordinates of the centre of each sodium isotopes position in $TOF : \Delta E$. A first order fit was then applied:

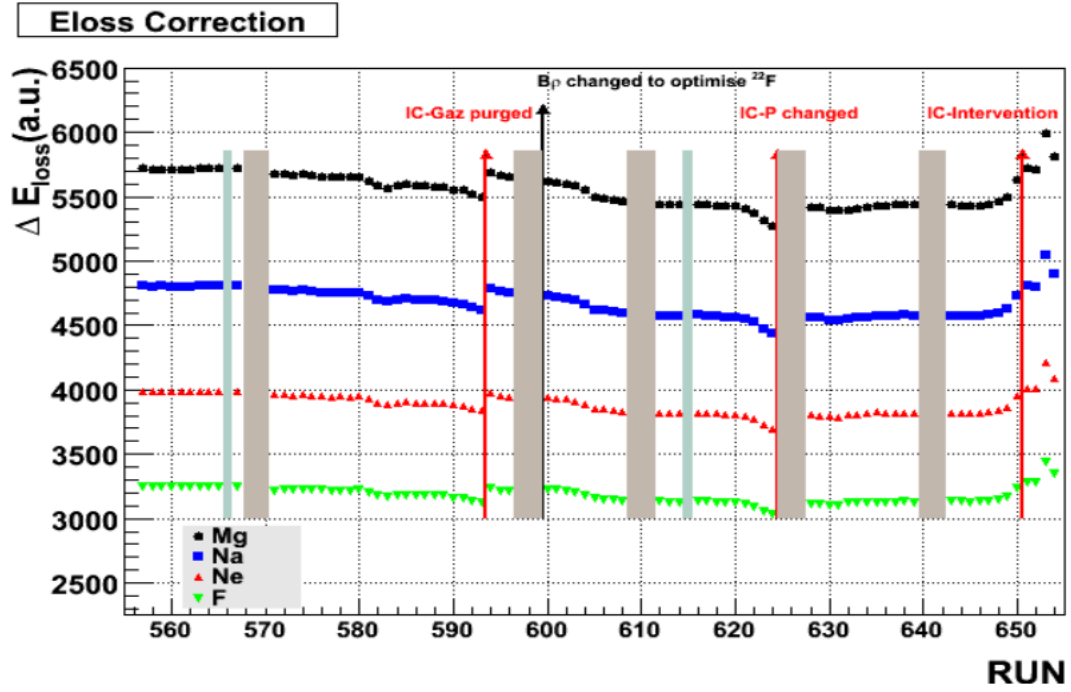
$$E'_{Na} = E_{Na} \cdot TOF + E_0. \quad (2.22)$$

Following the TOF correction being applied to all runs, the elements of the 1D projection of the energy loss (shown in the lower half of Fig. 2.24) may be fitted with

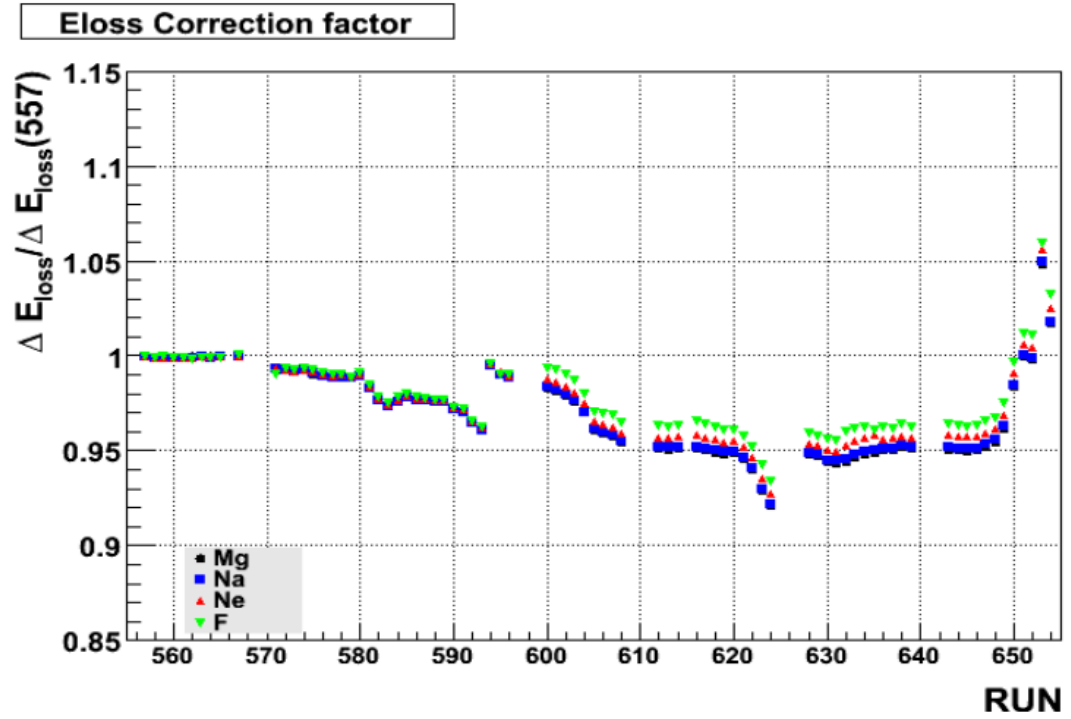
a Gaussian distribution in order to determine the mean energy loss for that element for that run. By taking the point of reference as the energy loss of the sodium isotopes in Run 557 (the first run) the shift in energy loss may be plotted for each element by run number (see Fig. 2.25(a)) and the correction factor for each element may also be plotted by run number (Fig. 2.25(b)). The variation of energy loss with pressure does not appear to have any significant dependence on Z until run 600, where there appears a slight dependence. This was taken as negligible and the runs were normalised by multiplication of the ΔE value by a corrective multiplication factor, $C_{\Delta E}$, defined by

$$C_{\Delta E} = \frac{\Delta E_{557}^{Na}}{E_i^{Na}}. \quad (2.23)$$

As the corrective factor is very similar for all measured elements $C_{\Delta E}$ was taken for the sodium isotopes, ΔE_{557}^{Na} being the energy loss for the TOF corrected Sodium isotopes in run 557 and E_i^{Na} being the energy loss for the TOF corrected Sodium isotopes in the i_{th} run. The improvement in resolution is necessary for the particle identification, demonstrated in the ΔE vs. E plots of the combined reaction data, shown in Fig. 2.26.

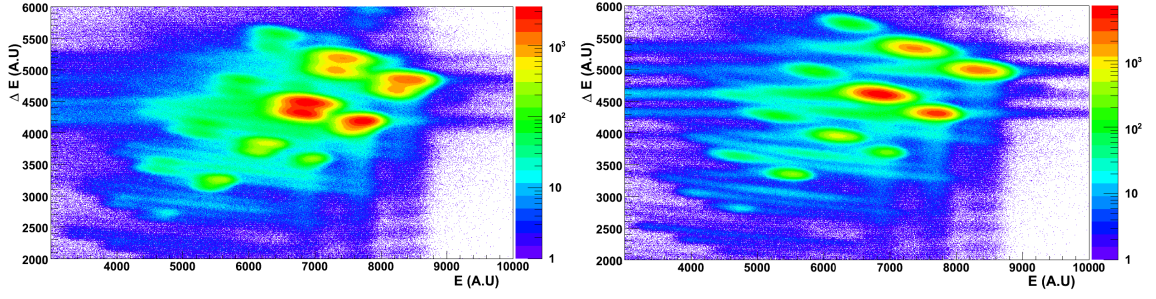


(a) Energy loss for Mg, Na, Ne and F against Run number.



(b) Correction factor for Mg, Na, Ne and F against Run number, defined in Eq. 2.23 for Na.

Figure 2.25: Ionisation gas pressure correction.



(a) Before gas pressure correction

(b) After gas pressure correction

Figure 2.26: Gas pressure correction effect.

2.8 Data Acquisition Trigger

The data acquisition was set to trigger on certain detectors, so as to only record data when a certain event was present, providing the processing gate was not already open (dead time). This was achieved using the GANIL Master Trigger (GMT), a logic unit into which the outputs from the seven chosen detector triggers were fed. There were seven triggers selected for use, shown in Table 2.2.

Table 2.2: Data Acquisition Trigger.

Trigger Number	Trigger
1	Ge OR
2	NaI OR
3	SPEG
4	SPEG + Ge OR
5	SPEG + NaI OR
6	Trifoil Div.
7	SPEG Div.

Trigger 1 relates to the logic output from the Germanium detectors. The signal begins as the output of one crystal's central contact (of 32 crystals) exceeds a preset threshold. This is converted to a digital pulse by the ADC (Analogue to Digital Converter), then passing into a Fan-In Fan-Out (FIFO) module, which makes the condition that if one of the 32 central contact pulses is above the threshold that a logic pulse is sent to the GMT to start the acquisition. Trigger 2 works in a similar manner, with the NaI detectors as the initial output. Trigger 3 refers to the plastic scintillator detector, where the beam particles are implanted at the end of the beam line. There was a photo-multiplier tube (PMT) attached to each end of the plastic detector, denoted 'EPL_L' and 'EPL_R' (left and right). The right signal was taken as the trigger, the signal delayed for proper time alignment with the other detector signals (as the plastic scintillator detectors process time was a few nanoseconds), then

This dec signal then prompts the GMT to open a Fast Analysis Gate (FAG) which determines whether the event is valid, to be passed on for further processing, or to be rejected. The opening of the FAG is simultaneous with that of the dead time gate opening, as the GMT is currently processing. On the condition that the event is accepted a validation gate is opened, with a validation point falling within the gates time duration as an addition measure to ensure the events validity.

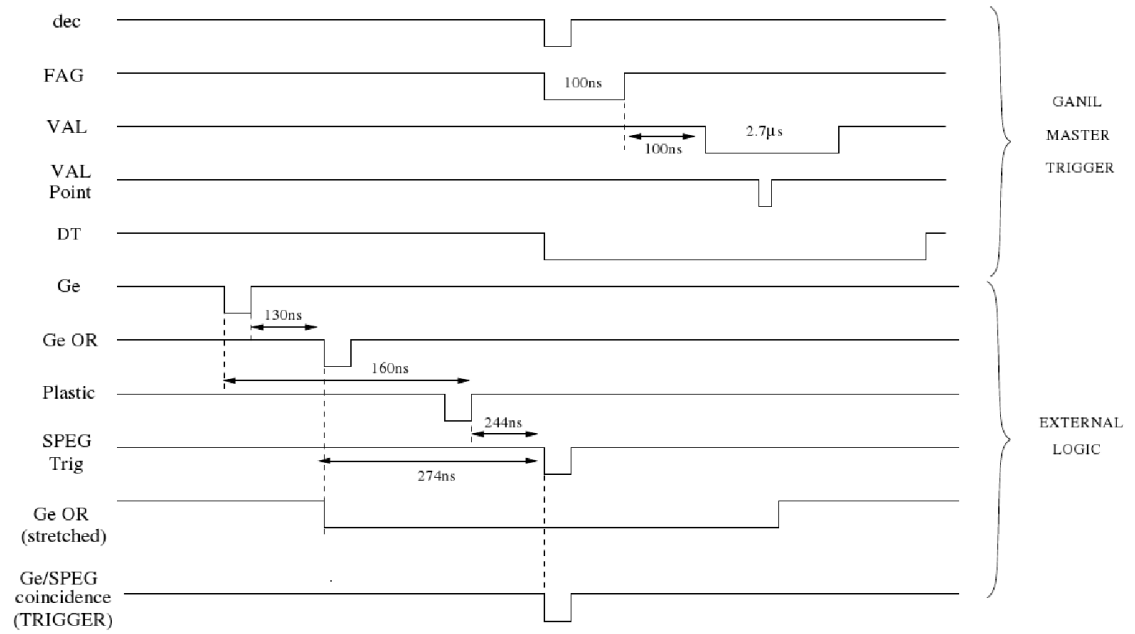


Figure 2.28: Representation of the timing signals used in the Ge OR and SPEG trigger.

Chapter 3

Analysis

In this chapter the techniques and procedure for both the experimental and theoretical analyses will be outlined. The main aims of the experimental analysis were the extraction of cross sections and momentum distributions for each reaction fragment, both inclusive and exclusive. Any exclusive measurement relies on the detection of the γ -ray transition associated with that state. This necessitates a careful reconstruction of the γ -ray spectra. A value which is relevant both to determining cross sections and the mean velocity of reaction fragments at the centre of the reaction target is the thickness of the reaction target.

3.1 Target Thickness

The target thickness was given as a nominal value of 183 mg cm^{-2} . In order to determine a more accurate value, the $B\rho$ value of several nuclides was measured from data taken with the secondary target removed and the direct beam centred on the

focal plane. These $B\rho$ values were compared with subsequent data where the target was set back in place. Using the LISE++ programme [19] the target thickness for a number of nuclides was calculated from their $B\rho$ values pre and post target. The mean of these values was then taken to give a value of $170.8 \pm 1.4 \text{ mg cm}^{-2}$. This value was subsequently used to determine the inclusive cross sections and also to adjust the velocity of the core fragments for the Doppler correction of the γ rays to account for energy loss in the target.

3.2 Doppler Shift and Broadening Correction

In order to account for the relativistic speeds of the core fragment nuclei as they emit γ rays, the Doppler correction equation

$$E_{\gamma}^{c.o.m} = E_{\gamma}^{lab} \frac{\sqrt{1 - \beta^2}}{1 - \beta \cos \theta}, \quad (3.1)$$

must be used. Here $E_{\gamma}^{c.o.m}$ is the photon's energy in the core fragment nucleus' centre-of-mass frame, and E_{γ}^{lab} is the energy observed in the laboratory frame. To calculate $E_{\gamma}^{c.o.m}$ the β ($= v/c$) value of the core fragment nucleus and the angle at which the γ ray was emitted with respect to the beam direction, θ , need to be used.

3.2.1 Lorentz factor calculation

A small distribution in energy of each core fragment nucleus causes a spread of Lorentz values. The Lorentz factor is defined by

$$\gamma = \frac{1}{\sqrt{1 - \beta^2}}. \quad (3.2)$$

Although this spread of values is small for each fragment, in order to correct the γ -ray spectrum for relativistic effects it is important to use the most accurate value of β possible. This can be done separately for each ion by using its position in the SPEG focal plane, via

$$\beta_{pt} = \sqrt{\frac{1}{((Z \cdot (c \cdot 10^{-6}) \cdot B\rho)/A)^2}}, \quad (3.3)$$

where β_{pt} is the β value for a given nuclide post-target, A is the nuclide mass, Z the nuclide charge, c the velocity of light in a vacuum (ms^{-1}) and $B\rho$ is the magnetic rigidity of that nuclide obtained from its position in the focal plane. The $B\rho$ in Eq. 3.3 is calculated as

$$B\rho = B\rho^{ref} \cdot (1 + X_f/D), \quad (3.4)$$

where $B\rho^{ref}$ is the nominal magnetic rigidity setting of SPEG, X_f is the position measurement in the horizontal direction across the focal plane and D is the dispersion, which is taken as 8.146%, the gradient of the $B\rho$ calibration shown in Fig. 2.21. The core fragments are taken as decaying in the centre of the target. Using the previously determined target thickness, the LISE++ programme [19] was used to calculate the energy loss for each nuclide. Three values were taken which corresponded to the minimum, mean and maximum β_{pt} for each nuclide and the beta values mid-target (before passing through half the target thickness, 85.4 mg cm^{-2} of ^{12}C). A second-order polynomial fit was applied, giving fit parameters unique to each nucleus. These parameters (par1, par0) were then applied event-by-event to give the β value at the middle of the target,

$$\beta_{mt} = \beta_{pt} \cdot par1 + par0. \quad (3.5)$$

An example of how β_{mt} changes for different values of β_{pt} is shown in Fig. 3.1 for ^{24}F .

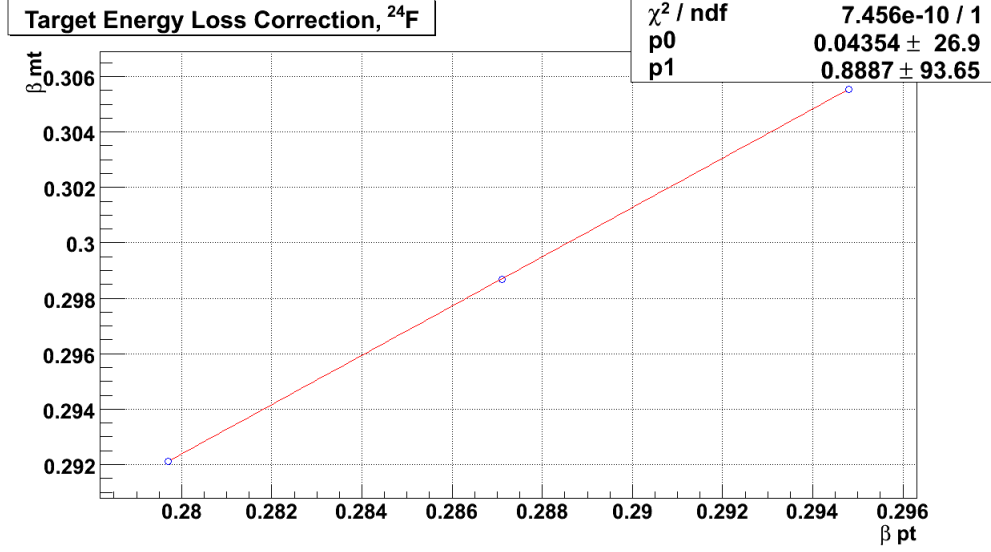


Figure 3.1: The effect of energy loss through half the ^{12}C target for ^{24}F . The β values are shown for post-target and mid-target.

Although the actual energy loss relationship is quite complicated, over a small range of β a linear fit is a good approximation, reflected by the small χ^2 value.

3.2.2 Theta Calculation

Theta is defined by the angle between the incident beam and the first interaction point of the γ ray, relative to the position where the γ ray was emitted. Each decay is assumed to be immediate and at the centre of the reaction target. Now that an event-by-event β has been calculated, values of θ must be found to use Eq. 3.1. For the NaI array the angle was taken by assuming a mean interaction depth of 30 mm

(from Monte Carlo simulations) and the geometrical positioning. The restrictions on Doppler-correction accuracy depend on the opening angle of the detector. For the EXOGAM array the electronic segmentation of the clovers coupled with their excellent intrinsic energy resolution enables a high quality Doppler corrected γ -energy spectrum. As the γ ray interacts with the clover and scatters through it, different fractions of the γ -ray energy are absorbed in a number of segments. The largest fraction is assumed to be the first interaction point and it is the angle from the centre of the secondary ^{12}C target and the centre of this segment and the incident beam which is taken as θ . Trigonometry is employed to calculate this angle for each segment, using the segment position values given by Fig. 3.2.

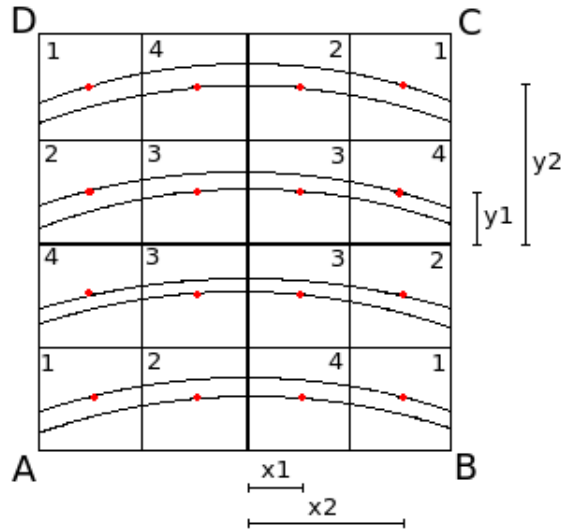


Figure 3.2: EXOGAM clover face. Taking the centre of the clover as $(0,0)$, the centre of each segment can be assigned a coordinate for $X (\pm x_1, x_2)$ and $Y (\pm y_1, y_2)$. These are used in Eqs. 3.6, 3.7.

The curved lines in Fig. 3.2 denote the theta cone, which coincides with the centre of the segments (marked in red). The clover face is shown with the beam directed into the page below it. The centre of each segment can be identified using a 2D coordinate system, with the clover centre taken as 0,0. For example, in Fig. 3.2 segment D1 would have the values $x = -x_2$, $y = y_2$. Using these coordinates the angle relative to the beam direction from the reaction target to the centre of each segment can be found via

$$\theta_f = \arccos \left(\frac{R - y}{\sqrt{2(R^2 + x^2 + y^2)}} \right), \quad (3.6)$$

$$\theta_b = \pi - \arccos \left(\frac{R - y}{\sqrt{2(R^2 + x^2 + y^2)}} \right). \quad (3.7)$$

Here θ_f refers to the forward EXOGAM array angles, θ_b refers to the backward array angles. The R value relates to the distance between the centre of the target and the centre of the clover, plus the mean interaction depth, taken as 30 mm (from Monte Carlo simulations).

Shown in Fig. 3.3 is the effect of Doppler-correction and add-back for the ^{24}F core fragment. The effect of the Lorentz boost can be seen in the top left (right) of the figure, where the non-Doppler-corrected photopeak energy is lower (higher) in energy for the backward (forward) angular positioned detector array. The add-back procedure was done on a single clover basis, with the central contact for each crystal summed for a clover non-Doppler-corrected energy, which was Doppler-corrected using Eq. 3.1, θ taken for the segment which recorded the highest energy in that clover for that event, assumed to be the first interaction point.

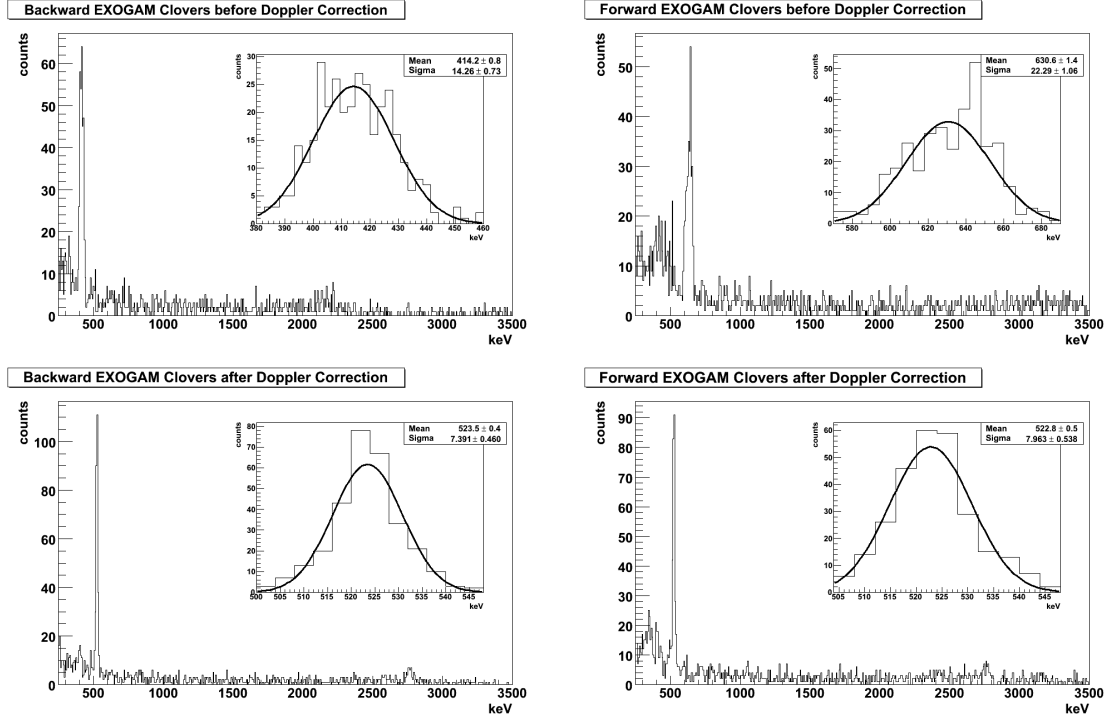


Figure 3.3: Shown top (bottom) are the ^{24}F γ spectra before (after) Doppler-correction and Add-back, left (right) is the backward (forward) EXOGAM array. The mean β for ^{24}F was ~ 0.30 . An insert of the ~ 523 keV photo-peak is shown for each case.

3.3 Inclusive Cross Sections

In order to derive the inclusive cross sections for one-neutron removal reactions a number of runs were taken without a secondary target in place throughout the experiment in order to measure the rate of the incident beam for each nuclide. The magnetic rigidity was set accordingly to centre the beam in the focal plane of SPEG. After particle identification was defined, as previously described, the beam rate was established relative to the scalers associated with a number of detectors. A scaler is an

electronic circuit that records the aggregate of a specific number of signals that occur too rapidly to be recorded individually, in this case scalers recorded the passage of ions through each little drift chamber (LDCX1..4), the TI and the Trifoil detector. The TI (Intensity Transformer) was used to monitor the current of the primary beam. In Fig. 3.4 the change in beam rate over consecutive data runs for four Fluorine isotopes (taken by dividing by the first LDC scaler, LDCX1) is shown. Both the beam intensity

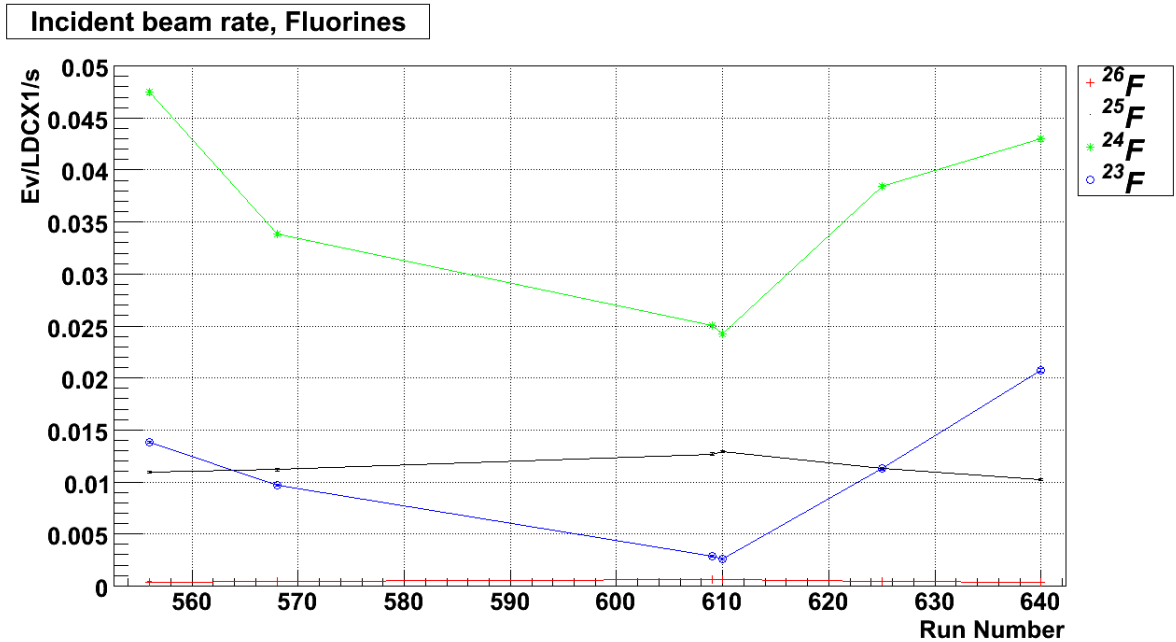


Figure 3.4: Incident beam rate determined using the LDCX1 scaler, shown here vs Run number for four Fluorine isotopes.

and composition were subject to fluctuation. To account for this, it was decided to scale the incident beam rate of each nuclide to the fragment rate of neighbouring reaction runs. For example the rate of the direct beam ^{25}F would be scaled to the rate

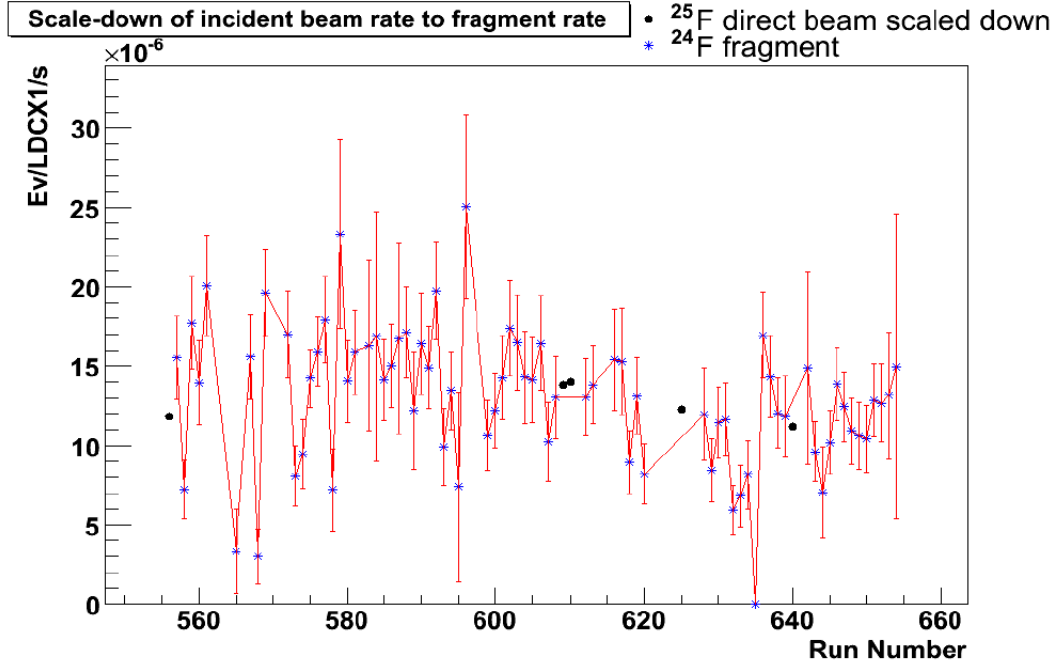


Figure 3.5: Scaledown of ^{25}F incident beam rate to ^{24}F fragment rate.

of the core fragment ^{24}F , shown in Fig. 3.5. Due to some irregularities with the Trifoil trigger, the incident beam runs taken were those using only the SPEG trigger. These 5 runs were scaled to their neighbouring reaction run fragments, a zero-suppressed χ^2 fit was employed to find the optimum scaledown factor. The χ^2 fits for scaledown factors of the ^{25}F direct beam rate to the ^{24}F reaction product rate are shown in Figs. 3.6, 3.7. The three lines refer to three respective fits. The black line an average fit, the red line a χ^2 fit including the errors on the reaction product rates, the blue line a χ^2 fit including both the errors on the reaction product rates and the errors on the beam rate. The last fit was taken to calculate the inclusive cross sections. Due to the possibility of large beam rate fluctuations over a small time scale an average of a small number of reaction run's rate was taken. Both one, two and three neighbouring runs

were taken either side of the direct beam run rate (where possible). It was decided that taking a single neighbouring run was the most accurate method. Figs. 3.6, 3.7 take a single neighbouring run.

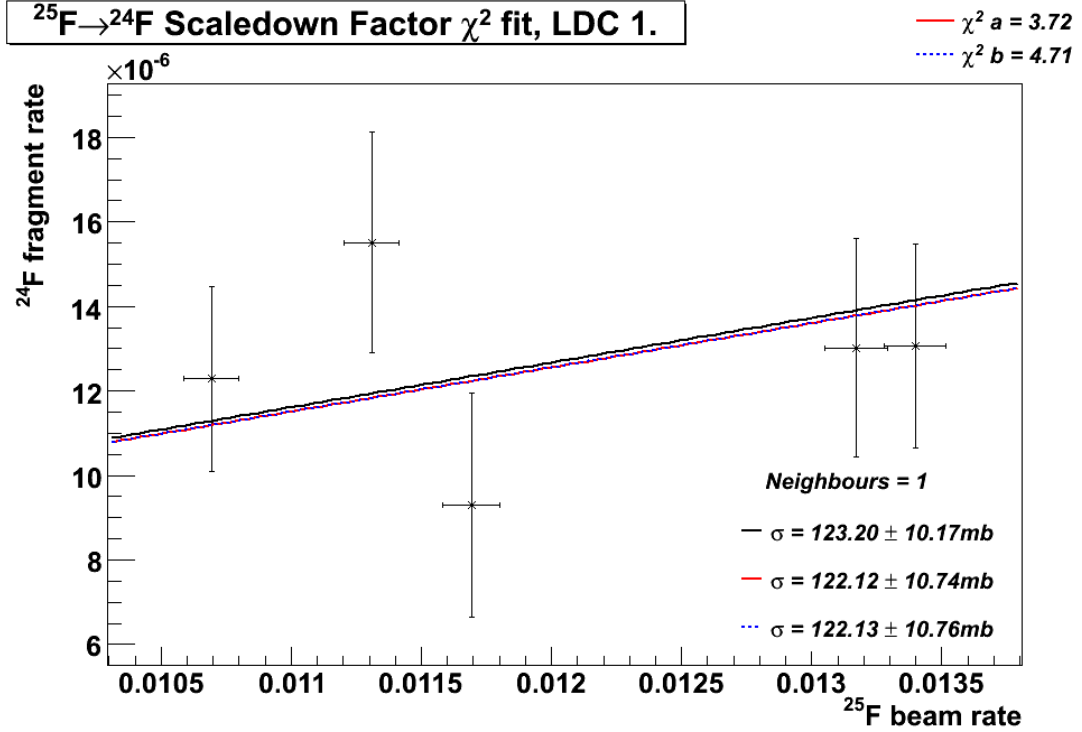


Figure 3.6: ^{24}F Scaledown factors from LDCX1 (see text).

A χ^2 fit of the scaledown factors, as described above, was used to determine the inclusive cross section (shown in Figs. 3.6, 3.7), as shown in Eq. 3.8,

$$\sigma_{inc} = \frac{N_{cf}}{N_{beam}} \frac{1}{nx}. \quad (3.8)$$

Here N_{cf} refers to the number of core fragment nuclei produced by one-neutron removal reactions, N_{beam} is the number of incident nuclei, n the target density and x

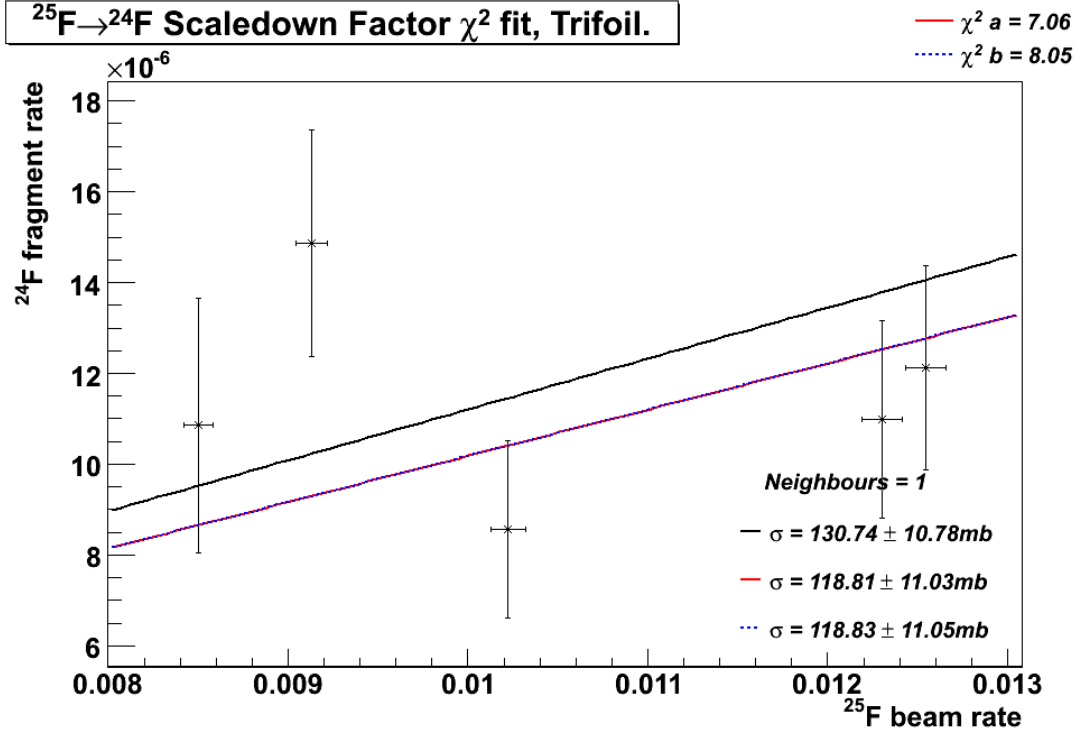


Figure 3.7: ^{24}F Scaledown factors from Trifoil (see text).

the target thickness. The ratio N_{cf} to N_{beam} is taken as the scaledown factor from the χ^2 fit described above. The final inclusive cross sections were the weighted mean of five inclusive cross section values for each nuclide, calculated separately for four LDC and one Trifoil scaler values. For the nuclides with the lowest production rate the majority of the 2 – 3 hour long runs had no counts for the reaction product. This was the case for $^{26}\text{F} \rightarrow ^{25}\text{F}$ and $^{24}\text{O} \rightarrow ^{23}\text{O}$. In these cases a number of runs was combined to enable a value of core fragment rate to be used for the scaling. Using reaction run data of a greater time duration away from the normalisation run data introduced greater uncertainty, reflected in the error on the cross section.

3.4 Exclusive Cross Sections

For the exclusive cross sections the branching ratio to the state considered must be determined, after which the exclusive cross sections may be determined via

$$\sigma_i = b_i \sigma_{inc}, \quad (3.9)$$

where σ_i is the exclusive cross section and b_i is the branching ratio to the i_{th} state.

To find b_i , peaks in the Doppler corrected γ spectra must firstly be identified. After background subtraction, the peaks were fitted with a Gaussian and the integral of the peaks extracted. This was done independently for the forward and backward EXOGAM arrays and the NaI array. For the EXOGAM analysis, the Doppler corrected photopeak was gated to give the non-Doppler-corrected (NDC) energy. The mean of this NDC energy was then found using a Gaussian fit. A factor which must be accounted for is the effect of the Lorentz boost at these relativistic beam energies. This will have the effect of forward-focusing the γ rays so that the efficiency calibrations done with stationary, isotropic sources will not be applicable. To correct for this, Geant4 [1] simulations of the EXOGAM setup were employed. The number of simulated γ ray events passing through the forward (backward) array when the source was stationary was N_f (N_b). Multiple simulations using the same number of initial events were then ran for a number of different β values. The number of events passing through the forward (backward) array when $\beta > 0$ was recorded, n_f (n_b). A value termed *ratio* was determined as a function of β for the forward (backward) array by N_f/n_f (N_B/n_b). The plots of *ratio* vs. β for the forward and backward arrays can be seen in Figs. 3.8 and 3.9 respectively.

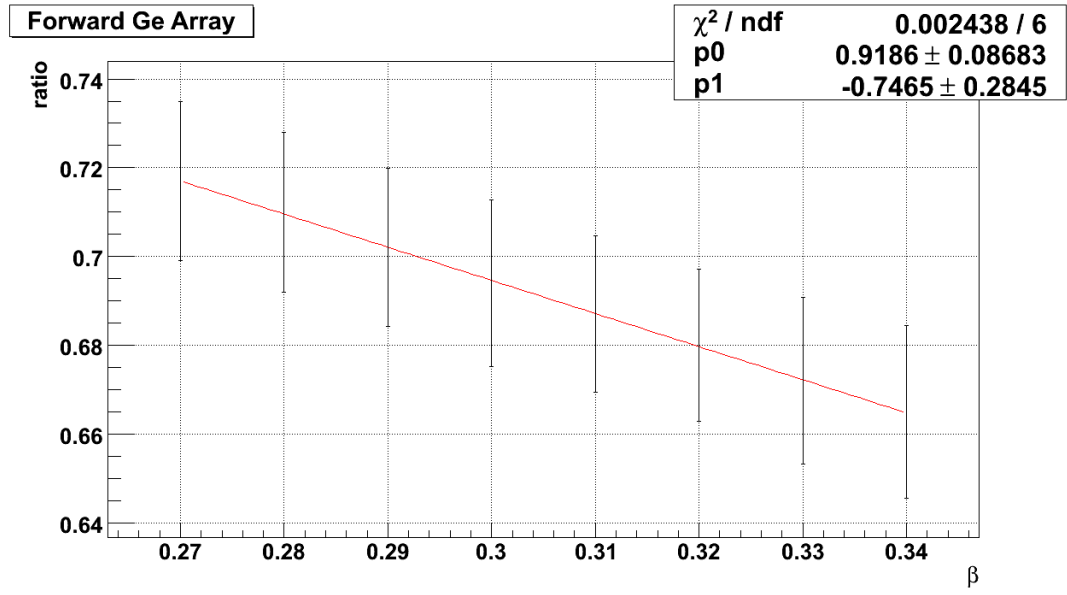


Figure 3.8: Forward EXOGAM Array Ratio (see text).

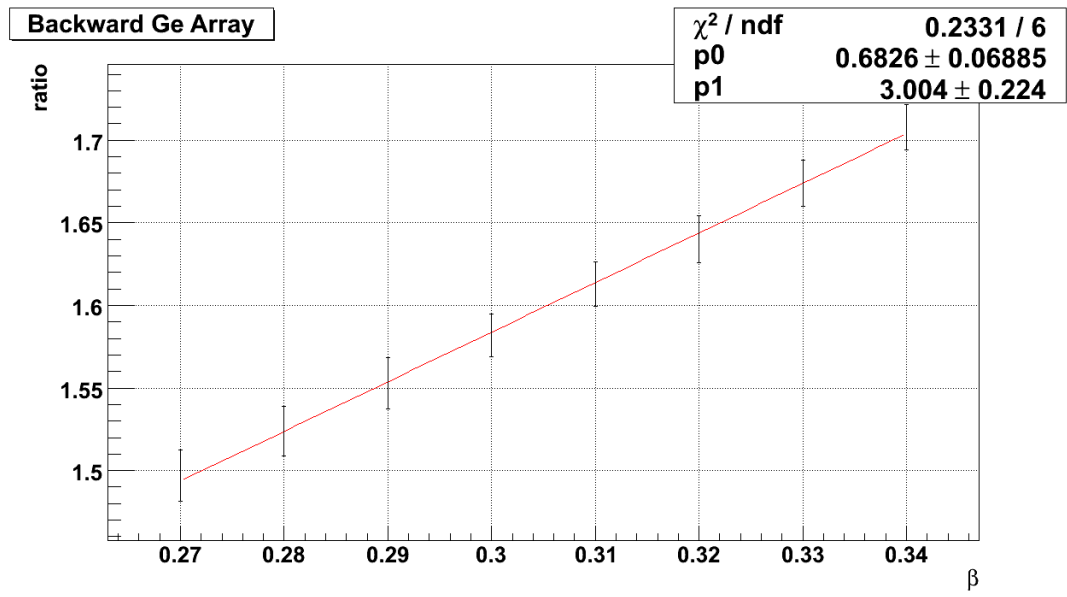


Figure 3.9: Backward EXOGAM Array Ratio (see text).

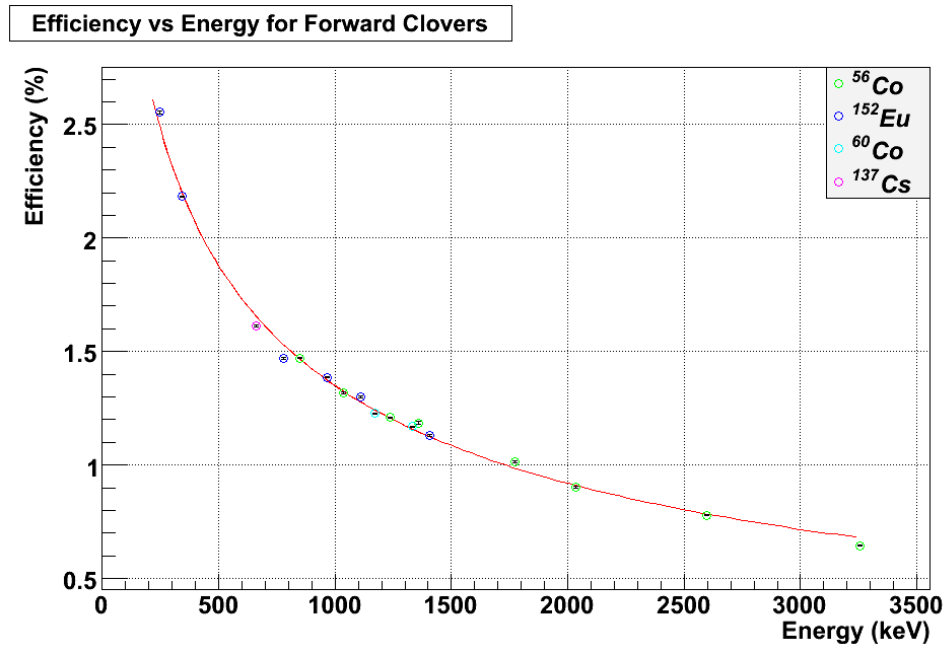


Figure 3.10: Isotropic Forward EXOGAM Array Efficiency.

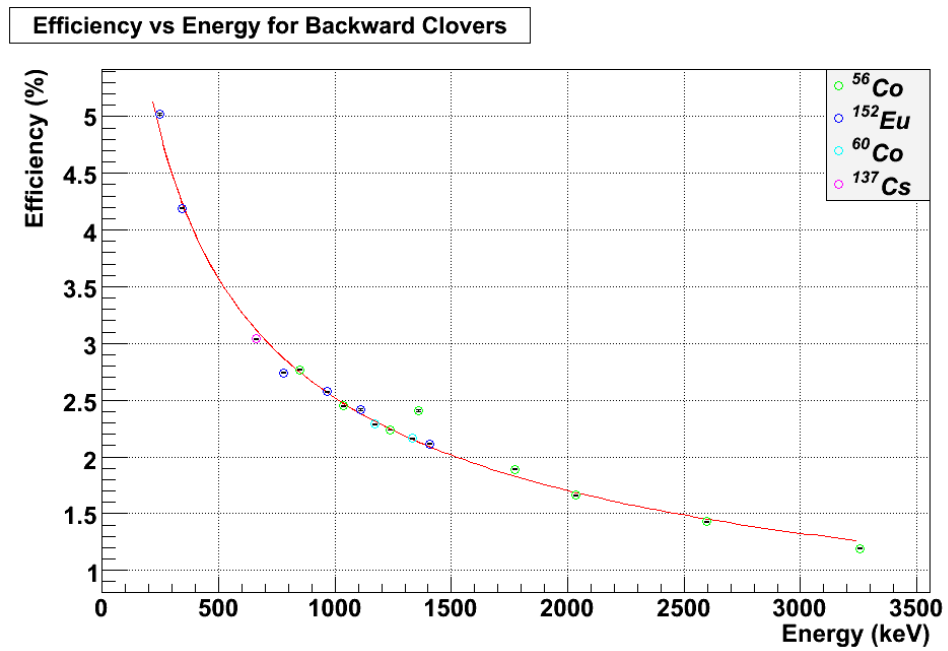


Figure 3.11: Isotropic Backward EXOGAM Array Efficiency.

A linear fit was taken for Figs. 3.8 and 3.9, which was used to correct the efficiency calibration taken using stationary sources for the effect of the Lorentz boost, done separately for the forward and backward EXOGAM arrays. This is done using

$$\epsilon_\beta = ratio \cdot \epsilon_0 = (p1 \cdot \beta + p0) \cdot \epsilon_0, \quad (3.10)$$

where β is the Gaussian mean of the event-by-event calculated β for that nuclide (e.g. β_{mt} in Eq. 3.5). The parameters $p1$, $p0$ are obtained from the linear fits for the forward and backward arrays. The efficiency for the NDC (non-Doppler-corrected) energy, ϵ_0 , is calculated via Eq. 2.14), the efficiency fits shown in Figs. 3.10 and 3.11 are for the forward and backward arrays respectively. The efficiency, ϵ_β , is then used to determine the total number of γ rays emitted at that decay energy (n_γ) in each array. The intensity of each γ ray is found as

$$I_\gamma = \frac{\frac{100}{\epsilon_\beta} \cdot n_\gamma}{N_\gamma}. \quad (3.11)$$

N_γ is found by using a trigger condition that includes trigger 7 (see Table 2.2) and taking the total number of core fragment events. As trigger 7 was divided by 30 and triggers 4 and 5 were divided by 1 this total number was multiplied by 30 to give N_γ . The above process is completed separately for the forward and backward EXOGAM array and the NaI array (for γ peaks where resolution in the NaI is possible). These 3 (2 if NaI not possible) I_γ values are used with a weighted mean to yield a final I_γ value. After each I_γ has been calculated the state feeding must be accounted for in order to calculate the branching ratio for each state, b_i . In cases where the level scheme is known to a good extent, previous work can be applied. In lesser known cases a combination of intensity balancing and $\gamma\gamma$ coincidences can be employed. A simple

example of feeding subtraction can be where two decays (γ_2, γ_3) feed into the state E_1 , which decays via a single transition, γ_1 . The branching ratio to E_1 is calculated from the intensity, I , of the transitions via

$$b_1 = I_1 - I_2 - I_3. \quad (3.12)$$

Once the branching ratio has been determined for a given state the exclusive cross section, σ_{ex} , can be determined via

$$\sigma_{ex} = b_i \sigma_{inc}, \quad (3.13)$$

where σ_{inc} is the inclusive cross section, determined by Eq. 3.8.

3.5 Inclusive Momentum Distributions

The drift chambers in the focal plane of SPEG were used to determine the event-by-event x -axis position on the SPEG focal plane. The $B\rho$ of each nuclide could then be calculated via Eq. 3.4. This is then related to the nuclide's momentum via

$$P_z = B\rho \cdot Z \cdot c \cdot 10^{-6}, \quad (3.14)$$

where Z is the charge of the (fully stripped) ions and c is the velocity of light in a vacuum (ms^{-1}). Due to limited statistics it was necessary to optimise for the detection of γ rays. To this aim, triggers 4, 5, 6 and 7 were used for the reaction runs (see Table 2.2). Due to problems with the Trifoil trigger it was discounted. In order not to bias the inclusive momentum distribution, a trigger condition was set to only accept events which included trigger 7, except in the case of $^{24}\text{O} \rightarrow ^{23}\text{O}$ where there were no

excited states [64] and the events from triggers 4 and 5 were included as coinciding with background γ radiation did not discount the validity of the events as part of the inclusive momentum distribution.

3.6 Exclusive Momentum Distributions

The first step in determining the exclusive momentum distribution for each excited state in the core fragment was to gate on the energy region of the photopeak. The energy limits were determined by fitting a Gaussian function to the peak following background subtraction, then taking the energy limit values to be 3σ each side of the given mean. When the energy limits have been determined the number of events falling within these limits in the non background subtracted spectra is determined (a). The background is then fitted and subtracted. This gives another number of events, n , the difference between the two being the number of background events within the energy limits, $b = a - n$. This is illustrated in Fig. 3.12.

The value for BE_{min} on Fig. 3.12 was chosen a few keV higher than E_{max} in order to ensure no E_γ events were within the background region. Then BE_{max} was chosen in order that the number of events in the background region was equal to the number of background events (i.e. events underneath the background fit) in the peak region. The background region was taken as a higher energy than the peak region, so as not to include the Compton edge from the observed transition. Along the same lines, care was taken so the background region was not contaminated by the Compton edge of a possible transition directly above it. Now the values for E_{min} , E_{max} , BE_{min}

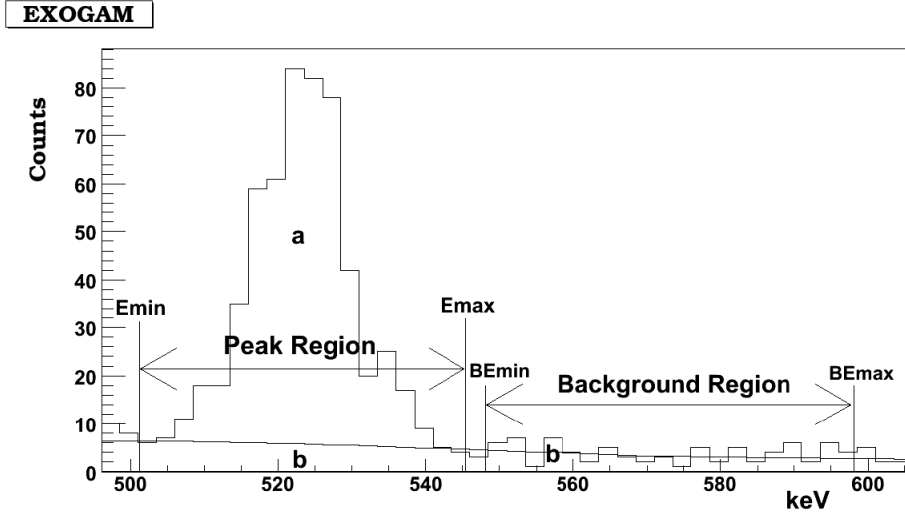


Figure 3.12: Background Subtraction schematic (see text).

and BE_{max} have been established, the background subtraction for the LMDs may be performed. The peak region and the background region are gated upon to produce a peak LMD and a background LMD. The background LMD is then subtracted from the peak LMD to remove the background contribution. Where peak resolution in the NaI array was possible, the events were combined with the EXOGAM events for that transition to increase statistics. In Fig. 3.13 is an example of this background subtraction. The top row is for the EXOGAM gated LMDs. At the left of that row is the $E_{min} - E_{max}$ gated LMD, the middle figure is for the $BE_{min} - BE_{max}$ gated LMD and on the right is the LMD following subtraction. The middle row is the same, but for the NaI array. The bottom row of Fig. 3.13 shows the addition of the EXOGAM gated LMD to the NaI gated LMD. For most cases only the EXOGAM gated LMD was used due to poor energy resolution and high background for the NaI array.

Now the transition LMDs have been background subtracted, yielding P_t , we have

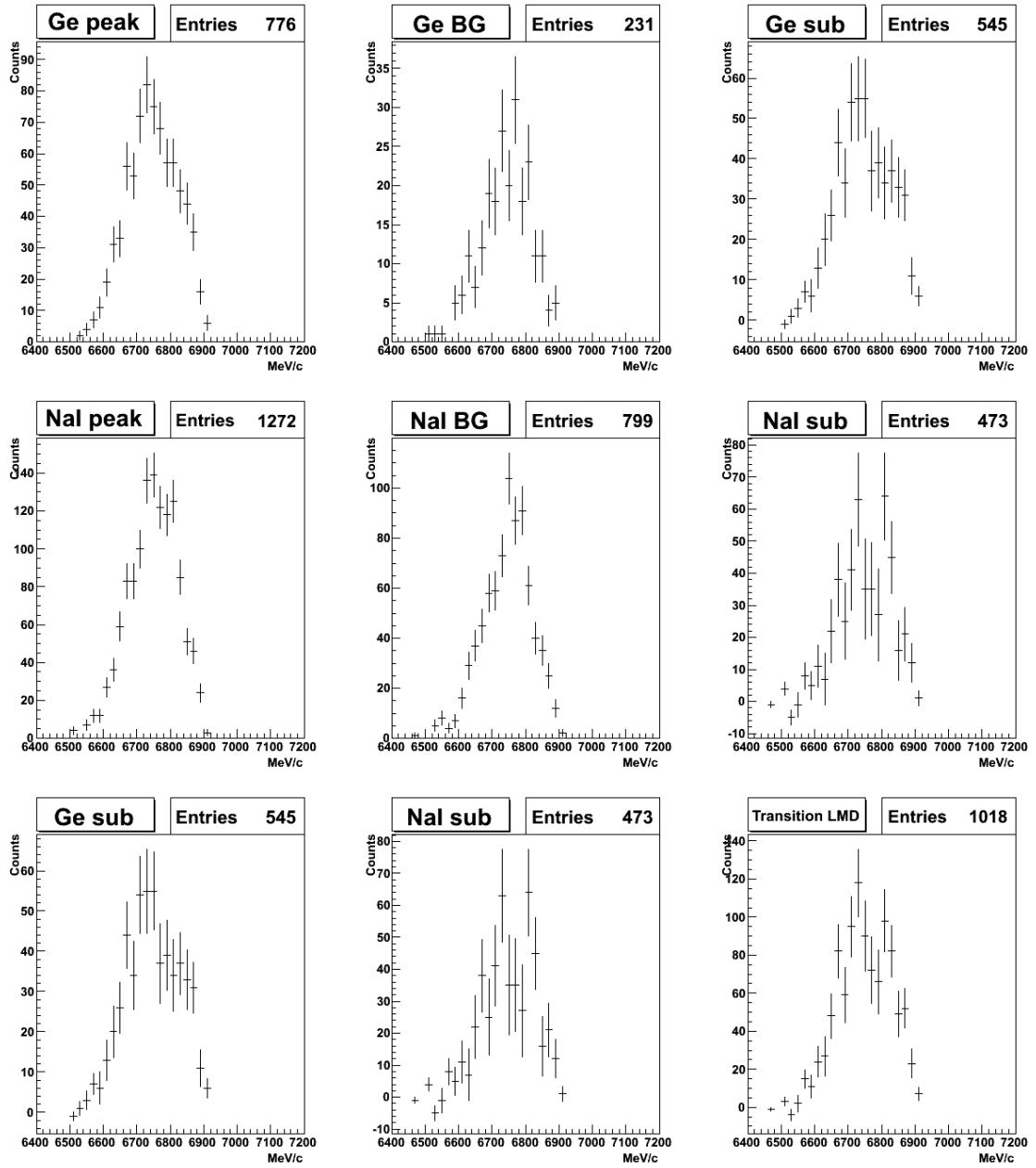


Figure 3.13: Example of LMD background subtraction, taken for the 916 keV transition from ^{23}F (see text).

to account for the feeding in order to have LMDs specific to each excited state, P_s . For some cases the level scheme is partially known, for others a combination of intensity balancing and $\gamma\gamma$ coincidences must be employed. With the intensity of each transition calculated via Eq. 3.11 and the feeding known, the LMD for each state can be determined. In the example below γ_2 feeds into state 1, which decays via a single transition, γ_1 . The transition LMDs for γ_1 (P_{t1}) and γ_2 (P_{t2}), have been previously calculated. The LMD for state 1, P_{s1} , can be found via

$$P_{s1} = P_{t1} - \frac{I_2 N_1}{I_1 N_2} P_{t2}, \quad (3.15)$$

where N_i is the number of counts in P_{ti} and I_i is the intensity of γ_i . The ground state distribution, P_{gs} was then determined by subtracting the LMDs for each excited state from the inclusive LMD, via

$$P_{gs} = P_{inc} - \sum_i \frac{N_{inc} b_i}{100 N_i} P_{si}, \quad (3.16)$$

where b_i is the percentage branching ratio to excited state i , N_{inc} (N_i) is the number of counts in the inclusive (excited state) LMD, P_{inc} (P_{si}).

3.7 Eikonal Calculations

3.7.1 Exclusive Cross Sections

Theoretical values for the cross sections to each state of the core fragment are the product of the occupancy of that subshell and the mechanism of the single-neutron removal reaction. Shell-model calculations may be used to give spectroscopic factors

that predict orbital occupancies for each state. An eikonal code (J.Tostevin [74]) may be used to give the partial production (single particle) cross section for that orbital at the energy of the state (see Fig. 3.15(b)), providing information on the reaction mechanism. The theoretical exclusive cross sections to each state may then be calculated using

$$\sigma_{state}(I^\pi) = \sum_i \left(\frac{A}{A-1} \right)^N C^2 S_i \cdot \sigma_{sp_i}, \quad (3.17)$$

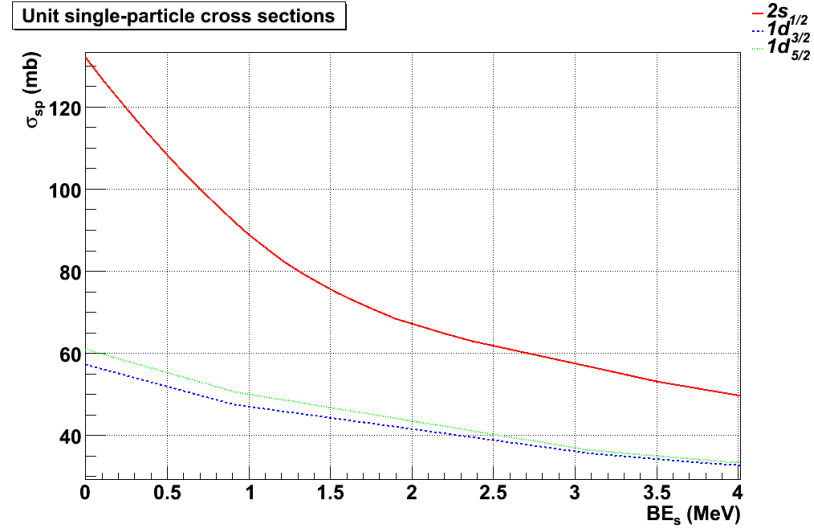
where i is the orbital ($1d_{3/2}$, $2s_{1/2}$ and $1d_{5/2}$ considered), $C^2 S$ is the spectroscopic factor given by shell-model calculations and σ_{sp} is the (unit) single-particle cross section for the considered state's energy. A centre-of-mass correction is also applied [20], to account for the change in mass after one nucleon is removed, N being the harmonic oscillator shell number, A the projectile mass number. For the $1d_{3/2}$, $2s_{1/2}$ and $1d_{5/2}$ subshells, $N = 2$. By convention, the theoretical $C^2 S$ values presented are from the USD interaction in the sd model space in pn formalism [15] (unless otherwise stated). The sum of the exclusive cross sections to all bound states gives the theoretical inclusive cross section, $\sigma_{theo.}$.

The energy of a given state was needed in order to correctly calculate the corresponding single-particle cross section. The energy of the fragment's excited state, E_s , was related to the effective binding energy via

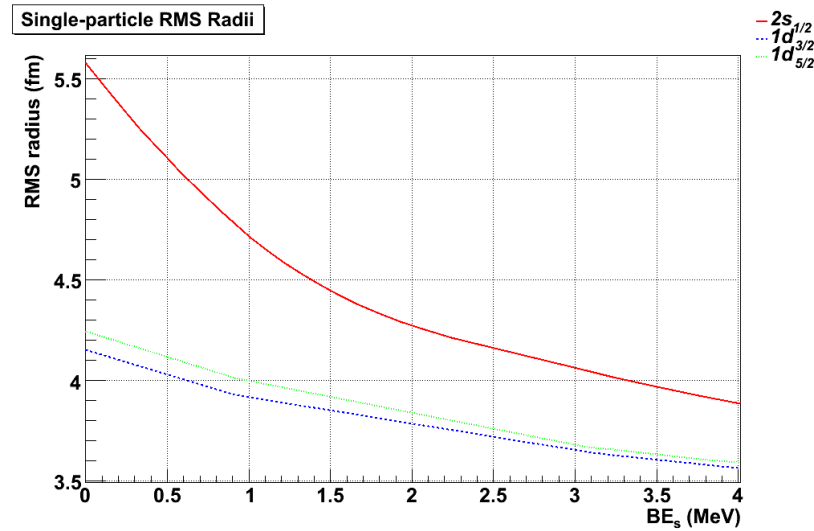
$$BE_s = BE_{gs} + E_s, \quad (3.18)$$

where BE_s is the effective binding energy of the given state, BE_{gs} being the binding energy for the ground state for the projectile. The effective binding energy was an input for both shell-model calculations [15] and the eikonal code [74], having a direct

impact on the Hartree–Fock calculated RMS radius of the nuclide in that given state. This in turn had a significant contribution to the single–particle cross sections as can be seen in Fig. 3.14 for each subshell, the values taken for the case of $^{26}\text{F} \rightarrow ^{25}\text{F}$.



(a) Single–particle Hartree–Fock RMS radii



(b) Single–particle cross section

Figure 3.14: Dependence of σ_{sp} on RMS radius.

Shown in Fig. 3.15 are the single-particle cross sections for $^{26}\text{F} \rightarrow ^{25}\text{F}$ as a function of BE_s , shown separately for the $2s_{1/2}$ and $1d_{5/2}$ subshells. The contributions from stripping and diffraction mechanisms are also displayed.

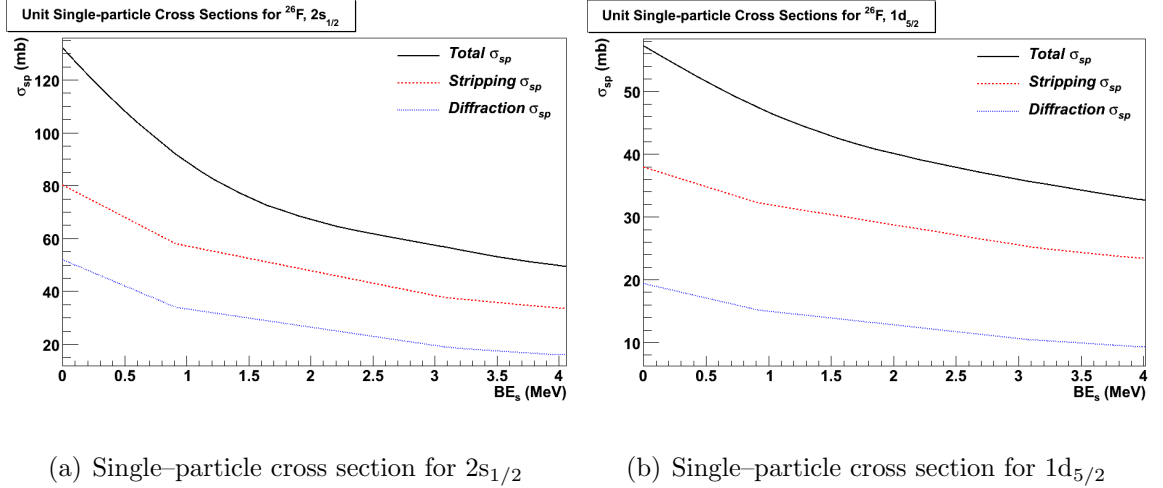


Figure 3.15: Contributions of stripping (nucleon absorbed) and diffraction (nucleon dissociated) mechanisms to the single-particle cross section.

Stripping refers to the case where the removed nucleon reacts with the target and excites it from its ground state. Diffraction describes the dissociation of the nucleon from the residue through their two-body interactions with the target, each being at most elastically scattered. As shown in Fig. 3.15, stripping is the dominant nucleon removal mechanism. This is usually the case, the exception being that of halo systems. The inclusive theoretical cross sections shown in Table 4.1 were calculated by the summation of the exclusive cross sections of all bound states predicted by shell-model calculations employing the USD interaction, taking the mean beam energy in the centre of the target for the nuclide considered.

3.7.2 Experimental Spectroscopic factors

There are certain difficulties facing the extraction of experimental C^2S values. In order to determine these values, the experimental exclusive cross sections must be divided by the single-particle cross sections determined using eikonal theory [74]. The single-particle cross sections are quite different for the $2s_{1/2}$ subshell and the $1d$ subshells (see Fig. 3.15(b)), which necessitates knowledge of the contribution of the individual orbital occupancy of that state prior to the extraction of experimental C^2S values. This occupancy could be determined for cases where the exclusive LMDs had high statistics, or in cases where the state is restricted to one orbital from angular momentum coupling. It is the exclusive state LMDs which may be compared to theoretical eikonal theory LMDs in order to infer information on the subshell occupancy of the given state.

3.7.3 Exclusive Momentum Distributions

In order to give information on the subshell occupancy the exclusive LMDs can be compared with the theoretical LMDs for each orbital. The eikonal code written by J.Tostevin [74] was used to produce theoretical LMDs specific to each state for the $1d_{5/2}$, $2s_{1/2}$ and $1d_{3/2}$ subshells. Only the aforementioned subshells were considered due to the nuclear region. The theoretical LMDs were determined by using the Michigan State University version of the shell-model code OXBASH [15] to calculate the Hartree-Fock RMS radius using the SKX Skyrme interaction [2], which in turn was used to calculate the density distribution of the wavefunction for the given state. The eikonal code [74] was then used to calculate the S-matrices of the core fragment

and valence neutron, this being combined with the wavefunction to give the theoretical LMDs for each considered orbital. The binding energy taken for a given state had a slight effect on the theoretical LMDs, the distribution broadening slightly, proportional to an increase in BE_s (see Eq. 3.18). The eikonal momentum distribution is the sum of the distribution of the magnetic substates that comprise that subshell. In the case of the $2s_{1/2}$ subshell with $l = 0$ there is only one magnetic substate, $m_l = 0$. For the $1d_{3/2}$ and $1d_{5/2}$ subshells with $l = 2$, $m_l = 0, 1, 2$. Shown in Fig. 3.16 is the eikonal distribution calculated for the $1d_{5/2}$ subshell of the ^{24}F fragment in the ground state, accompanied by its composite magnetic substate distributions.

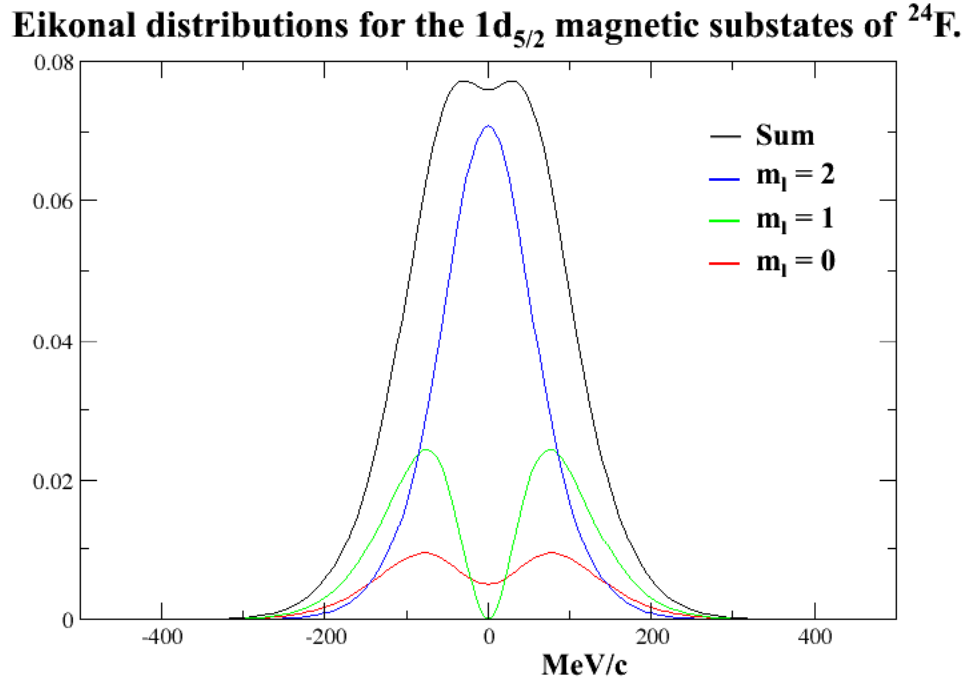


Figure 3.16: Eikonal distribution for the ^{24}F $1d_{5/2}$ ground state, showing the contribution from the magnetic substates.

3.7.3.1 Transformation of Theoretical LMDs

The eikonal code theoretical distributions are in the centre-of-mass (c.o.m.) frame [74]. As the measured LMDs were taken from nuclei moving at relativistic speeds, it is necessary to transform the theoretical distributions to the laboratory frame. This was done via

$$P' = \gamma P - \beta_{pt} \gamma E_{com}, \quad (3.19)$$

where P' is the momentum in the laboratory frame, P is the momentum in the c.o.m. frame, β_{pt} is the post-target β value defined in Eq. 3.3. The Lorentz factor, γ , was calculated via Eq. 3.2 using the mean value for the post-target β . The E_{com} value corresponds to the energy of the fragment in the centre-of-mass frame, defined as

$$E_{com} = \sqrt{P^2 + A^2}, \quad (3.20)$$

where A is the mass number of the fragment in MeV. Shown in Fig. 3.17 is an eikonal distribution before (black line) and after (red line) the c.o.m. frame to laboratory frame transformation. In this case the mean $\beta_{pt} = 0.287$ and the featured distribution corresponds to the $1d_{5/2}$ ground state of the ^{24}F fragment. After the eikonal distributions have been transformed to the lab. frame, convolution with the mother isotope's direct-beam-through-target (DBTT) momentum distribution may be performed.

3.7.3.2 Convolution of Theoretical LMDs

In order to compare the longitudinal momentum distributions with theoretical predictions for different shell orbitals, it is necessary to account for the momentum distribution of the incident beam nuclide as well as energy straggling in the target.

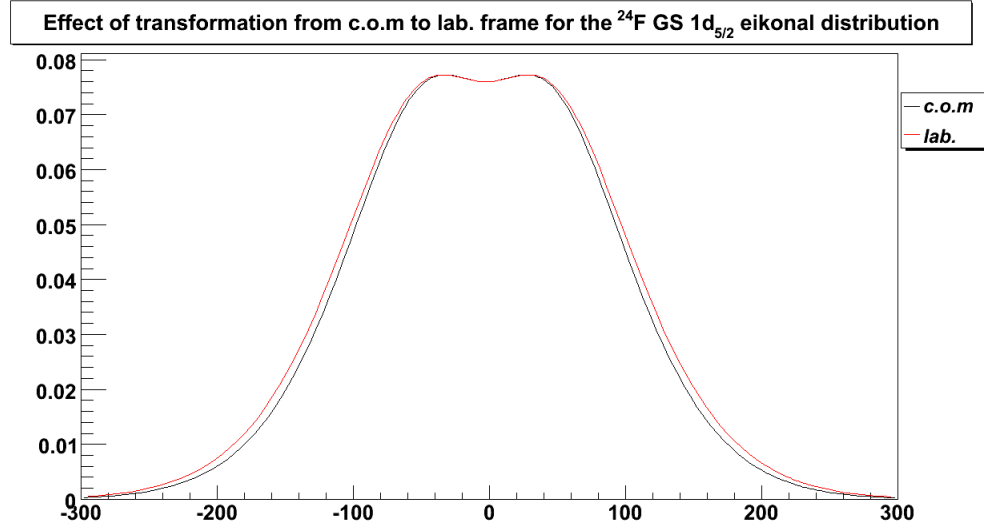


Figure 3.17: Transformation from centre-of-mass frame to laboratory frame.

This was achieved by fitting a Gaussian distribution to the LMD of each projectile which had passed unreacted through the target, with the SPEG $B\rho^{ref}$ (see Eq. 3.4) adjusted to align the unreacted beam in the centre of the focal plane. The Gaussian fit of each nuclide was then convolved with the theoretical predictions of its core fragment state LMD to give theoretical predictions that are directly comparable to the data. The direct-beam-through-target (DBTT) nuclide's momentum distributions are shown for the Fluorine isotopes and Oxygen isotopes in Fig. 3.18.

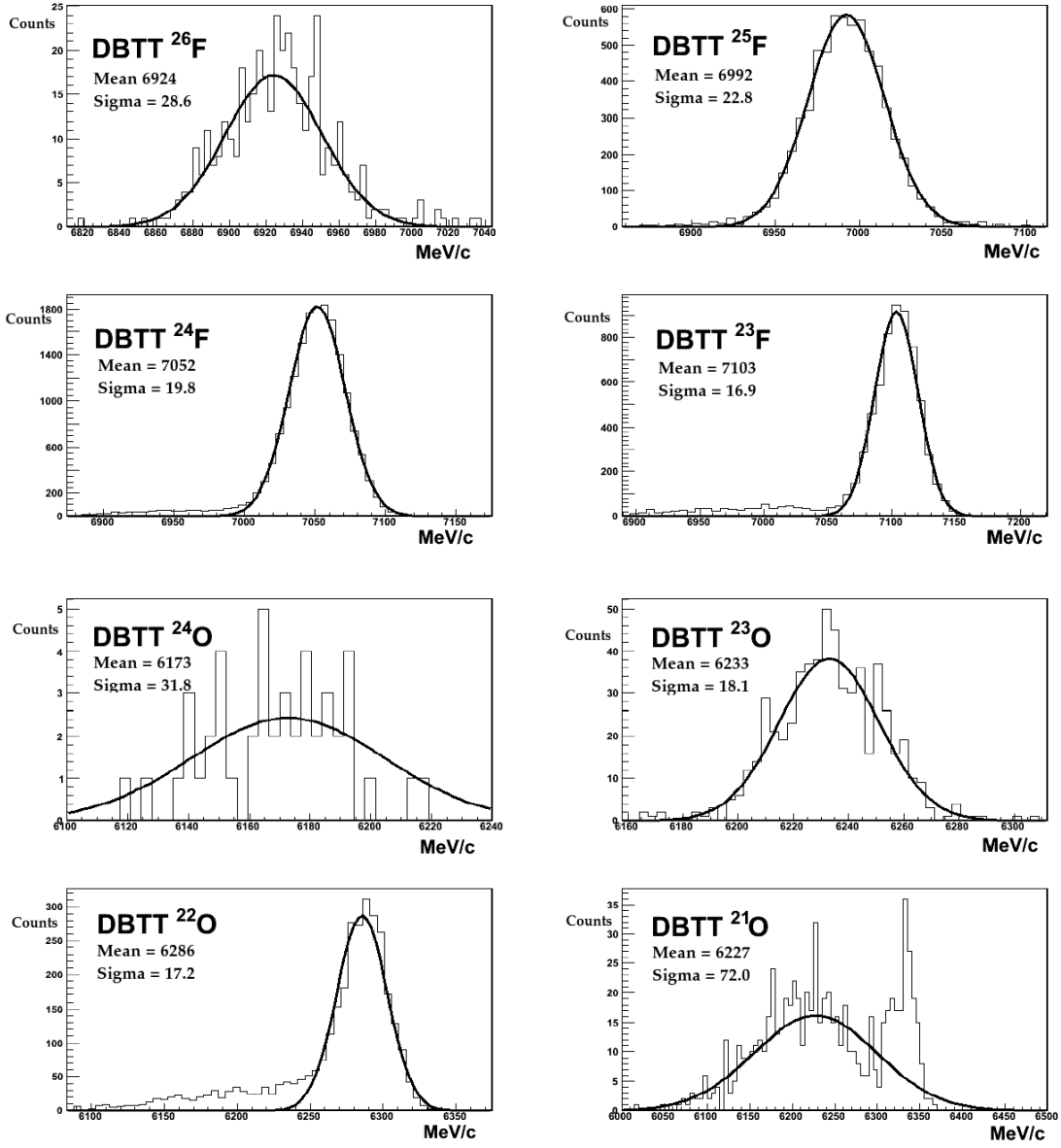


Figure 3.18: Direct-beam-through-target longitudinal momentum distributions.

Due to unresolved problems with SISSI, some of the longitudinal momentum distributions of the unreacted nuclide after passing through the target were observed not to be uniform. As can be seen, there is a significant low energy tail on the ^{22}O

momentum distribution as well as a highly irregular momentum distribution for ^{21}O . The consequence of this is that it was not possible to determine the angular momentum contribution to the momentum distribution for $^{21}\text{O} \rightarrow ^{20}\text{O}$. The nature of the PID cuts rules out contamination in these cases.

For the nuclides with appropriate direct-beam-through-target momentum distributions, a Gaussian distribution was fitted. The Gaussian distribution was then convolved with the theoretical output for the $A - 1$ fragment. Fig. 3.19 is an example of the convolution.

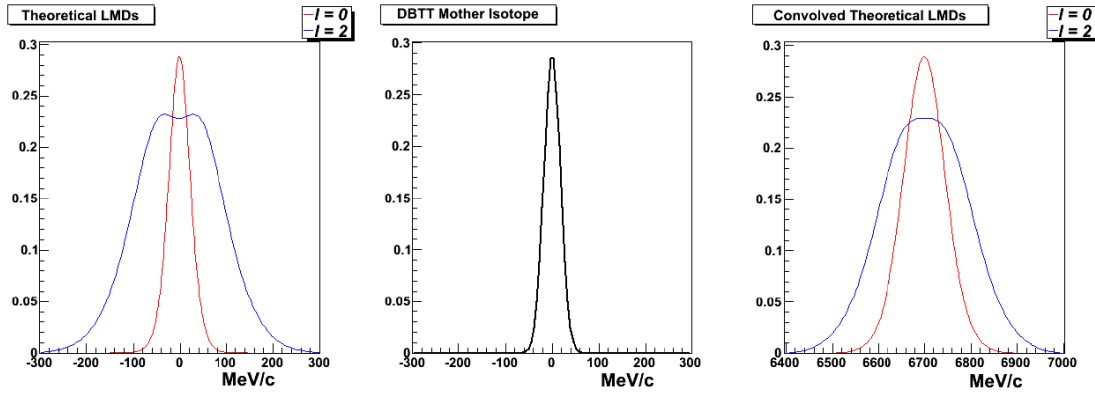


Figure 3.19: Convolution of Fragment Theoretical LMDs with the Projectile DBTT LMD.

3.7.4 Interactions and Model Spaces

When performing shell-model calculations [15] it is necessary to select interactions and model spaces appropriate to the nuclear region. The MSU version of OXBASH was used. Due to the nuclear region studied in this work, the $1d_{5/2}$, $2s_{1/2}$ and $1d_{3/2}$

orbitals, the *sdpn* model space was selected. This is the standard *sd* model space adapted into proton – neutron formalism, where the protons and neutrons are treated separately.

The interaction used for calculating the overlap between the ground state wavefunction of the A projectile and the excited (and ground) states of the $A - 1$ fragment was *wpn*, Wildenthal’s $A = 17\text{--}39$ USD interaction (July 1982) in the proton – neutron formalism. To predict energy levels using Hamiltonians calculated from more recent data, the USDAPN and USDBPN interactions were employed [14]. The original USD interaction was obtained from a least-squares fit of 380 values of energy data with experimental errors ≤ 0.2 MeV from 66 nuclei. The new interactions are taken from 608 states of 77 *sd*-shell nuclei, including data from neutron-rich nuclei, improved in both quality and quantity. The USDA Hamiltonian is more conservative, fitting more closely to the renormalised G matrix *sd*-shell (RGSD). The USDB Hamiltonian does not fit as closely to the RGSD, but gives a better fit to data. The single-particle root-mean-square (RMS) radii of neutron orbitals were found using Hartree-Fock calculations employing the sk20 (SKX) Skyrme interaction [2]. The value of nuclear diffuseness was set at the standard value of $a = 0.7$ fm [23]. It should be noted that the small differences (0.65 – 0.7) in the value chosen for the diffuseness have little impact on the results of the calculation with a fixed RMS radius [69]. The RMS radius of ^{12}C (the target) was set at 2.45 fm [26], the density distribution assumed to be Gaussian. There is a direct effect of the state energy on the RMS radius of the nucleon occupying each orbital. This in turn directly effects the single-particle cross sections calculated by eikonal theory, as previously discussed.

Chapter 4

Results and Discussion

In this chapter experimental results will be presented with theoretical predictions. Theoretical work includes the energy levels predicted by the USD, USDA and USDB interactions in an *sdpn* model space, compared to experimental results where possible. The USD predicted state energies and C^2S values have also been used in conjunction with eikonal reaction theory to give exclusive cross sections to each state. The sum of these exclusive cross sections to all (USD predicted) bound states yields a theoretical value for the inclusive cross section. Where conditions permit, experimental spectroscopic factors have been extracted and compared with predictions.

Eikonal reaction theory has also been used to predict theoretical longitudinal momentum distributions for the single-particle occupancy of each orbital in the *sd* model space. This set of theoretical predictions has been calculated for each considered state and compared with experimental results for the inclusive, and where possible exclusive, momentum distributions.

The implications of these results are considered in the context of previous findings and the consequence to our understanding of the structure discussed.

4.1 Inclusive One-Neutron Removal Cross Sections

For ease of reference Table 4.1 displays the measured inclusive cross sections for one neutron removal reactions from Oxygen and Fluorine projectiles. All significant errors (target thickness, statistical) have been accounted for. Theoretical eikonal predictions and previous work by Sauvan [56] have been included for comparison.

Table 4.1: Inclusive One-Neutron Removal Cross Sections.

Projectile	Beam Energy	Expt.	Eikonal	Expt. [56]	Beam Energy [56]
		σ_{-1n}	σ_{-1n}	σ_{-1n}	
	(A.MeV)	(mb)	(mb)	(mb)	(A.MeV)
^{26}F	41	60.3(17.8)	157.5	-	-
^{25}F	45	120.7(10.8)	138.2	173(46)	50
^{24}F	49	141.5(6.1)	161.8	124(16)	54
^{23}F	54	130.8(7.9)	-	114(12)	59
^{23}O	42	95.4(12.3)	184.1	-	-

It should be noted that the inclusive cross sections that compare less favourably to eikonal predictions (i.e. for projectiles ^{23}O and ^{26}F) suffered from low statistics, the

method used to overcome this possibly introducing a higher level of uncertainty than has been accounted for in the given error. The eikonal predicted cross sections were calculated for the exact experimental conditions of this work.

4.2 $^{23}\text{O} \rightarrow ^{22}\text{O}$

4.2.1 Discussion

The structure of ^{23}O has been an issue of some controversy in recent years. An experiment led by Kanungo [33] measured the core fragment ^{22}O inclusive momentum distribution following one neutron removal from ^{23}O . In this paper, predictions from eikonal theory were reported to suggest a possible $5/2^+$ ground state for ^{23}O , contrary to the previous $1/2^+$ prediction [55]. This was hypothesised to be due to a modification of the ^{22}O core in the ground state configuration of ^{23}O , with the $2s_{1/2}$ subshell descending below the $1d_{5/2}$ subshell. The conclusions of this paper, along with its mention of an “absence of proper reaction theory”, prompted a response from Brown et al [13], which stated that established eikonal reaction theory described the experimental observations of [33] well, the results supporting the prediction of a $1/2^+$ ground state for ^{23}O . Further evidence for a $1/2^+$ ground state followed [18, 43]. These reported that the structure of ^{23}O treated as a $2s_{1/2}$ neutron coupled to a ^{22}O (0^+) core gave a good agreement with the observed data.

4.2.2 Inclusive One-Neutron Removal Cross Sections

The experiment lead by Cortina–Gil [18] utilised the same reaction channel as this work, as did Kanungo [33]. Table 4.2 displays the measured σ_{-1n} for ^{23}O for previous experiments, accompanied by the corresponding eikonal prediction.

Table 4.2: ^{23}O Inclusive One-Neutron Removal Cross Sections

Source	σ_{-1n} (mb)	Eikonal (mb)	Beam Energy (A.MeV)
This Experiment	95.4(12.3)	184	42
Kanungo [33]	233(37)	185	72
Cortina-Gil [18]	85(10)	82	938

The Eikonal prediction of 184 mb was calculated for this work, the other predictions taken from their respective papers. There is a large discrepancy between the value measured in this work and the theoretical value. This may be explained by uncertainties introduced by the method used to combine data sets in order to overcome the poor statistics for this fragment.

The structure of ^{22}O has been investigated previously via γ -spectroscopy [64]. In the present experiment two transitions were observed at 1382(7) and 3195(9) keV, the quoted errors on the γ -ray energies calculated via Eq. 4.1. These transitions can be assigned as the known $3_1^+ \rightarrow 2_1^+$ (1383(4) keV) and $2_1^+ \rightarrow 0_1^+$ (3199(8) keV) transitions, placed in the previous level scheme shown in Fig. 4.1.

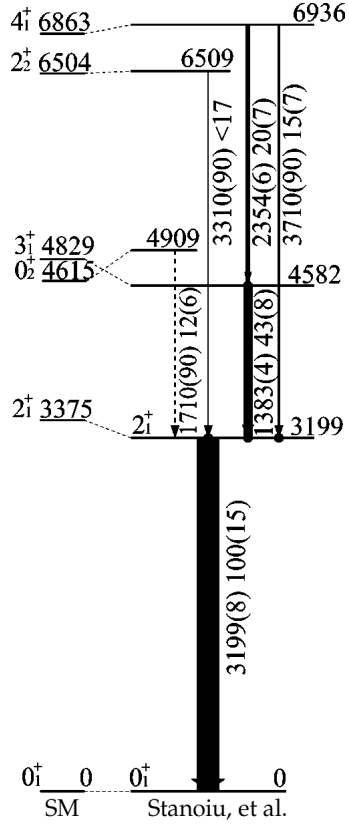
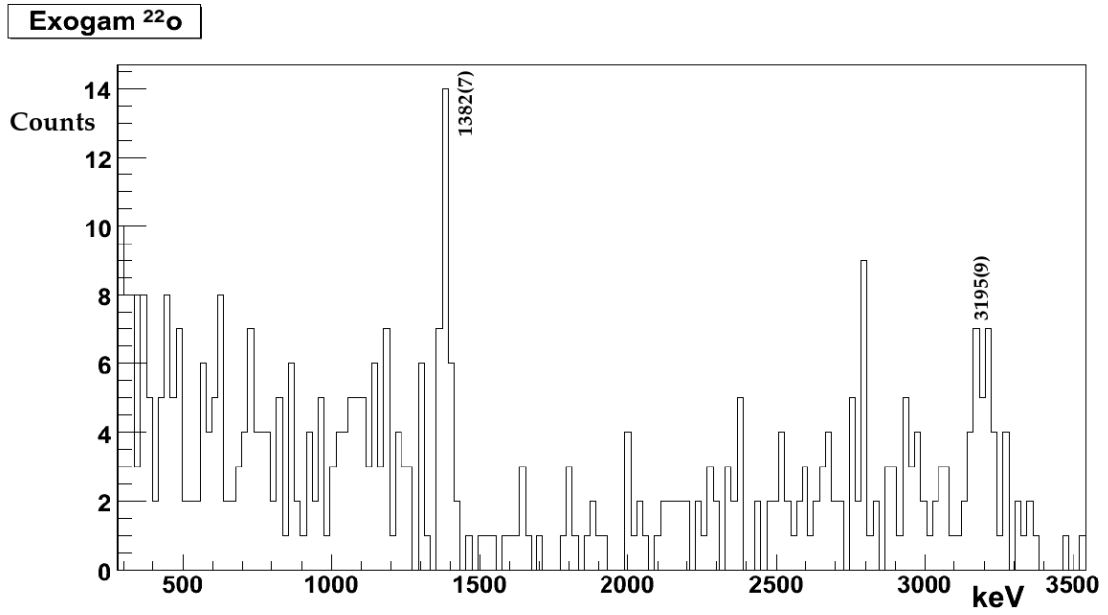


Figure 4.1: Level scheme of ^{22}O , taken from [64].

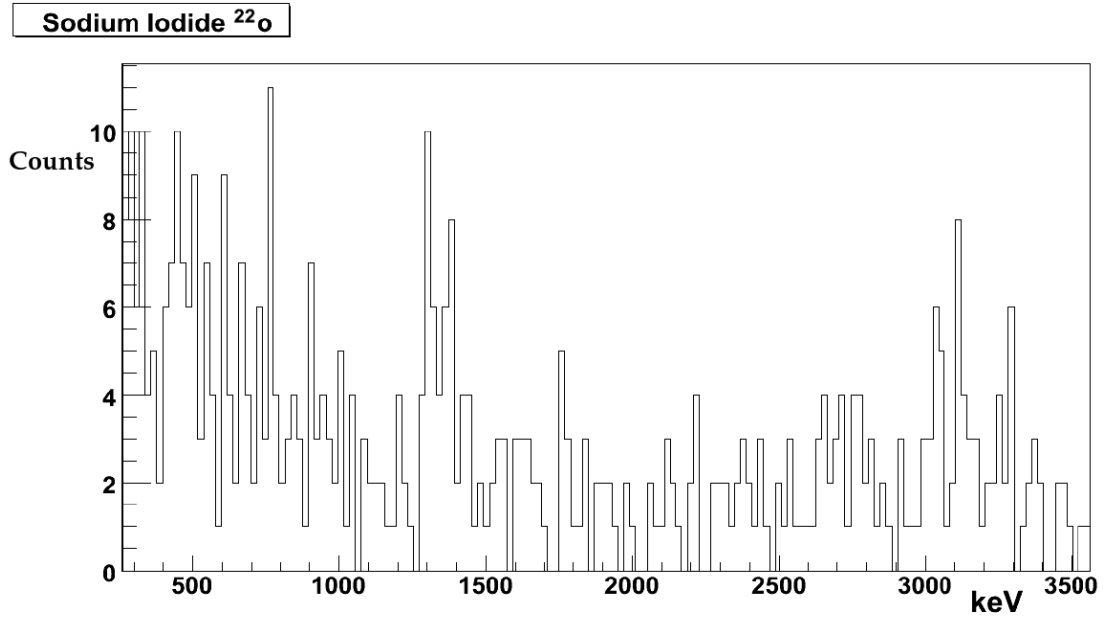
The measured γ spectra for the EXOGAM and NaI arrays are shown in Fig. 4.2. The errors on the γ -ray energies are given by

$$\frac{\sigma}{\sqrt{N}}, \quad (4.1)$$

where σ is taken from a Gaussian fit of the background subtracted peak, N being the integral. Errors corresponding to the calibration were also accounted for. Due to a combination of low statistics and a number of unobserved (but known) feeding transitions, it was not possible to determine exclusive measurements corresponding to the individual states.



(a) ^{22}O EXOGAM



(b) ^{22}O NaI

Figure 4.2: ^{22}O γ spectra.

Table 4.3 displays the C^2S values of each positive parity state below the neutron separation energy ($S_n = 6.85$ MeV) given by the USD interaction as well as the corresponding exclusive cross sections predicted by eikonal theory.

Due to the conservation of angular momentum, the maximum possible spin for the ^{22}O fragment following one neutron removal is 3^+ . This assumes an initial ground state occupation for the projectile, taken as $1/2^+$ for ^{23}O [18, 43].

Table 4.3: Predicted occupancies for $^{23}\text{O} \rightarrow ^{22}\text{O}$ using the USD interaction.

E_{level} (MeV)	I^π	$C^2S_{2s_{1/2}}$	$C^2S_{1d_{3/2}}$	$C^2S_{1d_{5/2}}$	$\sigma_{2s_{1/2}}$ (mb)	$\sigma_{1d_{3/2}}$ (mb)	$\sigma_{1d_{5/2}}$ (mb)	σ_{state} (mb)
0.000	0_1^+	0.797	-	-	53.54	0.00	0.00	53.54
3.376	2_1^+	-	0.053	2.077	0.00	1.38	51.49	52.87
4.617	0_2^+	0.115	-	-	3.90	0.00	0.00	3.90
4.828	3_1^+	-	-	3.079	0.00	0.00	68.85	68.85
6.504	2_2^+	-	0.005	0.237	0.00	0.11	4.80	4.90
SUM ($\sigma_{\text{theo.}}$)					57.43	1.49	125.14	184.06

In Table 4.3 it is useful to note the summed exclusive cross section to each orbital. As the orbital angular momentum l affects the spin independent LMD, the $1d_{3/2}$ and $1d_{5/2}$ subshells can be combined to give the d-wave contribution. In this way the predicted ratio of s-wave to d-wave occupancy can be calculated for the inclusive

momentum distribution. In the case of the ^{22}O core fragment the ratio is $\sim 1 : 2.2$.

4.2.3 Longitudinal Momentum Distributions

As statistics for this core fragment were scarce it was not possible to gate on the transitions to extract exclusive momentum distributions. Shown in Fig. 4.3 is the inclusive longitudinal momentum distribution for ^{22}O , overlayed with theoretical predictions assuming ground state occupancy. The inclusive distribution seems to have a strong s-wave component, which disagrees with the predicted occupancy (see Table 4.3). Although the ground state has a pure s-wave structure, the sum of the excited state's predicted cross sections is more than double that of the ground state, with the main excited states (2_1^+ , 3_1^+) having a pure d-wave component. Some support of a higher relative occupation of the $2s_{1/2}$ orbital than predicted comes from [35], in which eikonal LMD predictions were compared with data from [33], see Fig. 4.4.

The eikonal predictions for the inclusive momentum distribution revealed a stronger s-wave component in the measured distribution than the s-wave : d-wave $1 : 2.2$ ratio predicted by shell model calculations, see Fig. 4.3. Some support of this observation is given by [35] who took inclusive LMD data from [33] and overlayed it with eikonal LMD predictions for the different substates, shown in Fig. 4.4.

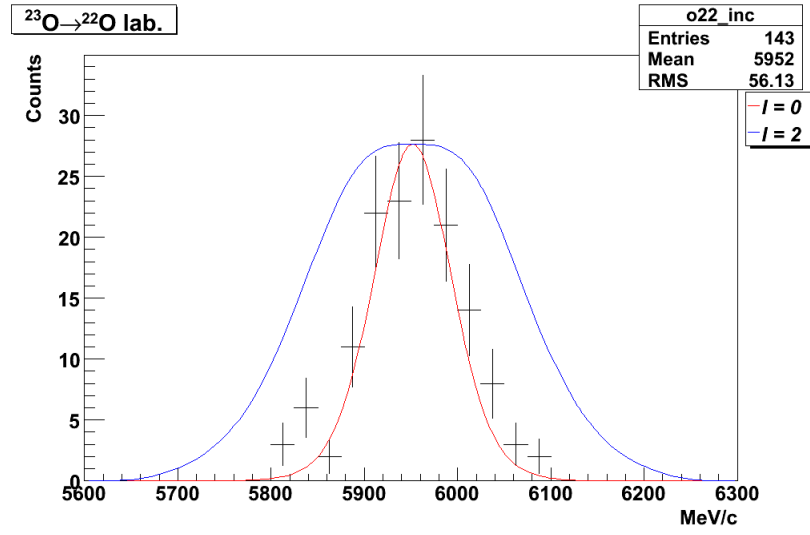


Figure 4.3: ^{22}O Inclusive LMD from this experiment.

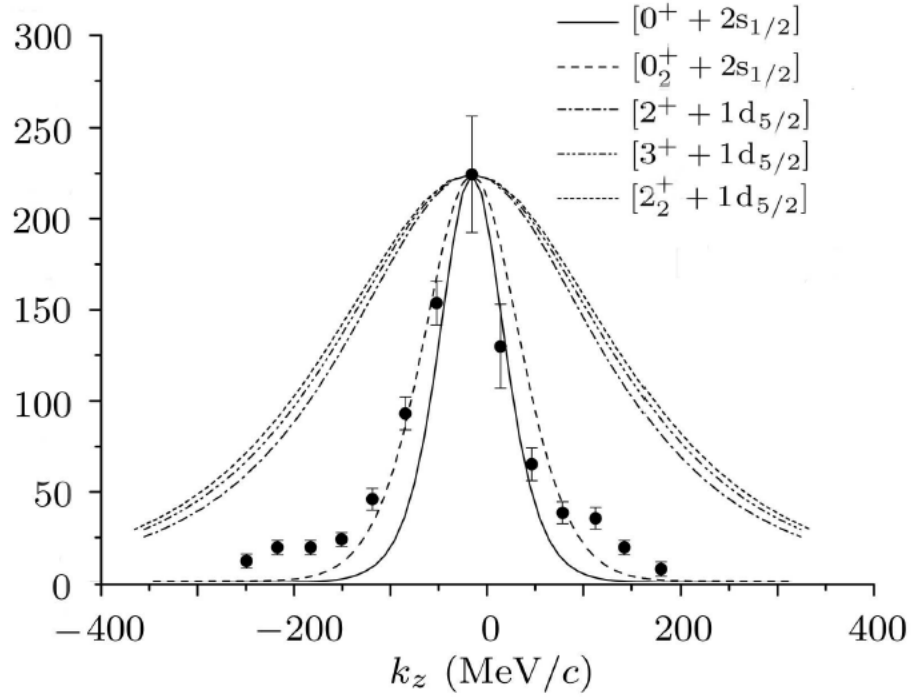


Figure 4.4: ^{22}O Inclusive LMD taken from [35]. Data from [33].

4.3 $^{24}\text{F} \rightarrow ^{23}\text{F}$

4.3.1 Discussion

The shifting of magic numbers from $N = 20$ to $N = 16$ as the neutron dripline is approached has been attributed to a two-body attractive tensor interaction between the $\pi d_{3/2}$ and $\nu d_{5/2}$ shells (see Section 1.5.2).

Excited states in ^{23}F have been interpreted as a weak coupling of the single $1d_{5/2}$ proton with the 2_1^+ phonon state in ^{22}O [6]. The measured state energies for each nucleus, along with shell-model predictions for ^{23}F , are shown in Fig. 4.5.

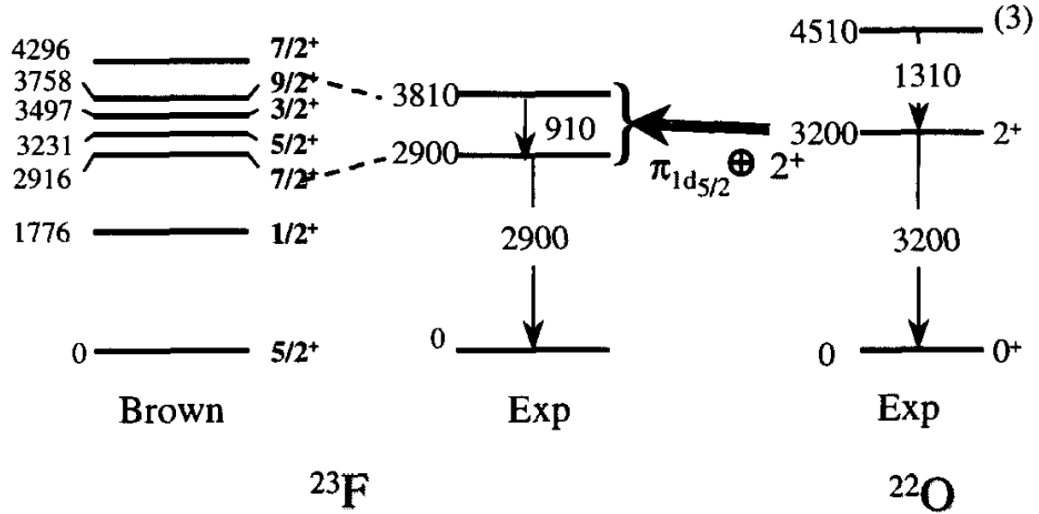
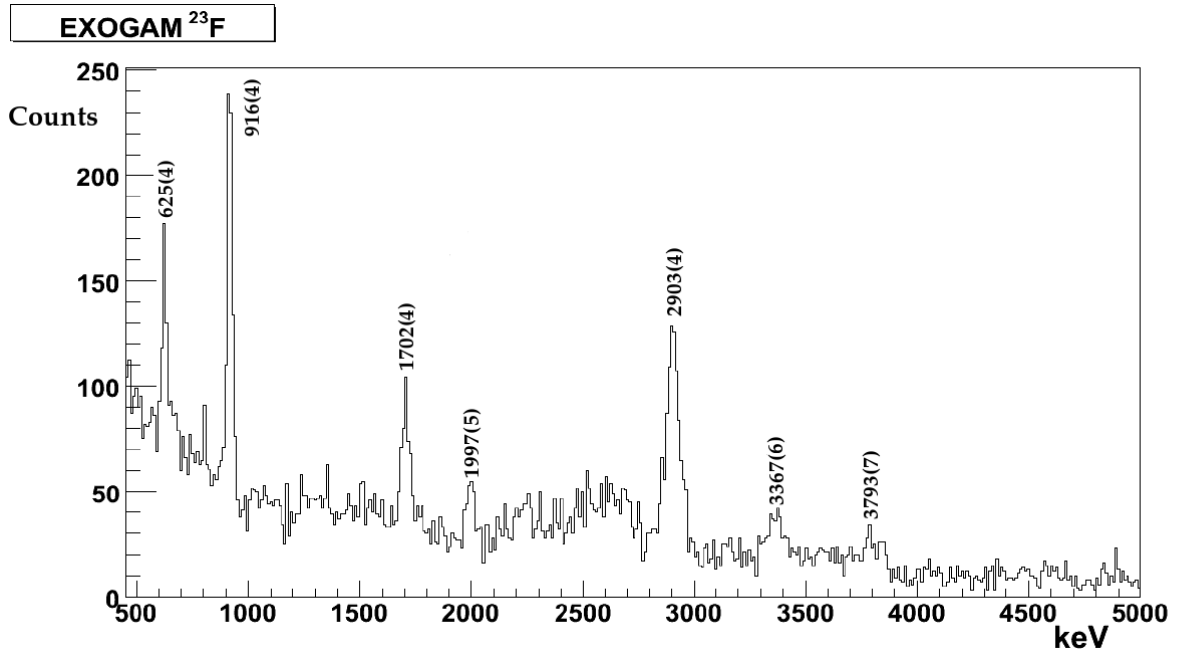
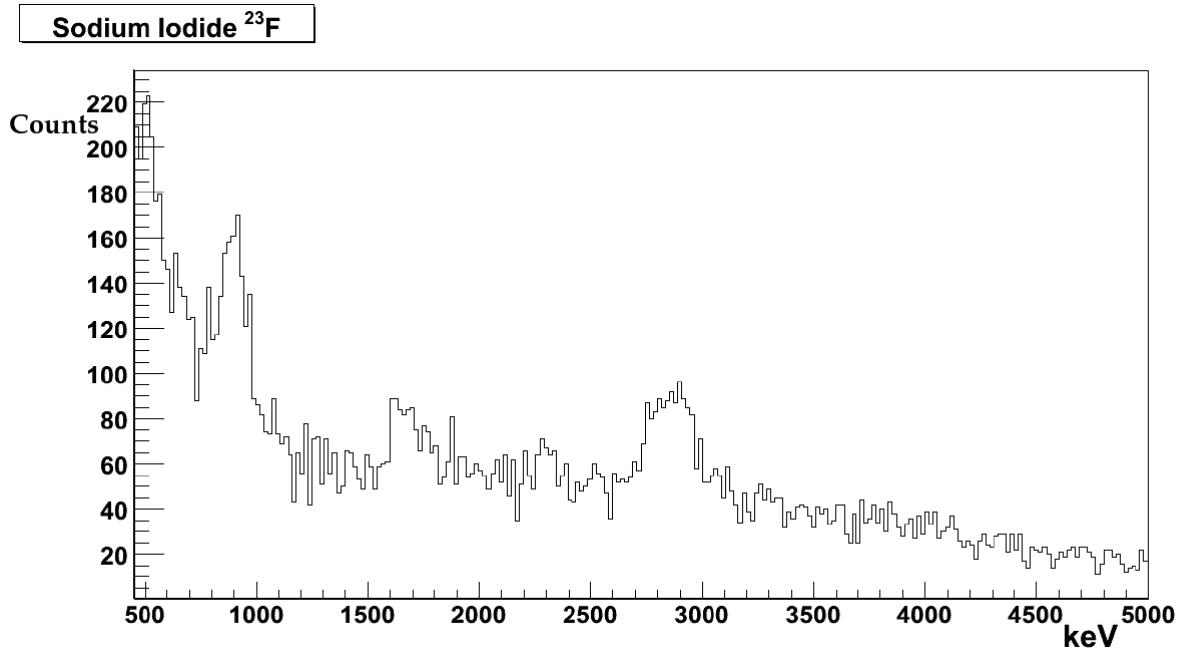


Figure 4.5: Comparison of ^{22}O and ^{23}F state energies, taken from [6].

In Fig. 4.6 are shown the γ spectra measured with the EXOGAM and NaI arrays. Transitions at 625(4), 916(4), 1702(4), 1997(5), 2903(4), 3367(6) and 3793(7) keV were observed.



(a) ^{23}F EXOGAM



(b) ^{23}F NaI

Figure 4.6: ^{23}F γ spectra.

4.3.2 $\gamma\gamma$ Coincidences

Shown in Fig. 4.7 are the EXOGAM $\gamma\gamma$ coincidence spectra for the observed transitions in ^{23}F . Observed γ -ray energies are shown as dotted red lines for a visual aid.

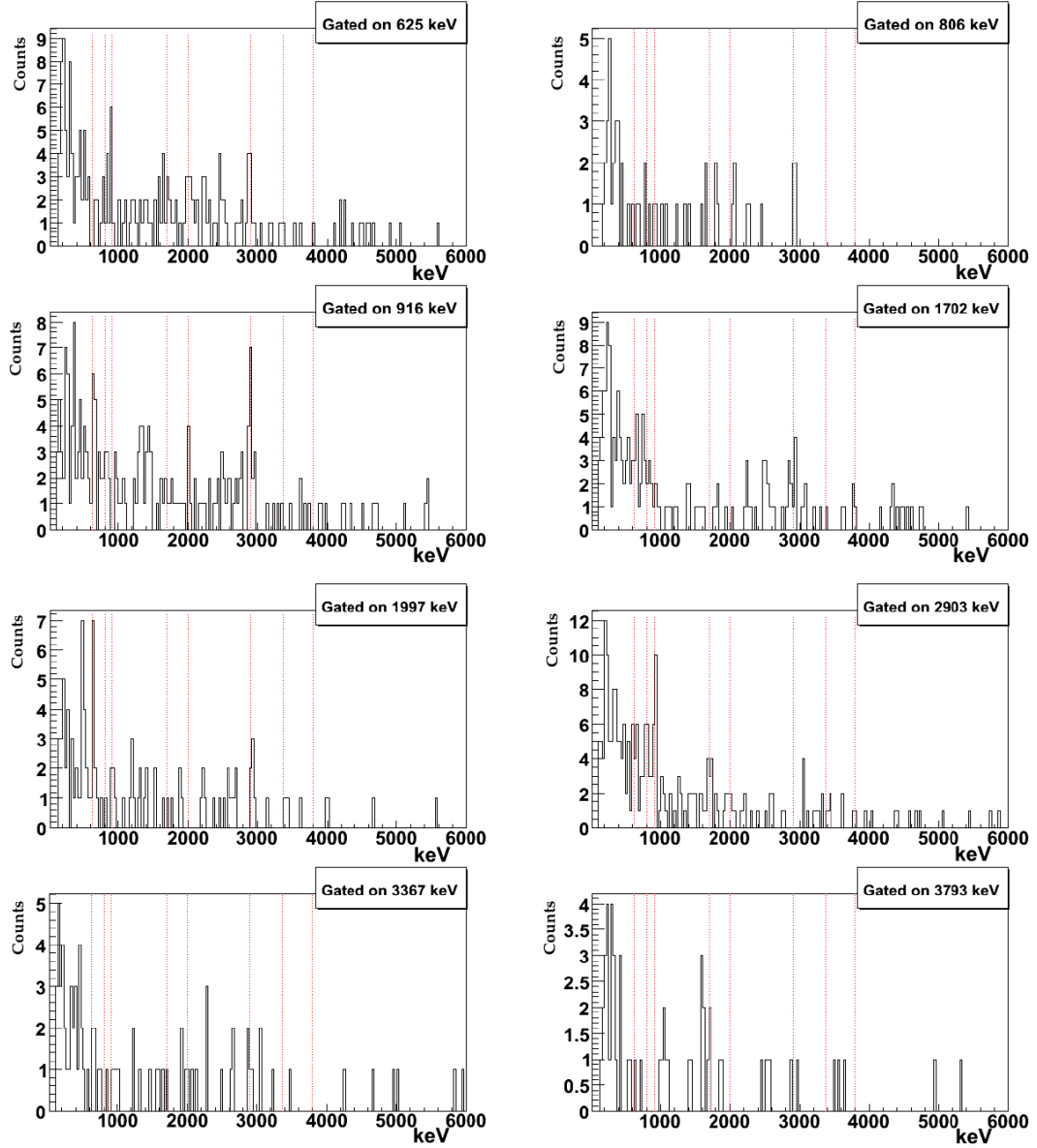


Figure 4.7: EXOGAM $\gamma\gamma$ coincidences for ^{23}F .

In Table 4.4 the coincidence data are shown. Asterisks denote coincidences which do not comply to the level scheme shown in Fig. 4.8. These denoted coincidences have poor statistics and are not conclusive. Values in **bold** denote good confidence in the coincidence.

Table 4.4: $\gamma\gamma$ Coincidences for ^{23}F .

E_γ (keV)	Coinc. E_γ (keV)	E_γ (keV)	Coinc. E_γ (keV)
625	916*	1702	2903
	1702*		3793
	1997	1997	625
	2903		2903
916	625	2903	916
	1997*		1702
	2903	3793	1702

Both the $\gamma\gamma$ coincidence information and the level scheme of ^{23}F proposed by Michimasa, et al [41], have been used to place the observed transitions, shown in Fig. 4.8. For the experiment presented in this thesis, peak energies above the calibration range can not be considered as accurate, as the third-order calibration increasingly diverges after the highest calibration energy, 3.2 MeV. The observed 3367(6), 3793(7) keV peaks correspond to the 3378, 3858 keV γ -ray energies of Michimasa, et al [41].

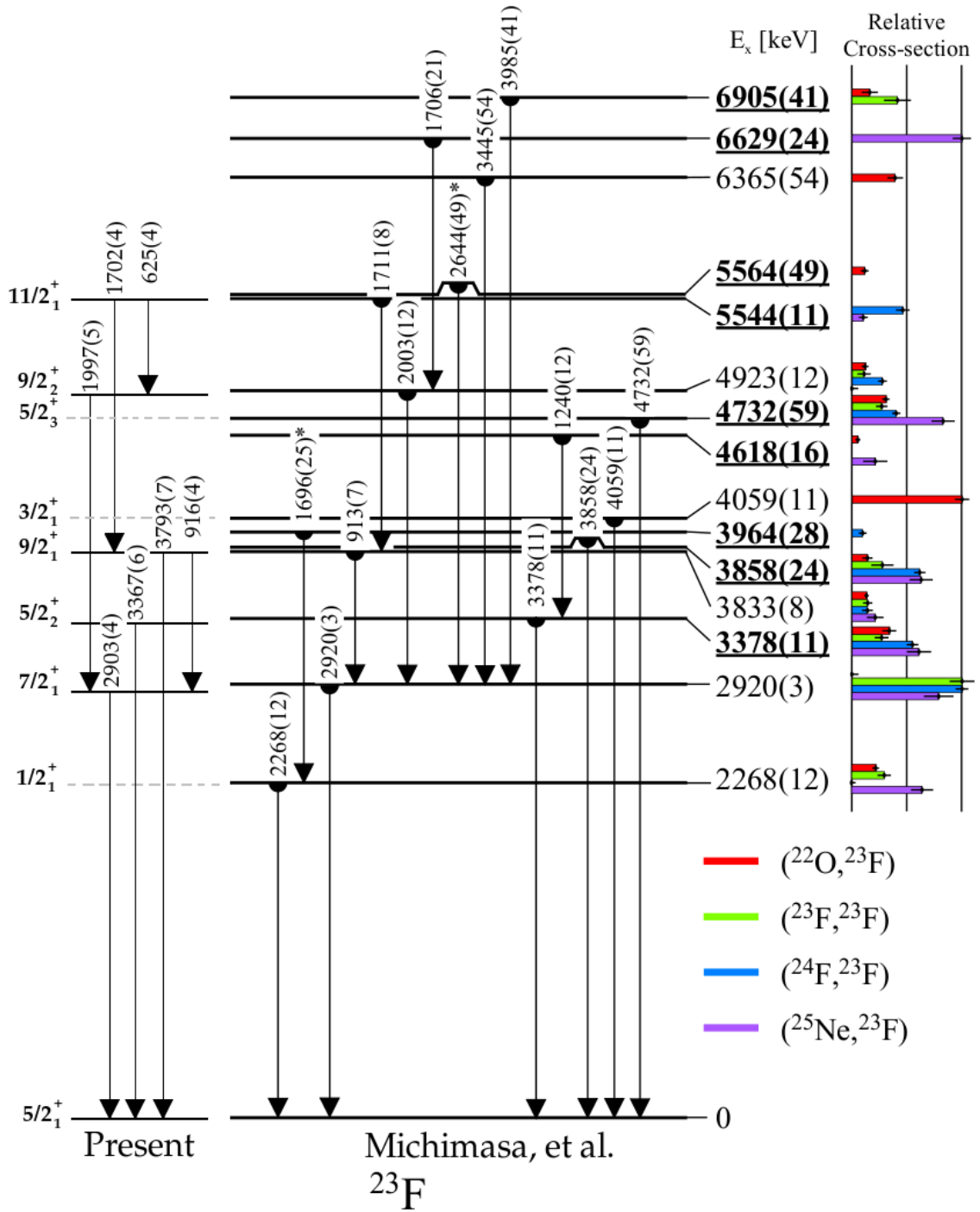


Figure 4.8: Level Scheme of ^{23}F , adapted from [41].

When performing shell model calculations there are a number of different possible model spaces and interactions. Shown in Fig. 4.9 are the different energy levels obtained with the USD, USDA and USDB interactions using the shell model code OXBASH [15]. All interactions use the pn formalism, which treats the protons and neutrons separately. The model space was chosen to be sd_{pn} for all three theoretical cases shown, which is the sd model space in the pn formalism. The experimental levels shown on the right of the figure correspond to the findings of Michimasa, et al. [41].

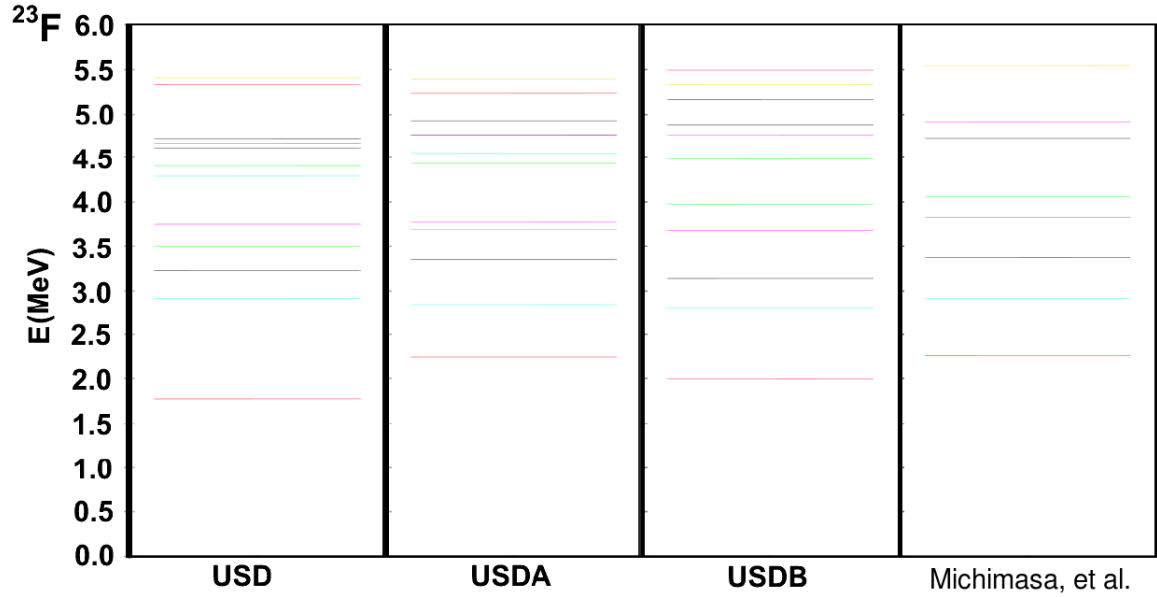


Figure 4.9: ^{23}F Shell-model predicted levels compared to experiment by Michimasa et al [41]. The red lines correspond to $1/2^+$ states, green $3/2^+$, black $5/2^+$, cyan $7/2^+$, magenta $9/2^+$ and gold $11/2^+$.

The USDA interaction seems to predict the energy of the states with better accuracy, though the USDB interaction is the only one of the three interactions to

predict the correct ordering of the $9/2_1^+$ and $3/2_1^+$ states.

Table 4.5 gives the transitions from different energy states observed in this experiment, accompanied by their intensities both before and after feeding subtraction. The observed transitions were placed in the level scheme shown in Fig. 4.8. The transitions labelled with an asterisk were not seen previously and are only speculatively assigned.

Table 4.5: ^{23}F γ intensities.

$E_{level}(\text{MeV})$ [41]	$E_\gamma(\text{MeV})$	$I(\%)$	$I_{fs}(\%)$
0.000	-	-	69.83(2.80)
2.920(3)	2.903(4)	20.22(1.39)	11.97(1.65)
3.378(11)	3.367(6)	3.95(0.14)	3.95(0.14)
3.833(8)	0.916(4)	7.40(0.76)	3.41(1.35)
	3.793(7)	2.54(0.75)	1.17(1.69)
4.923(12)	1.997(5)	0.85(0.47)	0.85(0.47)
5.544(11)	0.625(4)*	2.74(0.33)	2.74(0.33)
	1.702(4)	5.36(0.31)	5.36(0.31)

The E_{level} values reported in Table 4.5 are taken from Michimasa, et al [41]. The E_γ values were those observed in this experiment. The findings of [41] were interpreted theoretically by Brown, et al [59], who remarked upon a ~ 0.6 MeV peak present in Figure 1. of [41], which is not commented upon in the paper. Brown, et al, assigned this peak as the $11/2_1^+ \rightarrow 9/2_2^+$ transition [59].

The previously assigned $11/2_1^+$ and $9/2_2^+$ states give $\Delta E = 621$ keV [41], corresponding closely to the 625(4) keV transition observed in this experiment. $\gamma\gamma$ coincidence with the 916(4) keV, 1997(5) and 2903(4) keV transitions further support this placement. However, there is a violation in the intensity balancing, as the intensity of the 625(4) keV transition feeding the $9/2_2^+$ state is greater than the only known transition decaying out (2.74 > 0.85 %). The 625(4) keV transition was subsequently not included in the feeding subtraction for the $9/2_2^+$ state.

This violation could be accounted for by the existence of other transitions from the $9/2_2^+$ state. To investigate the possibility that the intensity imbalance is due to a competing transition from the $9/2_2^+$ state, Weisskopf estimates [79] can be used to give a rough prediction of the lifetime of different transitions from this state. The observed 1997(5) keV is an M1 transition, with a predicted lifetime of 2.7 fs. There is a possible transition at 4.89 MeV present in Fig. 4.6(a), but this cannot be confidently identified. The theoretical 4923 keV transition to the ground state has a predicted lifetime of 0.2 fs for an M1 transition and 50.5 fs for an E2 transition [79]. So it seems likely that an unseen $9/2_2^+ \rightarrow 5/2_1^+$ M1 transition could explain the imbalance in intensities.

The shell-model predicts the $11/2_1^+$ state to decay both to the $9/2_1^+$ state (56%) and the $9/2_2^+$ state (43%) [59]. If the 625(4) keV is indeed the $11/2_1^+ \rightarrow 9/2_2^+$ transition (with a USDB predicted energy of 0.56 MeV), then the experimental values of 34(4)% and 66(5)% are quite different from the values theoretically predicted. For the $9/2_1^+$ state, the transition to the ground state was predicted to be 61%, with 39% decaying to the $7/2_1^+$ state [59]. The experimental values give 26(8)% and 74(11)% – a notable difference.

All levels below the neutron separation energy ($S_n = 7.530$ MeV) calculated with the USD interaction are shown in Table 4.6. Also shown are the spectroscopic factors and single-particle cross sections for the $2s_{1/2}$, $1d_{3/2}$ and $1d_{5/2}$ orbitals and the exclusive cross sections for each state, σ_{state} . The theoretical cross section calculations included a centre-of-mass correction (see Eq. 3.17), whereas the tabulated C^2S values do not. In Table 4.6 the states underlined relate to observed transitions in this experiment.

Table 4.6: Predicted Occupancies for $^{24}\text{F} \rightarrow ^{23}\text{F}$ using the USD interaction.

E_{level} (MeV)	I^π	$C^2S_{2s_{1/2}}$	$C^2S_{1d_{3/2}}$	$C^2S_{1d_{5/2}}$	$\sigma_{2s_{1/2}}$ (mb)	$\sigma_{1d_{3/2}}$ (mb)	$\sigma_{1d_{5/2}}$ (mb)	σ_{state} (mb)
0.000	$5/2_1^+$	0.736	0.014	0.093	37.99	0.43	3.00	41.41
1.776	$1/2_1^+$	-	-	0.073	0.00	0.00	1.99	2.08
2.918	$7/2_1^+$	0.005	0.008	0.444	0.17	0.19	11.05	11.91
3.233	$5/2_2^+$	0.020	0.001	0.374	0.68	0.04	9.12	10.30
3.496	$3/2_1^+$	-	0.002	0.017	0.00	0.04	0.41	0.47
3.757	$9/2_1^+$	-	0.004	0.960	0.00	0.10	22.61	23.70
4.295	$7/2_2^+$	0.008	0.000	0.378	0.26	0.01	8.62	9.29
4.406	$3/2_2^+$	-	0.001	0.197	0.00	0.02	4.47	4.68
4.612	$5/2_3^+$	0.040	0.000	0.096	1.21	0.01	2.15	3.57
4.664	$9/2_2^+$	-	0.034	0.211	0.00	0.80	4.70	5.73
4.729	$5/2_4^+$	0.054	0.000	0.032	1.62	0.00	0.70	2.49
5.335	$1/2_2^+$	-	-	0.020	0.00	0.00	0.43	0.45
5.411	$11/2_1^+$	-	-	1.056	0.00	0.00	22.58	23.56
5.631	$5/2_5^+$	0.001	0.002	0.125	0.04	0.05	2.64	2.85
5.651	$3/2_3^+$	-	0.003	0.008	0.00	0.06	0.16	0.23
5.999	$7/2_3^+$	0.034	0.008	0.033	0.94	0.17	0.69	1.91
6.376	$1/2_3^+$	-	-	0.042	0.00	0.00	0.87	0.90
6.426	$3/2_4^+$	-	0.000	0.003	0.00	0.00	0.07	0.08
6.431	$5/2_6^+$	0.010	0.000	0.019	0.26	0.00	0.38	0.68
6.447	$9/2_3^+$	-	0.001	0.035	0.00	0.02	0.70	0.76
6.765	$3/2_5^+$	-	0.001	0.158	0.00	0.02	3.17	3.33
6.772	$9/2_4^+$	-	0.002	0.077	0.00	0.04	1.55	1.65
6.777	$11/2_2^+$	-	-	0.284	0.00	0.00	5.68	5.93
6.922	$5/2_7^+$	0.005	0.000	0.075	0.14	0.00	1.50	1.72
6.986	$7/2_4^+$	0.002	0.000	0.050	0.06	0.00	0.99	1.10
7.169	$7/2_5^+$	0.001	0.000	0.010	0.03	0.00	0.19	0.24
7.191	$9/2_5^+$	-	0.001	0.012	0.00	0.01	0.23	0.25
7.317	$5/2_8^+$	0.004	0.000	0.016	0.10	0.00	0.32	0.44
7.335	$9/2_6^+$	-	0.000	0.006	0.00	0.01	0.11	0.12
SUM ($\sigma_{\text{theo.}}$)					43.49	1.99	111.08	161.82

4.3.3 Exclusive One-Neutron Removal Cross Sections and Spectroscopic Factors

The assignment of states allows the determination via Eq. 3.17 of theoretical exclusive cross sections, σ_{state} , shown in Table 4.6. The product of the measured inclusive cross section and branching ratio yields the experimental one-neutron removal exclusive cross section, σ_{ex} .

In order to compare theoretical and experimental spectroscopic factors, a single spectroscopic factor for each state, $C^2S_{theo.}$, is required. The $C^2S_{theo.}$ value was taken as the sum of the orbital C^2S_{nlj} values after their respective centre-of-mass (c.o.m.) corrections were applied. Results are shown in Table 4.7. The overall single-particle cross section of each state, σ_{sp} , was determined by the sum of the $2s_{1/2}$, $1d_{3/2}$ and $1d_{5/2}$ single-particle cross sections, weighted by the state's predicted occupancies [15] following a c.o.m. correction. For the ground state the high value of σ_{ex} relative to σ_{state} can be explained by numerous low intensity population of states (see Table 4.6) that were not observed, and so were not accounted for in the calculation.

Assignment of spin and parity has been included in Table 4.7, taken from [41]. The branching ratio values for the state, $b(\%)$, are the sum of the transition intensity, $I_{fs}(\%)$, (feeding subtracted) values decaying from the said state (see Table 4.5). Due to the intensity violation previously described, the 625(4) keV transition was not included in the 5.544 MeV state $b(\%)$ calculation. If it did indeed decay from the 5.544 MeV state, its inclusion would increase the experimental C^2S value. The

625(4) keV transition was included in the ground state branching ratio calculation. Three of the states ($9/2_1^+$, $9/2_2^+$, $11/2_1^+$) have no s-wave component as this is not possible with angular momentum coupling. Additionally, shell-model predictions give an almost pure $1d_{5/2}$ prediction for the $7/2_1^+$ and $5/2_2^+$ states. As many states are predicted to have dominant occupation in one orbital [15], this is included as a guide in the third column of Table 4.7. The E_{level} values displayed were taken from [41].

Table 4.7: Exclusive Cross Sections and Spectroscopic Factors for $^{24}\text{F} \rightarrow ^{23}\text{F}$.

E_{level} (MeV)	I^π	Occupancy	b (%)	σ_{sp} (mb)	σ_{ex} (mb)	σ_{state} (mb)	$C^2 S_{theo.}$	$C^2 S_{expt.}$
0.000	$5/2_1^+$	$2s_{1/2}$	69.83(2.91)	45.11	98.79(5.92)	41.27	0.92	2.19(0.13)
2.920	$7/2_1^+$	$1d_{5/2}$	11.97(1.65)	22.97	16.94(2.45)	11.42	0.50	0.74(0.11)
3.378	$5/2_2^+$	$1d_{5/2}$	3.95(0.14)	22.82	5.59(0.31)	9.90	0.43	0.25(0.01)
3.833	$9/2_1^+$	$1d_{5/2}$	4.58(1.11)	21.62	6.47(1.60)	22.71	1.05	0.30(0.07)
4.923	$9/2_2^+$	$1d_{5/2}$	0.85(0.47)	20.62	1.20(0.66)	5.49	0.27	0.06(0.03)
5.544	$11/2_1^+$	$1d_{5/2}$	5.36(0.31)	19.64	7.58(0.55)	22.58	1.15	0.39(0.03)

The summation of the fragment state's occupancies relate to the relative subshell occupancies of the projectile, presumed to be in its ground state. However, fragment states populated in the continuum cannot be accounted for as they are unbound, introducing a degree of uncertainty.

4.3.4 Longitudinal Momentum Distributions

The measured inclusive and exclusive LMDs for $^{24}\text{F} \rightarrow ^{23}\text{F}$ are presented in Figs. 4.10 to 4.18. Examining firstly the inclusive LMD (Fig. 4.10) a combination of the s-wave, d-wave theoretical predictions can be observed, as is to be expected [15]. However, the s-wave contribution seems to be dominant, which is contrary to shell model and eikonal calculations, which predict a $\sim 1:2.6$ ratio of s-wave to d-wave contribution (see Table 4.6) to the inclusive ^{23}F distribution. The ground state of ^{23}F is predicted to show a dominant $2s_{1/2}$ occupancy (Table 4.6). This is indeed reflected by the LMD (Fig. 4.11) exhibiting an almost pure s-wave distribution, confirming that the ground state of ^{23}F is the $5/2_1^+$, as no other states have a predicted $2s_{1/2}$ dominant occupancy. The 2903(4) keV gated $7/2_1^+$ state is predicted to have an almost pure $d_{5/2}$ occupancy (see Table 4.6). This is not clearly reflected in the LMD (Fig. 4.16), which seems to have an even contribution from s-wave and d-wave components.

For the 3367(6) keV gated $5/2_2^+$ state, a $1d_{5/2}$ dominant occupancy is predicted. The observed LMD (Fig. 4.17) does agree with this, albeit with large errors due to comparatively low statistics. If the 916(4) and 3793(7) keV γ transitions have been correctly assigned as decaying from the $9/2_1^+$ it would be expected that their coincident LMDs would be the same. The 916(4) keV gated LMD (Fig. 4.13) agrees well with the pure d-wave theoretical shell-model prediction, whereas the 3793(7) keV gated LMD (Fig. 4.18) has a less evident agreement due to it having $\sim 1/3$ of the 916(4) keV branching ratio and a loss of γ detection efficiency, resulting in a higher statistical error.

Shell-model predictions give an almost pure $1d_{5/2}$ occupancy for the $9/2_2^+$ state. This is consistent with the 1997(5) keV gated LMD (Fig. 4.15). Finally, a pure $1d_{5/2}$ occupancy is predicted for the $11/2_1^+$ state. The LMD gated on the 1702(4) keV transition (Fig. 4.14) does show a dominant d-wave distribution, but there seems to be a contribution ($\sim 1/5$) from the s-wave distribution. This can be assumed a statistical anomaly, as angular momentum coupling forbids an s-wave contribution. A similar distribution can be seen for the LMD associated with the 625(4) keV transition (Fig. 4.12), which as previously discussed is a candidate for decay from the $11/2_1^+$ state.

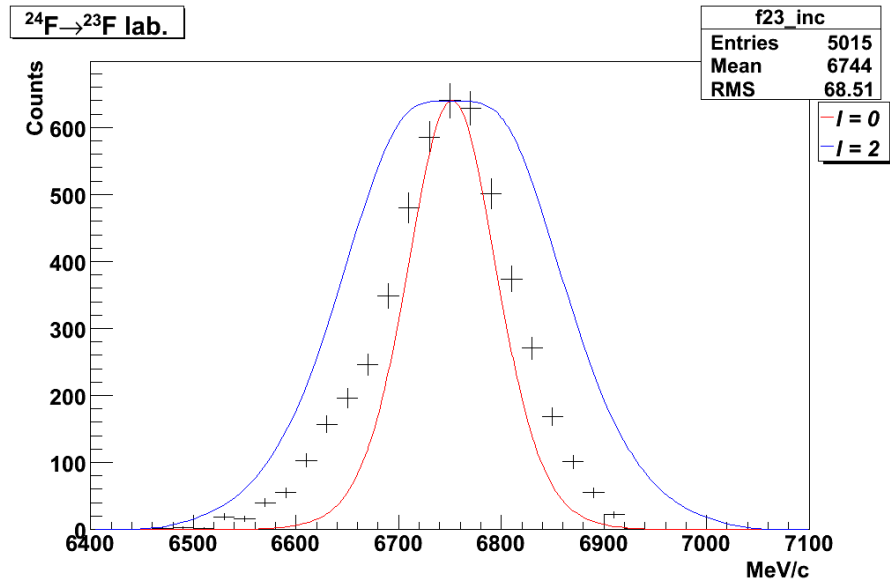


Figure 4.10: ^{23}F Inclusive LMD.

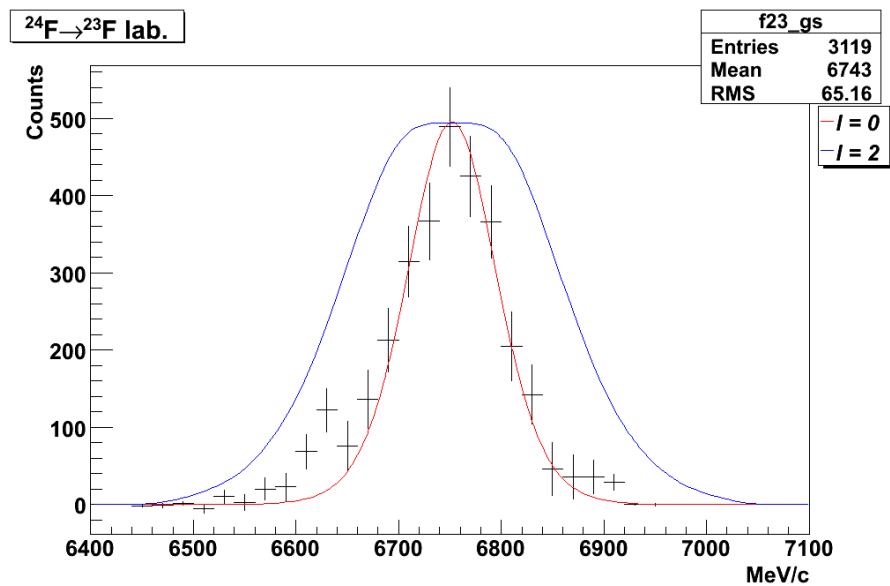


Figure 4.11: ^{23}F ground state LMD.

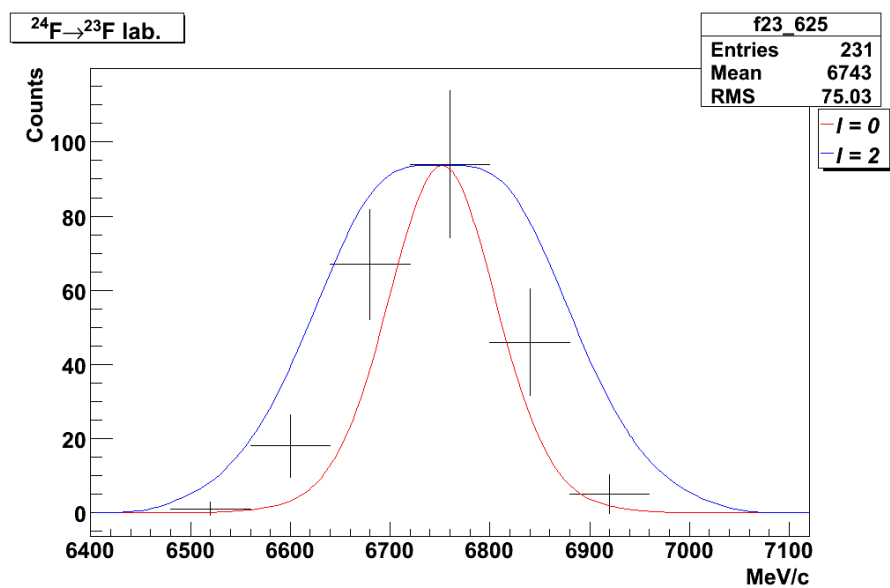


Figure 4.12: ^{23}F 625(4) keV coincident LMD.

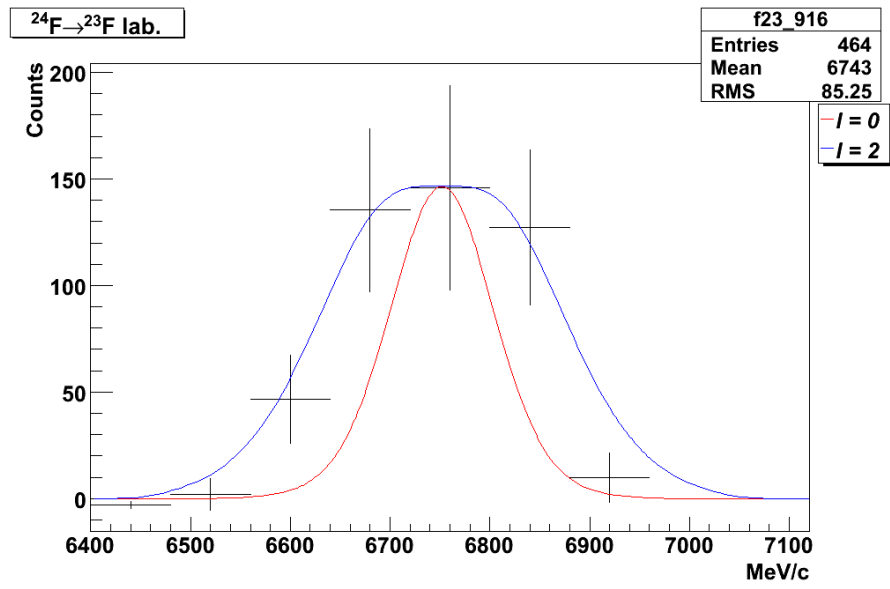


Figure 4.13: ^{23}F 916(4) keV coincident LMD.

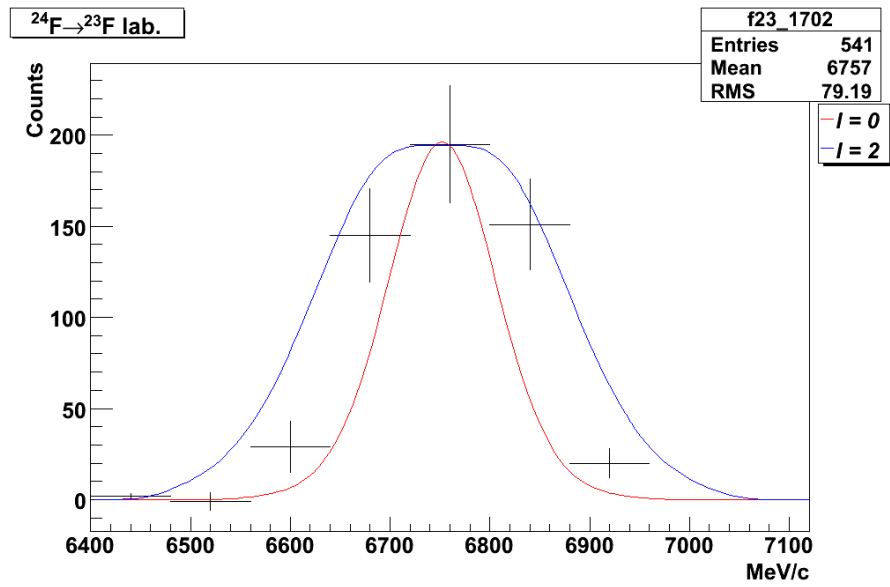


Figure 4.14: ^{23}F 1702(4) keV coincident LMD.

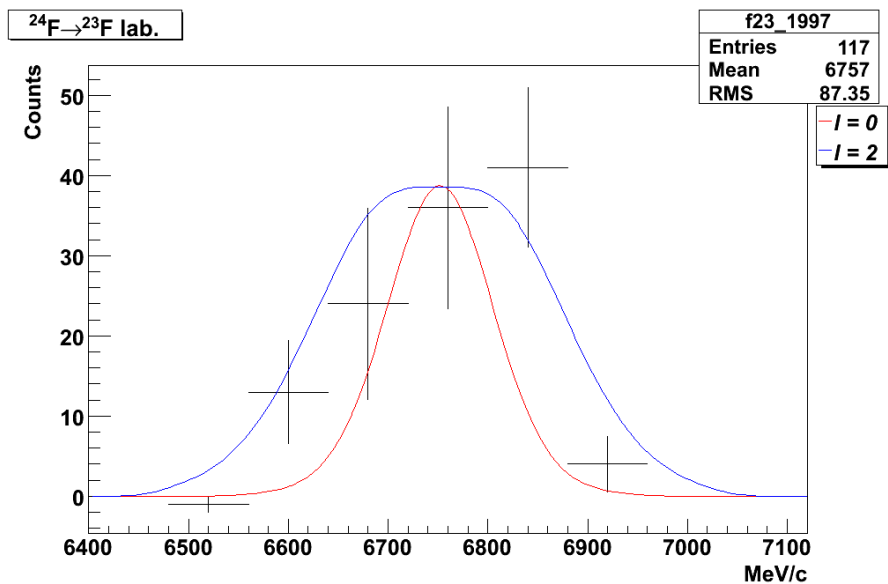


Figure 4.15: ^{23}F 1997(5) keV coincident LMD.

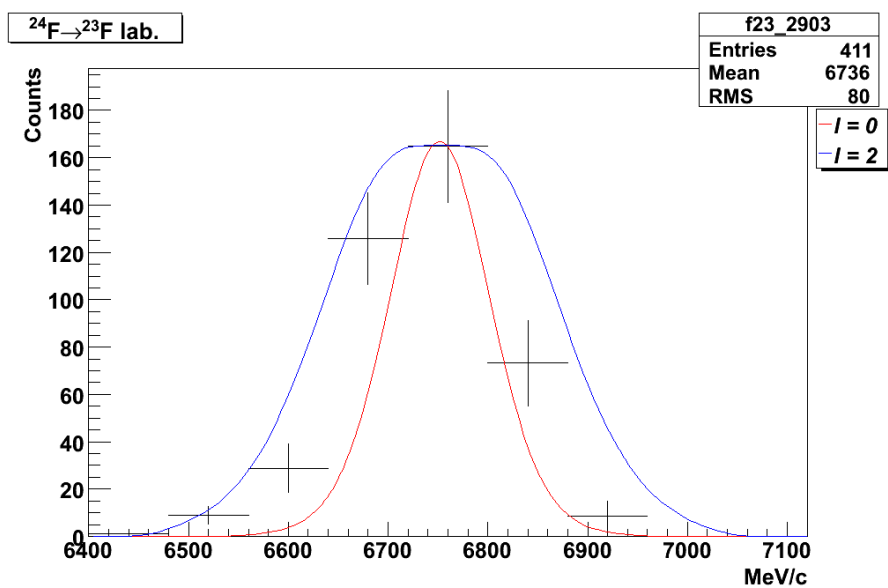


Figure 4.16: ^{23}F 2903(4) keV coincident LMD.

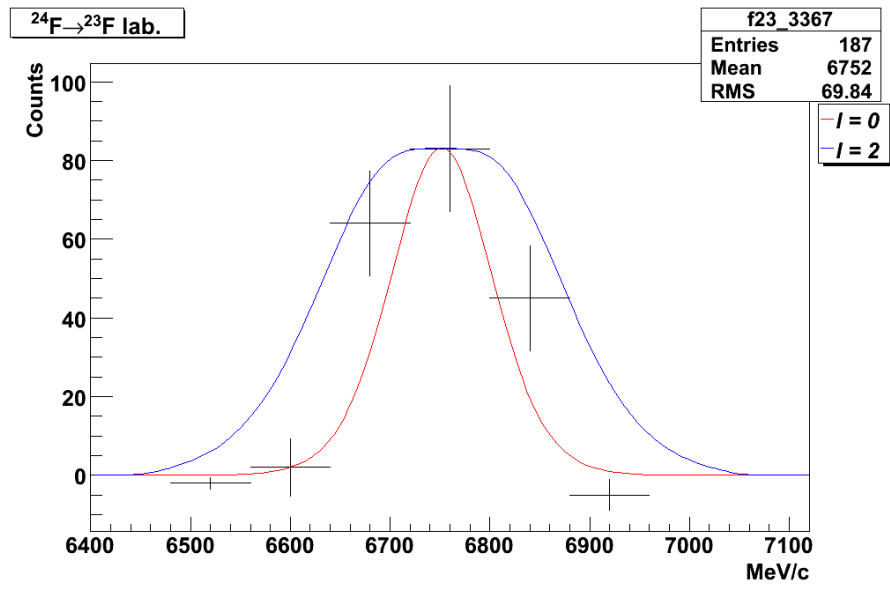


Figure 4.17: ^{23}F 3367(6) keV coincident LMD.

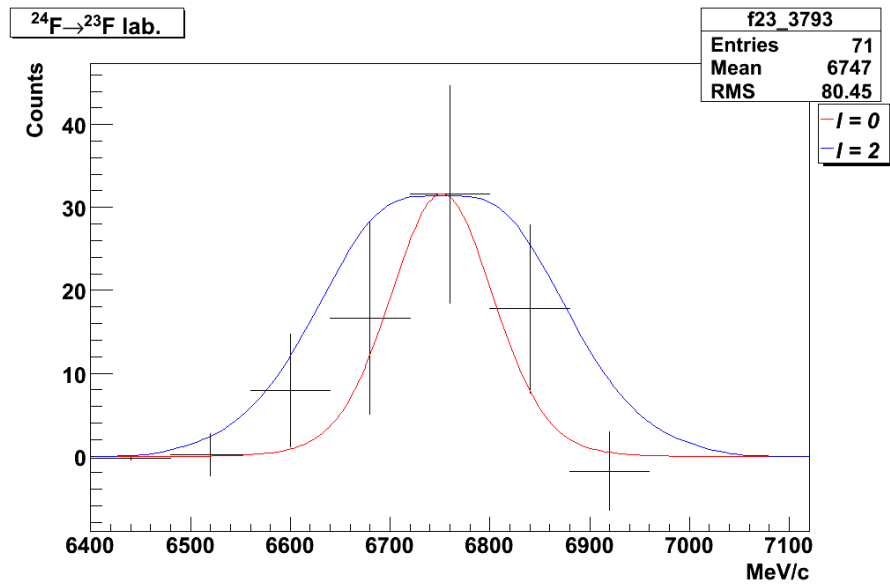


Figure 4.18: ^{23}F 3793(7) keV coincident LMD.

4.4 $^{25}\text{F} \rightarrow ^{24}\text{F}$

4.4.1 Discussion

The structures of ^{24}F and ^{25}F are not well known. A previous experiment [51] observed β -decay from ^{24}O and identified the ground state and two excited states in ^{24}F , assigned parities: ground state $(1,2,3^+)$, 521.5(0.3) keV $(1,2,3^+)$ and 1831.3(0.5)(1^+). The ground state was predicted to be 3^+ by Sauvan, et al [55]. Shown in Fig. 4.19 is the level scheme presented by Reed, et al, compared to shell model calculations using the CW interaction [51].

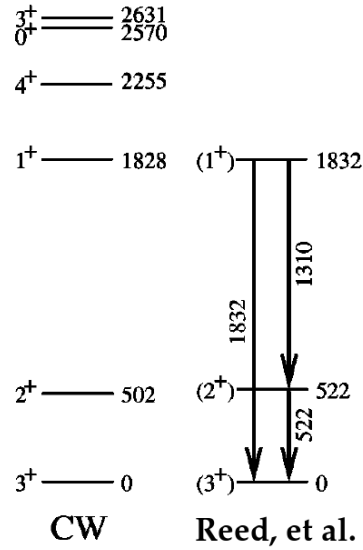
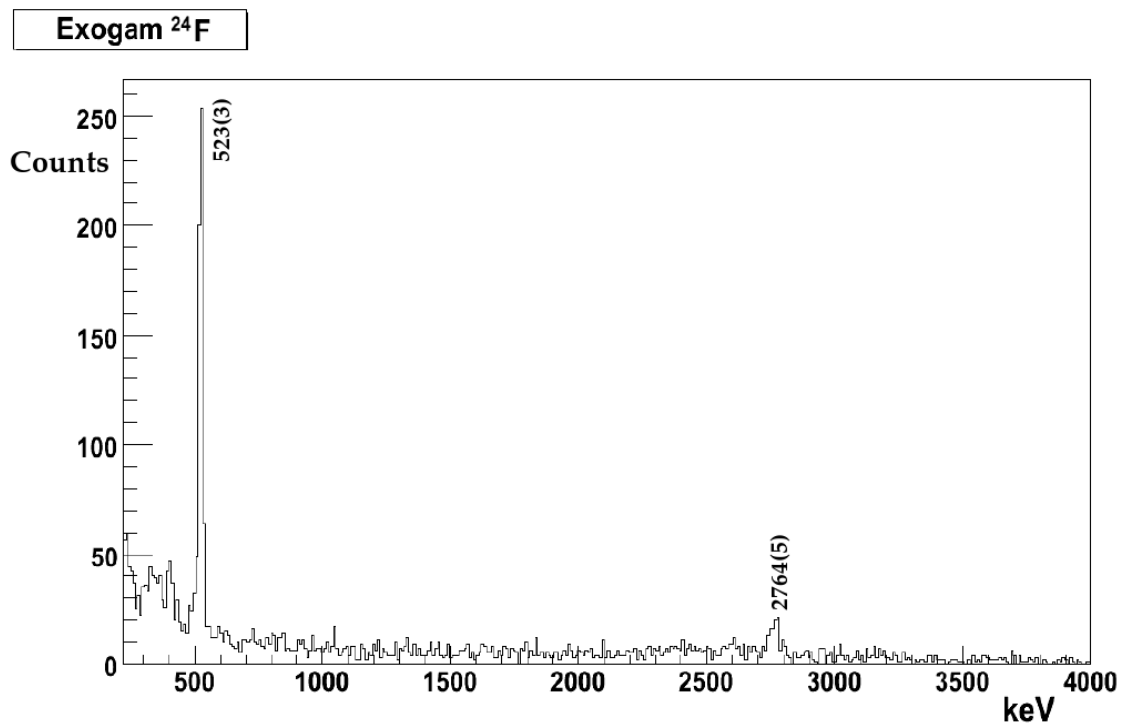
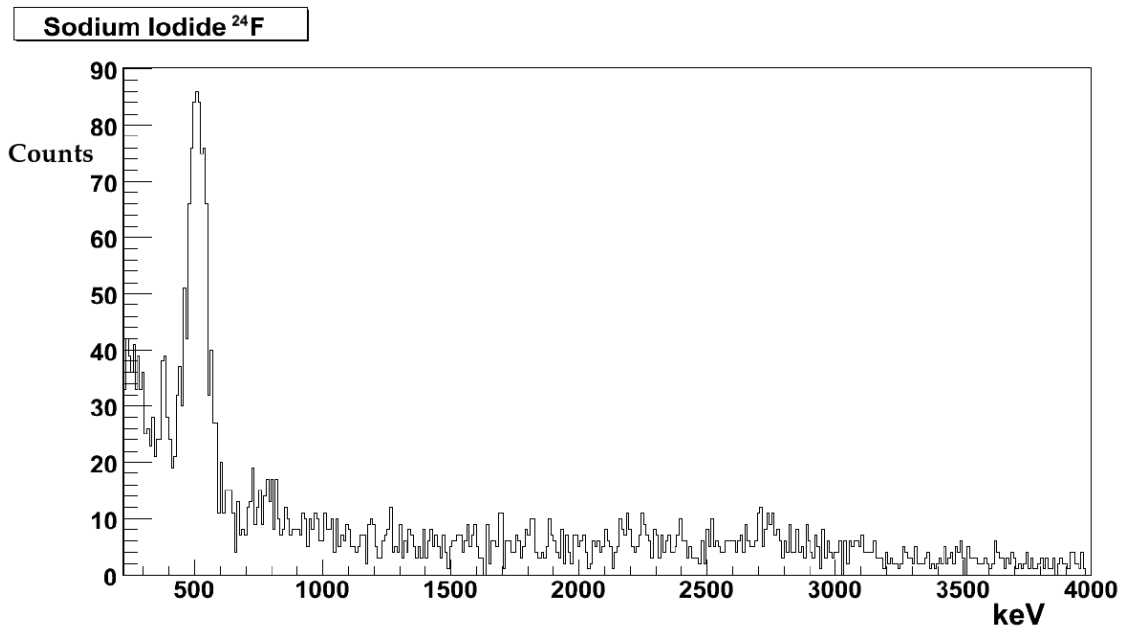


Figure 4.19: Level scheme of ^{24}F compared to shell model calculations, taken from [51].

In Fig. 4.20 are shown the Doppler-corrected γ spectra for the fragment ^{24}F for the EXOGAM and NaI array. Peaks at 523(3) keV and 2764(5) keV were observed, this being the first observation of the 2764(5) keV transition.



(a) ^{24}F EXOGAM.



(b) ^{24}F NaI.

Figure 4.20: ^{24}F γ spectra for the EXOGAM and NaI arrays.

The previously observed transitions [51] not seen in this experiment can be explained by the different reaction channels. For β -decay from ^{24}O (with a ground state of 0^+ [30]) β -decay selection rules [63] mean that ^{24}F would be dominantly populated in the 0^+ and 1^+ states. A low population of the 0^+ and 1^+ states is predicted for the one-neutron removal reaction (see Table 4.8).

In order to determine likely candidates for the observed states it is useful to examine the theoretical predictions for ^{24}F . Fig. 4.21 displays the different predicted energy levels using the USD, USDA and USDB interactions, along with observed transitions (right of figure). Again, the USDB interaction seems to predict state energies that match the experimental values more closely.

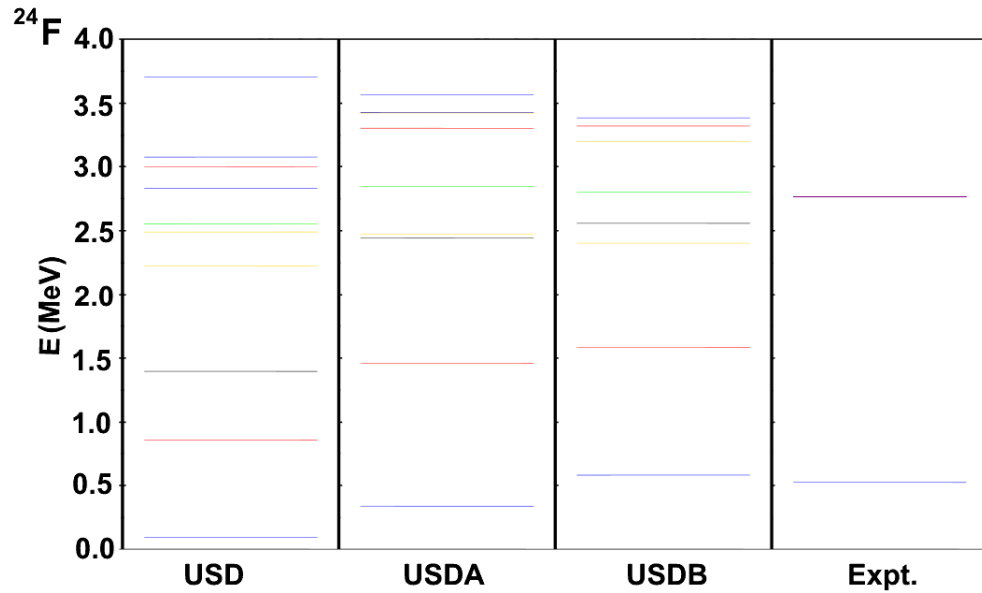


Figure 4.21: ^{24}F Shell-model predicted levels. The colour coding is as follows; 0^+ – black, 1^+ – red, 2^+ – blue, 3^+ – green, 4^+ – gold, unassigned – purple.

All states below the neutron separation energy ($S_n = 3.84$ MeV) calculated using the USD interaction are shown in Table 4.8. The predicted exclusive cross sections for each state, σ_{state} , can be examined to provide candidates for state assignment.

Table 4.8: Predicted Occupancies for $^{25}\text{F} \rightarrow ^{24}\text{F}$ using the USD interaction.

E_{level} (MeV)	I^π	$C^2S_{2s_{1/2}}$	$C^2S_{1d_{3/2}}$	$C^2S_{1d_{5/2}}$	$\sigma_{2s_{1/2}}$ (mb)	$\sigma_{1d_{3/2}}$ (mb)	$\sigma_{1d_{5/2}}$ (mb)	σ_{state} (mb)
0.000	3_1^+	0.822	0.001	0.077	35.98	0.06	1.77	37.80
0.097	2_1^+	0.641	0.011	0.031	27.63	0.45	0.71	28.79
0.861	1_1^+	-	0.062	0.014	-	2.56	0.32	2.88
1.396	0_1^+	-	-	0.042	-	-	0.93	0.93
2.223	4_1^+	-	0.004	0.997	-	0.17	21.75	21.93
2.490	4_2^+	-	0.111	0.346	-	4.49	7.52	12.01
2.554	3_2^+	0.009	0.000	0.694	0.27	0.02	15.05	15.34
2.828	2_2^+	0.013	0.019	0.179	0.41	0.76	3.86	5.03
2.996	1_2^+	-	0.011	0.089	-	0.46	1.92	2.37
3.074	2_3^+	0.002	0.005	0.133	0.07	0.20	2.86	3.12
3.704	2_4^+	0.022	0.013	0.323	0.63	0.47	6.91	8.01
SUM ($\sigma_{\text{theo.}}$)					64.98	9.64	63.60	138.22

4.4.2 Exclusive One-Neutron Removal Cross Sections

As shown in Fig 4.19, only the $\sim 523(3)$ keV peak has been previously observed [51]. $\gamma\gamma$ coincidences did not reveal any cascades, though this is inconclusive due to low statistics. The transitions have been taken as decaying to the ground state, making the assumption that there is no feeding present to account for.

Table 4.9: $^{25}\text{F} \rightarrow ^{24}\text{F}$ Exclusive Experimental Cross Sections.

E_{level} (keV)	b (%)	σ_{ex} (mb)
0.	64.25(1.32)	77.55(4.77)
523(3)	25.65(0.29)	30.96(3.38)
2764(5)	8.10(1.27)	9.78(3.36)
Experimental $\sigma_{inc} = 120.70(10.76)\text{mb}$		

It must also be noted that considerations such as state lifetimes, γ -ray intensity, detector threshold settings, mean that it is likely that some transitions have not been observed. For this reason the cross section to the ground state is likely to be smaller than the value displayed in Table 4.9.

4.4.3 Longitudinal Momentum Distributions

The inclusive and exclusive measured LMDs are presented in Figs. 4.22 – 4.25. The ^{24}F exclusive LMDs give good information about the configuration of the γ -coincident

states. The inclusive distribution (Fig. 4.22) is a combination of the ground and all populated excited states and appears to have a dominant s-wave contribution, where shell-model predictions predict equal s-wave and d-wave components (see Table 4.8). The ground state LMD (Fig. 4.23) also indicates a dominant s-wave component. The 523(3) keV gated LMD (Fig. 4.24) seems to be purely s-wave. This is in contrast to the 2764(5) keV gated LMD (Fig. 4.25), which seems to indicate a stronger d-wave component.

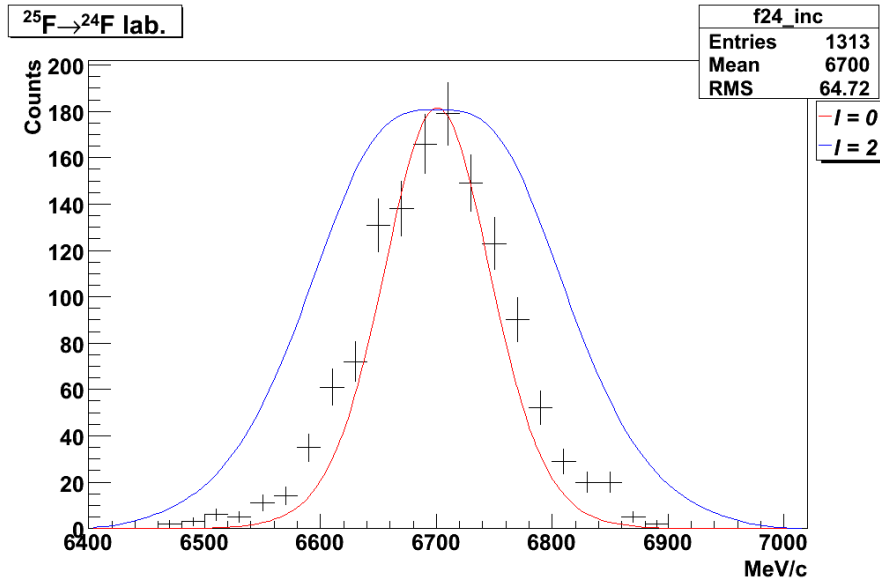


Figure 4.22: ^{24}F Inclusive LMD.

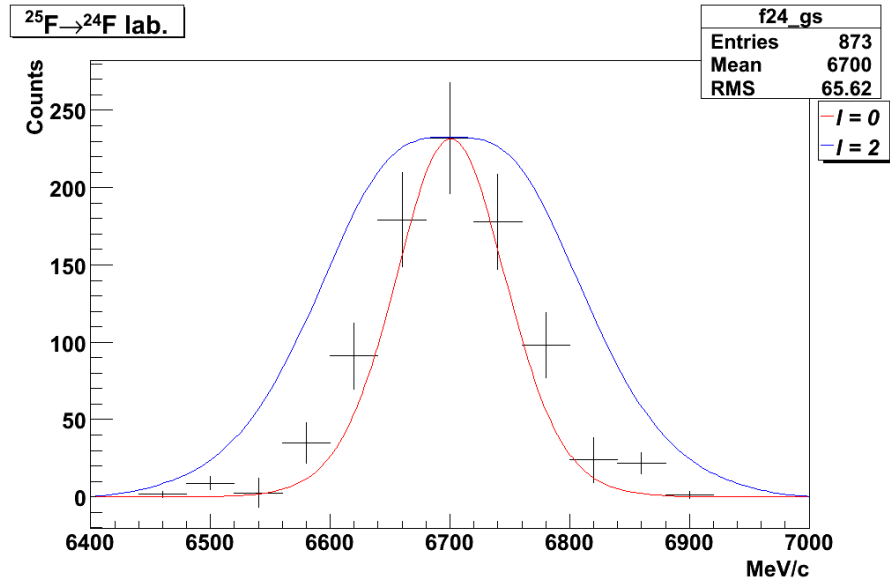


Figure 4.23: ^{24}F ground state LMD.

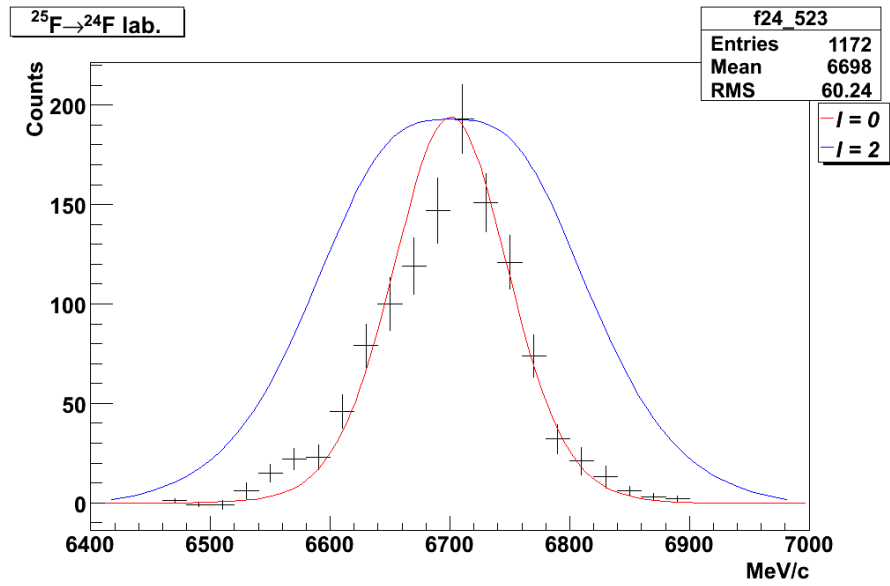


Figure 4.24: ^{24}F 523(3) keV coincident LMD.

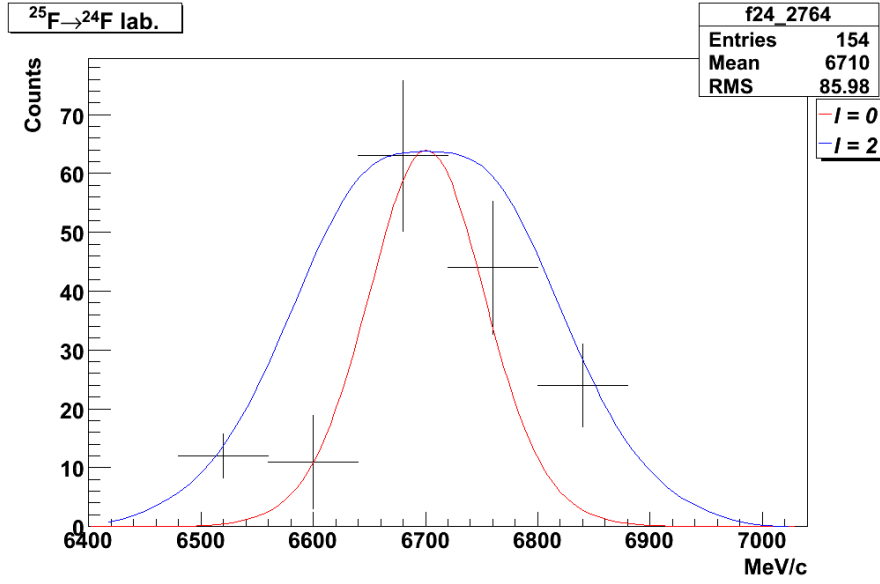


Figure 4.25: ^{24}F 2764(5) keV coincident LMD.

The predictions of a 3^+ ground state for ^{24}F [56] seem to be supported by the strong contribution from s-wave in the eikonal predicted LMDs (Fig. 4.23). The 2_1^+ seems a likely candidate for the 523(3) keV state, being as it is the only other state with a significant $2s_{1/2}$ predicted occupancy. Of the interactions used in Fig. 4.21, the one that best matches the 523(3) keV observed transition with the 2_1^+ is the USDB interaction, with a predicted energy of 580 keV (see Fig. 4.21). On the strength of the predicted occupancies [15] and LMD comparisons with eikonal predictions, the 523(3) keV state observed in the experiment has been labelled blue (for 2^+). The higher energy state at 2764(5) keV has been labelled purple, for unassigned. The high C^2S values for the 3_2^+ , 4_1^+ and 4_2^+ states mean that they are candidates for the state which decays via the 2764(5) keV transition. The USDB interaction predicts a 3_2^+ energy of 2802 keV, the Chung and Wildenthal (CW) effective interaction [51] predicts

a 3_2^+ energy of 2631 keV. The CW interaction was found to be in good agreement with low-lying states in ^{24}F (see Fig. 4.19).

It could be expected to observe peaks at a similar energy for the other states. There is another possibility – that the 2764(5) keV transition is an unresolved doublet of two states. A Monte Carlo simulation was performed to investigate this possibility. Fig. 4.26 shows this simulation. Both the data (black) and the Geant4 simulation (red) are shown, both independently background subtracted. The simulation did not account for $\Delta\beta$ due to energy straggling in the target and the Δp_z of the incoming beam, resulting in the FWHM being underestimated to some extent.

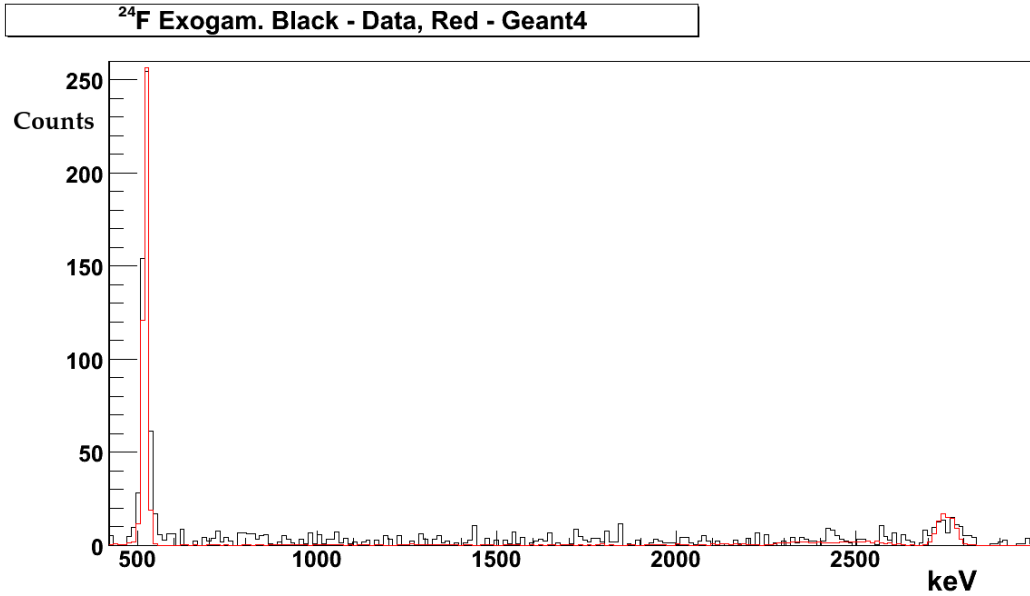


Figure 4.26: ^{24}F EXOGAM Geant4 – data comparison.

The resolution of a single simulated peak yields a similar energy resolution to the observed transition – which suggests that the peak is in fact a single transition.

A possible transition not previously observed may be seen at 403(6) keV, which suffers from low statistics. Although observed in both the EXOGAM and NaI arrays (see Fig. 4.20) there are factors which cast doubt upon it being a real transition. A Gaussian fit of the 403 keV peak seen in the NaI array gives a full-width-half-maximum value of ~ 30 keV, which is significantly smaller than expected. There are also no obvious candidates for the 403(6) keV transition in shell-model predictions.

4.4.4 Experimental Spectroscopic Factors

For the 523(3) keV transition we find a very good agreement in energy for the 2_1^+ state using the USDB interaction. This interaction was thus employed to extract theoretical C^2S values for the 2_1^+ state. Both shell-model predictions and the exclusive LMD reflect an almost pure $2s_{1/2}$ occupancy for this state. By assuming no d-wave contribution we may extract an experimental C^2S , which may be compared with theory. In Table 4.10 the USDB interaction is employed in a $sdpn$ model space to predict spectroscopic factors for the considered subshells for the 2_1^+ state.

Eikonal theory using $E_S = 523$ keV (see Eq. 3.18) gives (unit) single particle cross sections, σ_{sp} , for each subshell. The experimentally calculated exclusive cross section is 30.96(48) mb for the 523 keV transition (see Table 4.9). This is divided by the $2s_{1/2}$ single particle cross section (41.49 mb) to yield an experimental spectroscopic factor, C^2S_{expt} . This value may be compared to $C^2S_{USDB-com}$, which are the USDB C^2S values following the centre-of-mass correction described in Eq. 3.17. The experimental results are in excellent agreement with theory.

Table 4.10: $^{25}\text{F} \rightarrow ^{24}\text{F}$ Experimental Spectroscopic Factors

2_1^+ 523 keV	$2s_{1/2}$	$1d_{3/2}$	$1d_{5/2}$
C^2S_{expt}	0.746(81)	-	-
$C^2S_{USDB-com}$	0.743	0.012	0.037
C^2S_{USDB}	0.685	0.011	0.034
RMS radii (fm)	3.962	3.548	3.568
σ_{sp} (mb)	41.49	24.23	24.60
$\sigma_{theo.}$ (mb)	30.83	0.29	0.90

In conclusion, the ground state LMD of ^{24}F has been measured and was found to agree well with eikonal predictions for $2s_{1/2}$ occupancy. This supports the ground state assignment of 3^+ [55] in consideration of the shell-model predicted occupancy for that state.

The previously observed 523(3) keV transition [51] has been confidently assigned as the first 2^+ state on the basis that the LMD associated with that state exhibits almost pure $2s_{1/2}$ occupancy, the 2_1^+ state being the only excited state that shell model calculations predict to do so. In addition experimental C^2S values have been calculated for the assigned 2_1^+ state and are found to be in excellent agreement with theoretical USDB predictions.

A new transition at 2764(5) keV has been identified and has been speculatively assigned as the 3_2^+ , with the 4_1^+ and 4_2^+ states as other possible candidates.

4.5 $^{26}\text{F} \rightarrow ^{25}\text{F}$

4.5.1 Discussion

Previous work has identified transitions at 750, 1700, 3300 and 3700 keV in ^{25}F [6], see Fig. 4.27. In this work there were insufficient γ ray statistics for peak identification, but there is a suggestion of transitions at 1720(17) keV and 3270(24) keV in the Doppler-corrected spectra shown in Fig. 4.28. The previously observed 3300 keV has been assigned as the $9/2_1^+ \rightarrow 5/2_1^+$ (ground state) transition [6]. This assignment could not be correct for the (potential) 3270(67) keV peak as the $9/2_1^+$ state is not populated by the reaction channel employed in this experiment. It has been suggested that the 1700 keV transition may terminate at the $7/2_1^+$ level [6], though this would mean a bound state existed at ~ 5 MeV, higher than the current value for the neutron separation energy, 4.35 MeV. As the neutron separation energy was derived from mass measurement calculations, rather than a direct measurement, this is entirely possible. The energies of the ^{25}F states thought to be the $9/2_1^+$ and $7/2_1^+$ are presumed to be an estimate of the (as then) unmeasured 2_1^+ state in ^{24}O as between 3300 and 3700 keV. This has since been observed as a 4.7 MeV resonance via one proton removal from ^{26}F at the NSCL at MSU [30].

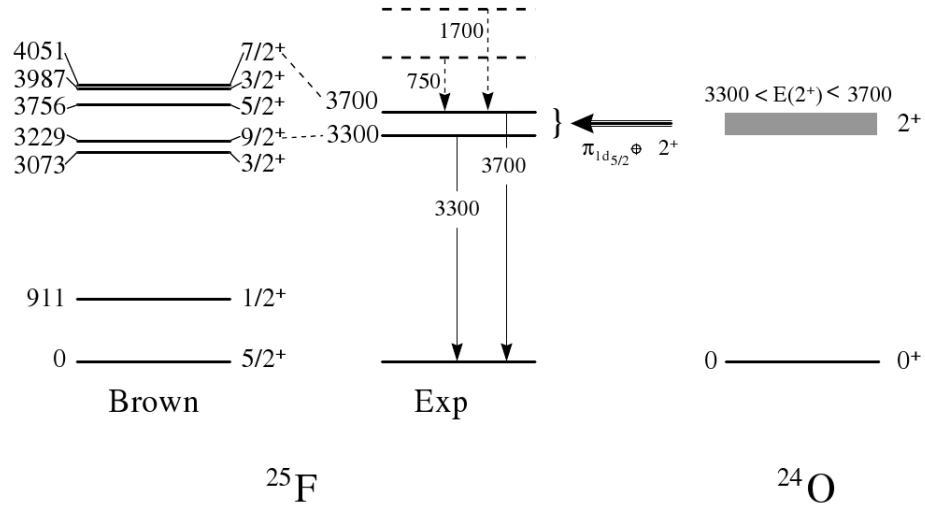
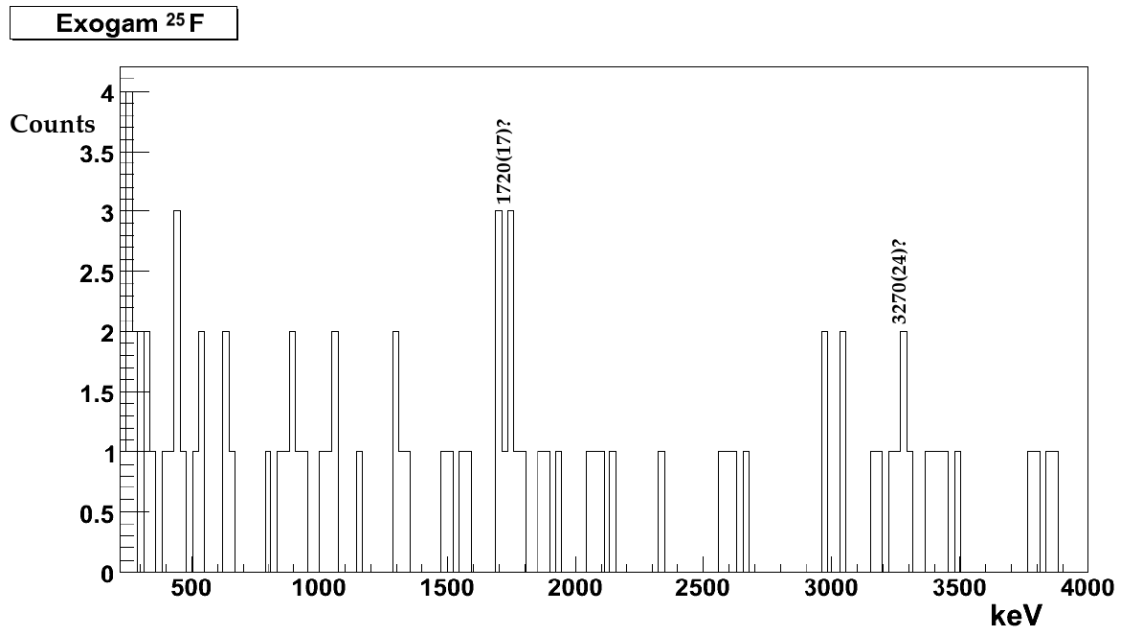
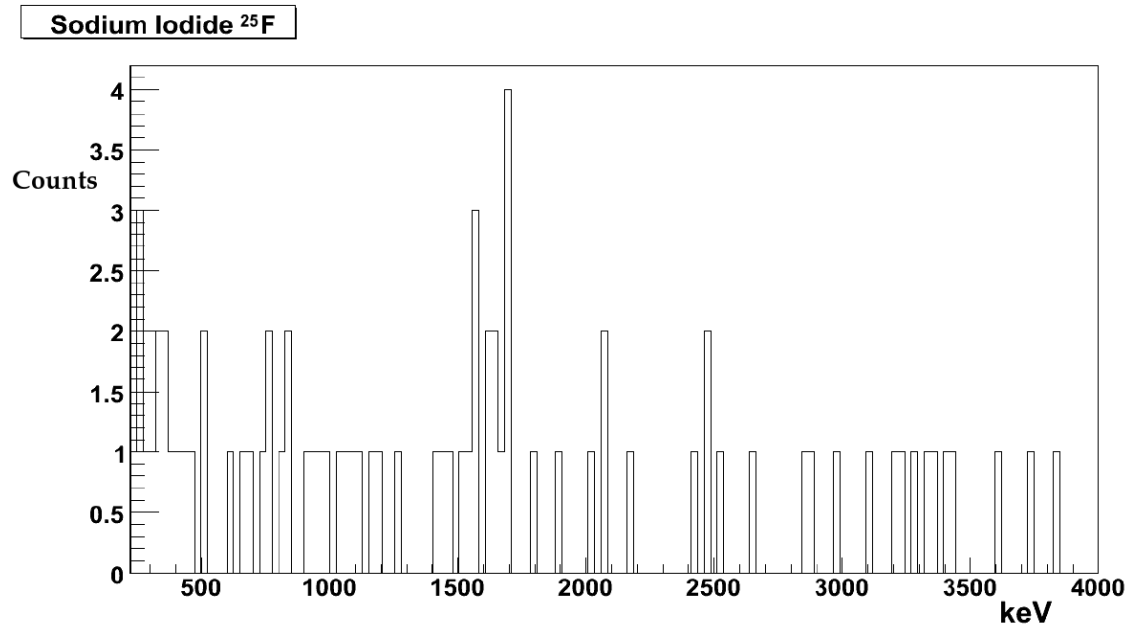


Figure 4.27: Level schemes of ^{25}F from previous experiment (middle) and shell model calculations including only the sd neutron valence space (left). A suggestion of what would be the level scheme of ^{24}O is indicated (right). Taken from [6].

A $^1\text{H}(^{27}\text{F}, ^{25}\text{F})$ reaction experiment at RIKEN [24] observed a 727(22) keV and 1753(53) keV transitions, and suggested that the 727(22) keV γ ray could correspond to the $1/2_1^+ \rightarrow 5/2_1^+$ (ground state) transition, if the considered model space was extended from sd to $sdpf$. This was taken as an indication of the breakdown of the $N = 20$ neutron shell closure [75]. No transition candidate was apparent in shell model calculations for the 1753(53) keV transition.



(a) ^{25}F EXOGAM.



(b) ^{25}F NaI.

Figure 4.28: ^{25}F γ spectra for the EXOGAM and NaI arrays.

Comparisons with shell model calculations can be made with a view to predicting all possible states associated with the transition. All levels below the neutron separation energy for the USD interaction are shown in Table 4.11. Table 4.11 shows the spectroscopic factors for each state, accompanied by the predicted exclusive cross sections calculated via eikonal theory. The theoretical inclusive cross section is simply the summation of the theoretical exclusive cross sections to all bound states.

Table 4.11: Predicted occupancies for $^{26}\text{F} \rightarrow ^{25}\text{F}$ using the USD interaction.

E_{level} (MeV)	I^π	$C^2S_{2s_{1/2}}$	$C^2S_{1d_{3/2}}$	$C^2S_{1d_{5/2}}$	$\sigma_{2s_{1/2}}$ (mb)	$\sigma_{1d_{3/2}}$ (mb)	$\sigma_{1d_{5/2}}$ (mb)	σ_{state} (mb)
0.000	$5/2_1^+$	-	0.801	0.033	-	49.69	2.18	51.87
0.911	$1/2_1^+$	0.205	0.011	-	20.44	0.58	-	21.02
3.072	$3/2_1^+$	0.891	0.004	0.010	54.75	0.14	0.41	55.30
3.229	$9/2_1^+$	-	-	-	-	-	-	0.00
3.756	$5/2_2^+$	-	0.014	0.114	-	0.50	4.20	4.70
3.987	$3/2_2^+$	0.016	0.006	0.161	0.85	0.21	5.83	6.89
4.052	$7/2_1^+$	-	-	0.013	-	-	0.46	0.46
4.069	$1/2_2^+$	0.292	0.008	-	16.91	0.30	-	17.21
SUM ($\sigma_{\text{theo.}}$)					92.95	51.42	13.08	157.45

4.5.2 Longitudinal Momentum Distributions

As no transitions could be confidently identified in the $^{26}\text{F} \rightarrow ^{25}\text{F} \gamma$ spectra, exclusive cross sections and momentum distributions were not extracted. Shown in Fig. 4.29 is the inclusive longitudinal momentum distribution for ^{25}F , overlayed with theoretical predictions assuming ground state occupancy. See Fig. 4.29. As predicted by USD shell model calculations (see Table 4.11), the inclusive distribution seems to be a combination of both s-wave and d-wave occupancy.

Though for the experiment presented in this thesis there proved insufficient ^{25}F fragments for detailed analysis, the poor agreement of previously observed transitions to shell-model predictions may indicate that there is some occupancy of fp subshells not considered in the sd model space. Additionally there may be some effects that are not considered in the models, for example simultaneous, correlated proton-neutron cross shell excitations may play a significant role [24].

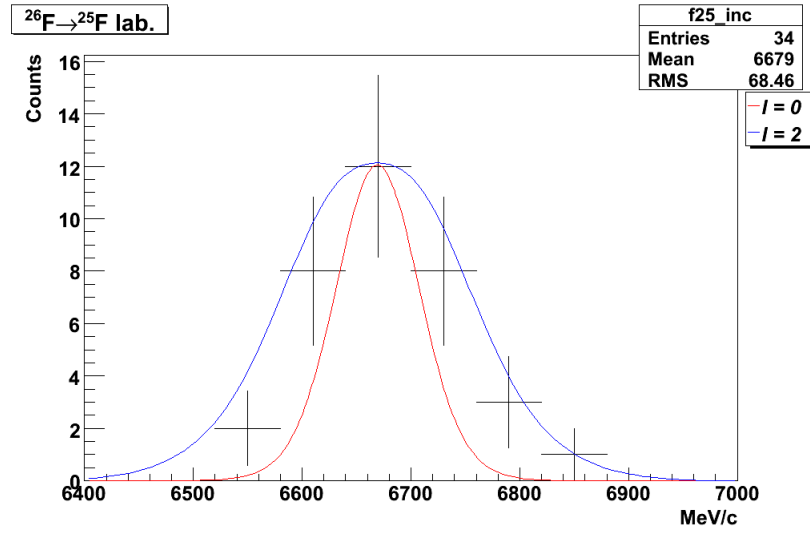


Figure 4.29: Inclusive LMD of ^{25}F , overlayed with eikonal $l = 0$ and $l = 2$ predictions.

Summary

Individual states in ^{25}F , ^{24}F , ^{23}F and ^{22}O have been populated from one-neutron removal reactions using radioactive beams of ^{26}F , ^{25}F , ^{24}F and ^{23}O at ~ 50 A.MeV. Cross sections have been determined for each fragment, including where possible exclusive measurements to separate states. The cross sections have been compared with those calculated from eikonal reaction theory [74]. Eikonal theory was also employed to give longitudinal momentum distribution predictions for each state, which were compared to experimentally observed distributions, providing information on the subshell occupancy of the state. Shell-model calculations [15] were employed to give both predictions of the energy of states and theoretical spectroscopic factors. The predictions of the USD, USDA and USDB interactions [14] were also compared to experimental results.

For $^{23}\text{O} \rightarrow ^{22}\text{O}$, two transitions were observed at 1382(7) and 3195(9) keV, associated with two known excited states. The inclusive LMD of ^{22}O is predicted to have a greater d-wave contribution by shell-model calculations than is observed experimentally. This does however agree with results employing a similar technique [35].

For $^{24}\text{F} \rightarrow ^{23}\text{F}$, seven transitions were observed at 625(4), 916(4), 1702(4), 1997(5), 2903(4), 3367(6) and 3793(7) keV, associated with five known excited states. Where statistics allowed, γ - γ coincidence data was taken, the results agreeing well with previous level schemes. An excellent agreement with theoretical predictions of a 3^+ ground state were found, with the g.s. longitudinal momentum distribution in excellent agreement with the eikonal prediction for near-pure s-wave occupancy. Similar agreement was found for excited states, for example the 916 keV transition from the $9/2_1^+$ state LMD giving good agreement with the eikonal prediction for a pure d-wave occupancy.

For $^{25}\text{F} \rightarrow ^{24}\text{F}$, two excited states were observed at 523(3) keV and 2764(5) keV. The state associated with the previously observed 523 keV transition [51] was unambiguously assigned as the 2_1^+ state. An experimental spectroscopic factor was extracted for this state, and found to be in excellent agreement with theoretical predictions. The transition at 2.76 MeV was observed for the first time and speculatively assigned as either the 3_2^+ , 4_1^+ or 4_2^+ states.

For $^{26}\text{F} \rightarrow ^{25}\text{F}$, eikonal predictions for the inclusive LMD show a mixed contribution of s-wave and d-wave occupancy, in agreement with shell-model predictions.

References

- [1] S. Agostinelli, J. Allison, K. Amako, J. Apostolakis, H. Araujo, P. Arce, M. Asai, D. Axen, S. Banerjee, G. Barrand, F. Behner, L. Bellagamba, J. Boudreau, L. Broglia, A. Brunengo, H. Burkhardt, S. Chauvie, J. Chuma, R. Chytrcek, G. Cooperman, G. Cosmo, P. Degtyarenko, A. Dell’Acqua, G. Depaola, D. Dietrich, R. Enami, A. Feliciello, C. Ferguson, H. Fesefeldt, G. Folger, F. Foppiano, A. Forti, S. Garelli, S. Giani, R. Giannitrapani, D. Gibin, J. J. G. Cadenas, I. Gonzalez, G. G. Abril, G. Greeniaus, W. Greiner, V. Grichine, A. Grossheim, S. Guatelli, P. Gumplinger, R. Hamatsu, K. Hashimoto, H. Hasui, A. Heikkinen, A. Howard, V. Ivanchenko, A. Johnson, F. W. Jones, J. Kallenbach, N. Kanaya, M. Kawabata, Y. Kawabata, M. Kawaguti, S. Kelner, P. Kent, A. Kimura, T. Kodama, R. Kokoulin, M. Kossov, H. Kurashige, E. Lamanna, T. Lampn, V. Lara, V. Lefebure, F. Lei, M. Liendl, W. Lockman, F. Longo, S. Magni, M. Maire, E. Medernach, K. Minamimoto, P. M. de Freitas, Y. Morita, K. Murakami, M. Nagamatsu, R. Nartallo, P. Nieminen, T. Nishimura, K. Ohtsubo, M. Okamura, S. O’Neale, Y. Oohata, K. Paech, J. Perl, A. Pfeiffer, M. G. Pia, F. Ranjard, A. Rybin, S. Sadilov, E. D. Salvo, G. Santin, T. Sasaki, N. Savvas, Y. Sawada,

- S. Scherer, S. Sei, V. Sirotenko, D. Smith, N. Starkov, H. Stoecker, J. Sulkimo, M. Takahata, S. Tanaka, E. Tcherniaev, E. S. Tehrani, M. Tropeano, P. Truscott, H. Uno, L. Urban, P. Urban, M. Verderi, A. Walkden, W. Wander, H. Weber, J. P. Wellisch, T. Wenaus, D. C. Williams, D. Wright, T. Yamada, H. Yoshida, and D. Zschesche. G4—a simulation toolkit. *Nuclear Instruments and Methods in Physics Research Section A: Accelerators, Spectrometers, Detectors and Associated Equipment*, 506(3):250 – 303, 2003.
- [2] B. Alex Brown. New skyrme interaction for normal and exotic nuclei. *Phys. Rev. C*, 58(1):220–231, 1998.
- [3] R. Anne. SISSI at GANIL. *Nuclear Instruments and Methods in Physics Research Section B: Beam Interactions with Materials and Atoms*, 126(1-4):279 – 283, 1997. International Conference on Electromagnetic Isotope Separators and Techniques Related to Their Applications.
- [4] T. Aumann, A. Navin, D. P. Balamuth, D. Bazin, B. Blank, B. A. Brown, J. E. Bush, J. A. Caggiano, B. Davids, T. Glasmacher, V. Guimarães, P. G. Hansen, R. W. Ibbotson, D. Karnes, J. J. Kolata, V. Maddalena, B. Pritychenko, H. Scheit, B. M. Sherrill, and J. A. Tostevin. One-neutron knockout from individual single-particle states of ^{11}B . *Phys. Rev. Lett.*, 84(1):35–38, 2000.
- [5] F. Azaiez. EXOGAM: a γ -ray spectrometer for radioactive beams. *Nuclear Physics A*, 654(1):1003c – 1008c, 1999.

- [6] F. Azaiez, M. Belleguic, D. Sohler, M. Stanoiu, Z. Dombrdi, O. Sorlin, J. Timr, F. Amorini, D. Baiborodin, A. Bauchet, F. Becker, C. Borcea, C. Bourgeois, Z. Dlouhy, C. Donzaud, J. Duprat, D. Guillemaud-Mueller, F. Ibrahim, M. Lopez, R. Lucas, S. Lukyanov, V. Maslov, J. Mrazek, C. Moore, F. Nowacki, B. Nyak, Y.-E. Penionzhkevich, M. Saint-Laurent, F. Sarazin, J. Scarpaci, G. Sletten, C. Stodel, M. Taylor, C. Theisen, and G. Voltolini. Probing shell structure in neutron-rich nuclei with in-beam γ -spectroscopy. *The European Physical Journal A - Hadrons and Nuclei*, 15:93–97, 2002.
- [7] D. Bazin, W. Benenson, B. A. Brown, J. Brown, B. Davids, M. Fauerbach, P. G. Hansen, P. Mantica, D. J. Morrissey, C. F. Powell, B. M. Sherrill, and M. Steiner. Probing the halo structure of $^{19,17,15}\text{C}$ and ^{14}B . *Phys. Rev. C*, 57(5):2156–2164, 1998.
- [8] E. Becheva, Y. Blumenfeld, E. Khan, D. Beaumel, J. M. Daugas, F. Delaunay, C.-E. Demonchy, A. Drouart, M. Fallot, A. Gillibert, L. Giot, M. Grasso, N. Keeley, K. W. Kemper, D. T. Khoa, V. Lapoux, V. Lima, A. Musumarra, L. Nalpas, E. C. Pollacco, O. Roig, P. Roussel-Chomaz, J. E. Sauvestre, J. A. Scarpaci, F. Skaza, and H. S. Than. $N = 14$ shell closure in ^{22}O viewed through a neutron sensitive probe. *Physical Review Letters*, 96(1):012501, 2006.
- [9] M. Belleguic, F. Azaiez, Z. Dombrádi, D. Sohler, M. J. Lopez-Jimenez, T. Otsuka, M. G. Saint-Laurent, O. Sorlin, M. Stanoiu, Y. Utsuno, Y.-E. Penionzhkevich, N. L. Achouri, J. C. Angelique, C. Borcea, C. Bourgeois, J. M. Daugas, F. D. Oliveira-Santos, Z. Dlouhy, C. Donzaud, J. Duprat, Z. Elekes, S. Grévy,

- D. Guillemaud-Mueller, S. Leenhardt, M. Lewitowicz, S. M. Lukyanov, and W. Mittig. Search for neutron excitations across the $N = 20$ shell gap in $^{25-29}\text{Ne}$. *Phys. Rev. C*, 72(5):054316, 2005.
- [10] L. Bianchi, B. Fernandez, J. Gastebois, A. Gillibert, W. Mittig, and J. Barrette. SPEG: An energy loss spectrometer for GANIL. *Nuclear Instruments and Methods in Physics Research A*, 276(1):509–520, 2002.
- [11] A. Bonaccorso and D. M. Brink. Stripping to the continuum of ^{208}Pb . *Phys. Rev. C*, 44(4):1559–1568, 1991.
- [12] B. A. Brown. The nuclear shell model towards the drip lines. *Progress in Particle and Nuclear Physics*, 47(2):517 – 599, 2001.
- [13] B. A. Brown, P. G. Hansen, and J. A. Tostevin. Comment on ”experimental evidence of core modification in the near drip-line nucleus ^{23}O ”. *Phys. Rev. Lett.*, 90(15):159201, 2003.
- [14] B. A. Brown and W. A. Richter. New USD Hamiltonians for the sd shell. *Physical Review C (Nuclear Physics)*, 74(3):034315, 2006.
- [15] B. A. Brown, et al. Oxbash for windows. MSU-NSCL Report 1289.
- [16] X. Campi, H. Flocard, A. K. Kerman, and S. Koonin. Shape transition in the neutron rich sodium isotopes. *Nuclear Physics A*, 251(2):193 – 205, 1975.
- [17] D. Cortina-Gil, J. Fernandez-Vazquez, F. Attallah, T. Baumann, J. Benlliure, M. J. G. Borge, L. Chulkov, C. Forssn, L. M. Fraile, H. Geissel, J. Gerl, K. Itahashi,

- R. Janik, B. Jonson, S. Karlsson, H. Lenske, S. Mandal, K. Markenroth, M. Meister, M. Mocko, G. Münzenberg, T. Ohtsubo, A. Ozawa, Y. Parfenova, V. Pribora, A. Richter, K. Riisager, R. Schneider, H. Scheit, G. Schrieder, N. Shulgina, H. Simon, B. Sitar, A. Stolz, P. Strmen, K. Smmerer, I. Szarka, S. Wan, H. Weick, and M. V. Zhukov. Nuclear and coulomb breakup of ^8B . *Nuclear Physics A*, 720(1-2):3 – 19, 2003.
- [18] D. Cortina-Gil, J. Fernandez-Vazquez, T. Aumann, T. Baumann, J. Benlliure, M. J. G. Borge, L. V. Chulkov, U. Datta Pramanik, C. Forssén, L. M. Fraile, H. Geissel, J. Gerl, F. Hammache, K. Itahashi, R. Janik, B. Jonson, S. Mandal, K. Markenroth, M. Meister, M. Mocko, G. Münzenberg, T. Ohtsubo, A. Ozawa, Y. Prezado, V. Pribora, K. Riisager, and H. Scheit. Shell structure of the near-dripline nucleus ^{23}O . *Phys. Rev. Lett.*, 93(6):062501, 2004.
- [19] M. L. D. Bazin, O. B. Tarasov and O. Sorlin. The program lise: a simulation of fragment separators. *Nuclear Instruments and Methods in Physics Research A*, 482:307 – 327, 2002.
- [20] A. E. L. Dieperink and T. d. Forest. Center-of-mass effects in single-nucleon knock-out reactions. *Phys. Rev. C*, 10(2):543–549, 1974.
- [21] J. Dobaczewski, I. Hamamoto, W. Nazarewicz, and J. A. Sheikh. Nuclear shell structure at particle drip lines. *Phys. Rev. Lett.*, 72(7):981–984, 1994.

- [22] J. Dobaczewski, W. Nazarewicz, T. R. Werner, J. F. Berger, C. R. Chinn, and J. Dechargé. Mean-field description of ground-state properties of drip-line nuclei: Pairing and continuum effects. *Phys. Rev. C*, 53(6):2809–2840, 1996.
- [23] J. Dudek, Z. Szymański, T. Werner, A. Faessler, and C. Lima. Description of the high spin states in ^{146}Gd using the optimized woods-saxon potential. *Phys. Rev. C*, 26(4):1712–1718, 1982.
- [24] Z. Elekes, Z. Dombrdi, A. Saito, N. Aoi, H. Baba, K. Demichi, Z. Flp, J. Gibelin, T. Gomi, H. Hasegawa, N. Imai, M. Ishihara, H. Iwasaki, S. Kanno, S. Kawai, T. Kishida, T. Kubo, K. Kurita, Y. Matsuyama, S. Michimasa, T. Minemura, T. Motobayashi, M. Notani, T. Ohnishi, H. Ong, S. Ota, A. Ozawa, H. Sakai, H. Sakurai, S. Shimoura, E. Takeshita, S. Takeuchi, M. Tamaki, Y. Togano, K. Yamada, Y. Yanagisawa, and K. Yoneda. Bound excited states in ^{27}F . *Physics Letters B*, 599(1-2):17 – 22, 2004.
- [25] M. Fauerbach, D. J. Morrissey, W. Benenson, B. A. Brown, M. Hellström, J. H. Kelley, R. A. Kryger, R. Pfaff, C. F. Powell, and B. M. Sherrill. New search for ^{26}O . *Phys. Rev. C*, 53(2):647–651, 1996.
- [26] W. S. G. Fey, H. Frank and H. Theissen. Nuclear rms charge radii from relative electron. *Zeitschrift fr Physik A Hadrons and Nuclei*, 265(4):401–403, 1973.
- [27] D. Guillemaud-Mueller, J. C. Jacmart, E. Kashy, A. Latimier, A. C. Mueller, F. Pougheon, A. Richard, Y. E. Penionzhkevich, A. G. Artuhk, A. V. Belozyorov, S. M. Lukyanov, R. Anne, P. Bricault, C. Détraz, M. Lewitowicz, Y. Zhang,

- Y. S. Lyutostansky, M. V. Zverev, D. Bazin, and W. D. Schmidt-Ott. Particle stability of the isotopes ^{26}O and ^{32}Ne in the reaction 44 mev/nucleon $^{48}\text{Ca}+\text{Ta}$. *Phys. Rev. C*, 41(3):937–941, 1990.
- [28] P. G. Hansen and J. A. Tostevin. Direct reactions with exotic nuclei. *Annu. Rev. Nucl. Part. Sci.*, 53:219–261, 2003.
- [29] O. Haxel, J. H. D. Jensen, and H. E. Suess. On the ‘magic numbers’ in nuclear structure. *Phys. Rev.*, 75(11):1766, 1949.
- [30] C. Hoffman, T. Baumann, D. Bazin, J. Brown, G. Christian, D. Denby, P. DeYoung, J. Finck, N. Frank, J. Hinnefeld, S. Mosby, W. Peters, W. Rogers, A. Schiller, A. Spyrou, M. Scott, S. Tabor, M. Thoennessen, and P. Voss. Evidence for a doubly magic ^{24}O . *Physics Letters B*, 672(1):17 – 21, 2009.
- [31] W. Horiuchi and Y. Suzuki. ^{22}C : An s-wave two-neutron halo nucleus. *Physical Review C (Nuclear Physics)*, 74(3):034311, 2006.
- [32] A. S. Jensen, K. Riisager, D. V. Fedorov, and E. Garrido. Structure and reactions of quantum halos. *Rev. Mod. Phys.*, 76(1):215–261, 2004.
- [33] R. Kanungo, M. Chiba, N. Iwasa, S. Nishimura, A. Ozawa, C. Samanta, T. Suda, T. Suzuki, T. Yamaguchi, T. Zheng, and I. Tanihata. Experimental evidence of core modification in the near drip-line nucleus ^{23}O . *Phys. Rev. Lett.*, 88(14):142502, 2002.
- [34] R. Kanungo, C. Nociforo, A. Prochazka, T. Aumann, D. Boutin, D. Cortina-Gil, B. Davids, M. Diakaki, F. Farinon, H. Geissel, R. Gernhäuser, J. Gerl, R. Janik,

- B. Jonson, B. Kindler, R. Knöbel, R. Krücken, M. Lantz, H. Lenske, Y. Litvinov, B. Lommel, K. Mahata, P. Maierbeck, A. Musumarra, T. Nilsson, T. Otsuka, C. Perro, C. Scheidenberger, B. Sitar, P. Strmen, B. Sun, I. Szarka, I. Tanihata, Y. Utsuno, H. Weick, and M. Winkler. One-neutron removal measurement reveals ^{24}O as a new doubly magic nucleus. *Physical Review Letters*, 102(15):152501, 2009.
- [35] R. Kharab, R. Kumar, P. Singh, and H. C. Sharma. Structural analysis of ^{23}O through single-neutron stripping reaction. *Communications in Theoretical Physics*, 49(4):1004–1008, 2008.
- [36] K. Lau and J. Pyrlik. Optimization of centroid-finding algorithms for cathode strip chambers. *Nuclear Instruments and Methods in Physics Research Section A: Accelerators, Spectrometers, Detectors and Associated Equipment*, 366(2-3):298 – 309, 1995.
- [37] J. F. Libin. Construction of two multichannel drift chambers for the focal plane of SPEG. *Nouvelles du GANIL* No 67., 2001.
- [38] J. B. Marion and F. C. Young. Graphs and tables. *Nuclear reaction analysis*, 1968.
- [39] M. G. Mayer. On closed shells in nuclei. *Phys. Rev.*, 74(3):235–239, 1948.
- [40] M. G. Mayer. On closed shells in nuclei. ii. *Phys. Rev.*, 75(12):1969–1970, 1949.
- [41] S. Michimasa, S. Shimoura, H. Iwasaki, M. Tamaki, S. Ota, N. Aoi, H. Baba, N. Iwasa, S. Kanno, S. Kubono, K. Kurita, M. Kurokawa, T. Minemura, T. Mo-

- tobayashi, M. Notani, H. Ong, A. Saito, H. Sakurai, E. Takeshita, S. Takeuchi, Y. Yanagisawa, and A. Yoshida. Proton single-particle states in the neutron-rich ^{23}F nucleus. *Physics Letters B*, 638(2-3):146 – 152, 2006.
- [42] A. Navin, D. W. Anthony, T. Aumann, T. Baumann, D. Bazin, Y. Blumenfeld, B. A. Brown, T. Glasmacher, P. G. Hansen, R. W. Ibbotson, P. A. Lofy, V. Madalena, K. Miller, T. Nakamura, B. V. Pritychenko, B. M. Sherrill, E. Spears, M. Steiner, J. A. Tostevin, J. Yurkon, and A. Wagner. Direct evidence for the breakdown of the $N = 8$ shell closure in ^{12}B . *Phys. Rev. Lett.*, 85(2):266–269, 2000.
- [43] C. Nociforo, K. Jones, L. Khiem, P. Adrich, T. Aumann, B. Carlson, D. Cortina-Gil, U. D. Pramanik, T. Elze, H. Emling, H. Geissel, M. Hellstrm, J. Kratz, R. Kulesa, T. Lange, Y. Leifels, H. Lenske, E. Lubkiewicz, G. Mnzenberg, R. Palit, H. Scheit, H. Simon, K. Smmerer, S. Typel, E. Wajda, W. Walus, and H. Weick. Coulomb breakup of ^{23}O . *Physics Letters B*, 605(1-2):79 – 86, 2005.
- [44] T. Otsuka, R. Fujimoto, Y. Utsuno, B. A. Brown, M. Honma, and T. Mizusaki. Magic numbers in exotic nuclei and spin-isospin properties of the NN interaction. *Phys. Rev. Lett.*, 87(8):082502, 2001.
- [45] T. Otsuka, T. Suzuki, R. Fujimoto, H. Grawe, and Y. Akaishi. Evolution of nuclear shells due to the tensor force. *Phys. Rev. Lett.*, 95(23):232502, 2005.

- [46] A. Ozawa, T. Kobayashi, T. Suzuki, K. Yoshida, and I. Tanihata. New magic number, $N = 16$, near the neutron drip line. *Phys. Rev. Lett.*, 84(24):5493–5495, 2000.
- [47] B. V. Pritychenko, T. Glasmacher, P. D. Cottle, M. Fauerbach, R. W. Ibbotson, K. W. Kemper, V. Maddalena, A. Navin, R. Ronningen, A. Sakharuk, H. Scheit, and V. G. Zelevinsky. Role of intruder configurations in $^{26,28}\text{Ne}$ and $^{30,32}\text{Mg}$. *Physics Letters B*, 461(4):322 – 328, 1999.
- [48] B. S. Pudliner, A. Smerzi, J. Carlson, V. R. Pandharipande, S. C. Pieper, and D. G. Ravenhall. Neutron drops and skyrme energy-density functionals. *Phys. Rev. Lett.*, 76(14):2416–2419, 1996.
- [49] W. D. M. Rae. Nushell for windows, solaris and Linux. unpublished, 2007.
- [50] R. Rebmeister, et al. Report CRN/PN 1983–16, 1983.
- [51] A. T. Reed, O. Tarasov, R. D. Page, D. Guillemaud-Mueller, Y. E. Penionzhkevich, R. G. Allatt, J. C. Angélique, R. Anne, C. Borcea, V. Burjan, W. N. Catford, Z. Dlouhý, C. Donzaud, S. Grévy, M. Lewitowicz, S. M. Lukyanov, F. M. Marqués, G. Martinez, A. C. Mueller, P. J. Nolan, J. Novák, N. A. Orr, F. Pougheon, P. H. Regan, M. G. Saint-Laurent, T. Siiskonen, and E. Sokol. Radioactivity of neutron-rich oxygen, fluorine, and neon isotopes. *Phys. Rev. C*, 60(2):024311, 1999.
- [52] B. Ross and O. Stzowski. Multidimensional calibration of the EXOGAM segmented clover. *Nuclear Instruments and Methods in Physics Research Section A*:

Accelerators, Spectrometers, Detectors and Associated Equipment, 565(2):623 – 629, 2006.

- [53] H. Sagawa and K. Yazaki. Momentum distributions of loosely-bound neutrons with the peripheral direct reaction model. *Physics Letters B*, 244(2):149 – 154, 1990.
- [54] H. Sakurai, S. M. Lukyanov, M. Notani, N. Aoi, D. Beaumel, N. Fukuda, M. Hirai, E. Ideguchi, N. Imai, M. Ishihara, H. Iwasaki, T. Kubo, K. Kusaka, H. Kumagai, T. Nakamura, H. Ogawa, Y. E. Penionzhkevich, T. Teranishi, Y. X. Watanabe, K. Yoneda, and A. Yoshida. Evidence for particle stability of ^{31}F and particle instability of ^{25}N and ^{28}O . *Physics Letters B*, 448(3-4):180 – 184, 1999.
- [55] E. Sauvan, F. Carstoiu, N. A. Orr, J. C. Anglique, W. N. Catford, N. M. Clarke, M. M. Cormick, N. Curtis, M. Freer, S. Grvy, C. LeBrun, M. Lewitowicz, E. Ligard, F. M. Marqus, P. Roussel-Chomaz, M. G. SaintLaurent, M. Shawcross, and J. S. Winfield. One-neutron removal reactions on neutron-rich psd-shell nuclei. *Physics Letters B*, 491(1-2):1 – 7, 2000.
- [56] E. Sauvan, F. Carstoiu, N. A. Orr, J. S. Winfield, M. Freer, J. C. Angélique, W. N. Catford, N. M. Clarke, N. Curtis, S. Grévy, C. Le Brun, M. Lewitowicz, E. Liégard, F. M. Marqués, M. Mac Cormick, P. Roussel-Chomaz, M.-G. Saint Laurent, and M. Shawcross. One-neutron removal reactions on light neutron-rich nuclei. *Phys. Rev. C*, 69(4):044603, 2004.

- [57] W. Schwab, H. Geissel, H. Lenske, K. H. Behr, A. Brnle, K. Burkard, H. Irnich, T. Kobayashi, G. Kraus, A. Magel, G. Mnzenberg, F. Nickel, K. Riisager, C. Scheidenberger, B. M. Sherrill, T. Suzuki, and B. Voss. Observation of a proton halo in ^8B . *Zeitschrift fr Physik A Hadrons and Nuclei*, 350(4):283–284, 1995.
- [58] R. Serber. The production of high energy neutrons by stripping. *Phys. Rev.*, 72(11):1008–1016, 1947.
- [59] A. Signoracci and B. A. Brown. Proton single-particle energies in ^{23}F . *Physical Review C (Nuclear Physics)*, 75(2):024303, 2007.
- [60] J. Simpson, F. Azaiez, G. de France, J. Fouan, J. Gerl, R. Julin, W. Korten, P. Nolan, B. Nyak, G. Sletten, and P. Walker. The EXOGAM array: A radioactive beam gamma-ray spectrometer. *Acta Physica Hungarica New Series - Heavy Ion Physics*, 11(7):159–188, 2000.
- [61] M. H. Smedberg, T. Baumann, T. Aumann, L. Axelsson, U. Bergmann, M. J. G. Borge, D. Cortina-Gil, L. M. Fraile, H. Geissel, L. Grigorenko, M. Hellstrm, M. Ivanov, N. Iwasa, R. Janik, B. Jonson, H. Lenske, K. Markenroth, G. Mnzenberg, T. Nilsson, A. Richter, K. Riisager, C. Scheidenberger, G. Schrieder, W. Schwab, H. Simon, B. Sitar, P. Strmen, K. Smmerer, M. Winkler, and M. V. Zhukov. New results on the halo structure of ^8B . *Physics Letters B*, 452(1-2):1 – 7, 1999.

- [62] O. Sorlin and M.-G. Porquet. Nuclear magic numbers: New features far from stability. *Progress in Particle and Nuclear Physics*, 61(2):602 – 673, 2008.
- [63] J. A. Spiers and R. J. Blin-Stoyle. A formulation of beta-decay theory for forbidden transitions of arbitrary order i: Selection rules and energy spectra. *Proceedings of the Physical Society. Section A*, 65(10):801–808, 1952.
- [64] M. Stanoiu, F. Azaiez, Z. Dombrádi, O. Sorlin, B. A. Brown, M. Belleguic, D. Sohler, M. G. Saint Laurent, M. J. Lopez-Jimenez, Y. E. Penionzhkevich, G. Sletten, N. L. Achouri, J. C. Angélique, F. Becker, C. Borcea, C. Bourgeois, A. Bracco, J. M. Daugas, Z. Dlouhý, C. Donzaud, J. Duprat, Z. Fülöp, D. Guillemaud-Mueller, S. Grévy, F. Ibrahim, A. Kerek, and A. Krasznahorkay. $N = 14$ and 16 shell gaps in neutron-rich oxygen isotopes. *Phys. Rev. C*, 69(3):034312, 2004.
- [65] I. Tanihata, H. Hamagaki, O. Hashimoto, Y. Shida, N. Yoshikawa, K. Sugimoto, O. Yamakawa, T. Kobayashi, and N. Takahashi. Measurements of interaction cross sections and nuclear radii in the light p -shell region. *Phys. Rev. Lett.*, 55(24):2676–2679, 1985.
- [66] I. Tanihata, D. Hirata, T. Kobayashi, S. Shimoura, K. Sugimoto, and H. Toki. Revelation of thick neutron skins in nuclei. *Physics Letters B*, 289(3-4):261 – 266, 1992.
- [67] O. Tarasov, R. Allatt, J. C. Anglique, R. Anne, C. Borcea, Z. Dlouhy, C. Donzaud, S. Grvy, D. Guillemaud-Mueller, M. Lewitowicz, S. Lukyanov, A. C. Mueller,

- F. Nowacki, Y. Oganessian, N. A. Orr, A. N. Ostrowski, R. D. Page, Y. Penionzhkevich, F. Pougheon, A. Reed, M. G. Saint-Laurent, W. Schwab, E. Sokol, O. Sorlin, W. Trinder, and J. S. Winfield. Search for ^{28}O and study of neutron-rich nuclei near the $N = 20$ shell closure. *Physics Letters B*, 409(1-4):64 – 70, 1997.
- [68] J. R. Terry, D. Bazin, B. A. Brown, C. M. Campbell, J. A. Church, J. M. Cook, A. D. Davies, D.-C. Dinca, J. Enders, A. Gade, T. Glasmacher, P. G. Hansen, J. L. Lecouey, T. Otsuka, B. Pritychenko, B. M. Sherrill, J. A. Tostevin, Y. Utsuno, K. Yoneda, and H. Zwahlen. Direct evidence for the onset of intruder configurations in neutron-rich Ne isotopes. *Physics Letters B*, 640(3):86 – 90, 2006.
- [69] J. R. Terry, D. Bazin, B. A. Brown, J. Enders, T. Glasmacher, P. G. Hansen, B. M. Sherrill, and J. A. Tostevin. Absolute spectroscopic factors from neutron knockout on the halo nucleus ^{15}C . *Phys. Rev. C*, 69(5):054306, 2004.
- [70] C. Thibault, R. Klapisch, C. Rigaud, A. M. Poskanzer, R. Prieels, L. Lessard, and W. Reisdorf. Direct measurement of the masses of ^{11}Li and $^{26-32}\text{Na}$ with an on-line mass spectrometer. *Phys. Rev. C*, 12(2):644–657, 1975.
- [71] J. A. Tostevin. Core excitation in halo nucleus break-up. *Journal of Physics G: Nuclear and Particle Physics*, 25(4):735–739, 1999.
- [72] J. A. Tostevin, S. Rugmai, and R. C. Johnson. Coulomb dissociation of light nuclei. *Phys. Rev. C*, 57(6):3225–3236, 1998.
- [73] J. A. Tostevin, University of Surrey. Private communication.

- [74] J. A. Tostevin, University of Surrey. Unpublished.
- [75] Y. Utsuno, T. Otsuka, T. Mizusaki, and M. Honma. Varying shell gap and deformation in $N \sim 20$ unstable nuclei studied by the monte carlo shell model. *Phys. Rev. C*, 60(5):054315, 1999.
- [76] E. K. Warburton, J. A. Becker, and B. A. Brown. Mass systematics for $A = 29-44$ nuclei: The deformed $A \sim 32$ region. *Phys. Rev. C*, 41(3):1147-1166, 1990.
- [77] E. K. Warburton and B. A. Brown. Effective interactions for the 0p1sd nuclear shell-model space. *Phys. Rev. C*, 46(3):923-944, 1992.
- [78] A. Watt, R. P. Singhal, M. H. Storm, and R. R. Whitehead. A shell-model investigation of the binding energies of some exotic isotopes of sodium and magnesium. *Journal of Physics G: Nuclear Physics*, 7(7):L145-L148, 1981.
- [79] V. F. Weisskopf. Radiative transition probabilities in nuclei. *Phys. Rev.*, 83(5):1073, 1951.
- [80] R. D. Woods and D. S. Saxon. Diffuse surface optical model for nucleon-nuclei scattering. *Phys. Rev.*, 95(2):577-578, 1954.